

**CHARACTERIZING CBID AND BAX BINDING TO SUPPORTED LIPID  
BILAYERS**

CHARACTERIZING CBID AND BAX BINDING TO SUPPORTED LIPID  
BILAYERS WITH SINGLE MOLECULE RESOLUTION

By SANJEEVAN SHIVAKUMAR, B.Sc.

A Thesis Submitted to the School of Graduate Studies in Partial Fulfilment of the  
Requirements for the Degree Master of Science

McMaster University © Copyright by Sanjeevan Shivakumar, September 2012

MASTER OF SCIENCE (2012)

Department of Biochemistry and Biomedical Sciences, McMaster University, Hamilton,  
Ontario

TITLE: Characterizing cBid and Bax binding to supported lipid bilayers with single  
molecule resolution

AUTHOR: Sanjeevan Shivakumar, B.Sc. (McMaster University)

SUPERVISOR: Professor Cécile Fradin

NUMBER OF PAGES: xiv, 148

## **Abstract**

Bid and Bax are proteins that play a key role in mitochondrial outer membrane permeabilization during apoptosis. Elucidating the molecular mechanisms regulating the function of these proteins is essential to understanding how apoptosis is altered in diseases and for developing therapies. In this thesis, a mitochondria-like supported lipid bilayer (SLB) system is established and used to characterize the membrane binding behaviour of cBid and Bax with single molecule resolution. The formation of SLBs on mica substrate was characterized and lipid diffusion in the plane of the membrane was measured by fluorescence correlation spectroscopy to be 2-6  $\mu\text{m}^2/\text{s}$  depending on the fluorescent probe used. The binding of cBid to lipids in supported bilayers occurred with an apparent  $K_D$  of 121  $\mu\text{M}$ . Combining fluorescence intensity distribution analysis and confocal imaging, cBid binding to SLBs revealed 2 populations of molecules in the membrane: monomers which primarily diffuse in the plane of the membrane and higher order oligomers which are predominantly immobile. In the presence of Bax, the distribution of cBid molecules shifted towards more mobile protein and smaller complexes, while in the presence of Bcl-XL an opposite shift towards immobile protein and larger complexes occurred. This suggests a mechanism for cBid function where the mobility of cBid in the membrane and its oligomeric state can alter its propensity to activate Bax and influence the progression of apoptosis. Bax binding to SLBs was also observed as two populations of mobile and immobile protein. Both populations comprised mostly Bax monomers. Immobile Bax oligomers up to decamers were also observed, and the formation of higher Bax oligomers appeared to be a cooperative processes once a

dimer was formed. In comparison to Bax binding to liposomal membranes, its affinity for SLBs appeared to be 40-fold less with a measured  $K_D$  of 381  $\mu\text{M}$ .

## **Acknowledgements**

To everyone who made this research project possible, especially my supervisors Dr. Cecile Fradin and Dr. David Andrews, I would like to express my gratitude for their commitment to helping achieve this degree. Thanks to my colleagues in the Fradin and Andrews labs for their collaboration and making it a pleasure to work with them. Thanks to my family for their love and support.

## Table of Contents

1	Introduction.....	1
1.1	Apoptosis, a form of programmed cell death.....	1
1.2	Bcl-2 family proteins, the sentinels regulating apoptosis.....	4
1.3	BH3 interacting-domain death agonist, Bid.....	10
1.4	Bcl-2 associated X protein, Bax.....	13
1.5	Planar membrane model systems.....	19
1.6	Fluorescence fluctuation techniques to characterize planar membrane systems.....	22
2	Materials and Methods.....	26
2.1	General methods.....	26
2.1.1	Materials.....	26
2.1.2	Luria Broth preparation.....	27
2.1.3	SDS-PAGE.....	28
2.1.4	Western Blotting.....	28
2.1.5	Quantifying Protein and Dye by Absorption.....	29
2.2	Preparing lipid films and liposomes.....	30
2.3	Protein Purification.....	31
2.3.1	Purification of Bax.....	31
2.3.2	Purification of Bid.....	33
2.4	Protein labelling.....	35
2.5	ANTS release pore formation assay.....	36
2.6	Bax oligomerization measured by FRET.....	37
2.7	Characterizing Bax binding to liposomes by quantitative Western blot.....	38
2.8	Fluorescence fluctuation experiments.....	40
2.8.1	Measurements.....	40
2.8.2	FCS Analysis.....	42
2.8.3	FIDA.....	43
2.8.4	Dye photostability in fluorescent protein constructs.....	43
2.8.5	FCS analysis of eGFP-Bax binding to liposomes.....	44

2.8.6 FIDA of eGFP-Bax binding to liposomes .....	45
2.9 A Simplified model for Bax binding to liposome membranes.....	46
2.10 Supported Lipid Bilayers .....	47
2.10.1 Mica substrate preparation.....	47
2.10.2. Planar membrane formation .....	48
2.11 Conditions for resolving single molecules on planar membrane .....	49
2.11.1 Resolution of the microscope .....	49
2.11.2 Conditions for single molecule detection .....	50
2.12. Confocal Image Acquisition.....	51
2.13. Automated Image Analysis .....	52
2.14 Object intensity distribution (complex size distribution) analysis .....	55
2.14.1 Expected probability distribution of mobile streaks at the membrane for a single and multiple fluorescent species .....	56
2.14.2 Expected probability distribution of immobile spots at the membrane .....	58
2.15 Determining concentration of protein from images .....	59
2.16 Binding constants for protein binding to planar bilayers .....	60
3 Characterization of Bax binding to liposomes.....	62
3.1 Protein labelling and pore forming activity.....	62
3.2 Bax binding to liposomes by Western blot .....	65
3.3 Bax binding to liposomes by fluorescence techniques.....	67
3.4 Bax binding can be described by a simple binding equilibrium .....	69
3.5 Bax binding to different size liposomes .....	71
4 Characterization of cBid and Bax binding to supported bilayers .....	75
4.1 Optimization of coverslip preparation.....	75
4.2 Characterization of supported lipid bilayer .....	77
4.3 Assessing dye photostability .....	81
4.4 cBid and Bax bind supported bilayers with specificity .....	84
4.5 Confocal imaging of protein binding to SLBs with single molecule resolution .....	86
4.6 Automated image analysis for detection and sorting of fluorescent proteins .....	88



4.7	Quantification of cBid binding to supported bilayers .....	95
4.8	Quantification Bax binding to supported bilayers.....	99
5	Discussion and Conclusions .....	102
5.1	Protein labelling and photostability.....	102
5.2	Fluorescent protein membrane binding and pore forming activity .....	104
5.3	Bax binding to liposomes measured by complimentary techniques .....	106
5.4	Validating the mitochondria-like supported lipid bilayer system .....	108
5.5	Characterization of cBid binding to supported bilayers .....	110
5.6	Characterization of Bax binding to SLBs .....	114
5.7	Future Directions.....	117
6	References.....	120
7	Appendix – ImageJ script for automated image analysis .....	129

## List of Figures

Figure 1: Comparison of 3 models for Bcl-2 family interactions.....	7
Figure 2: Bax vs. Western blot signal displays a linear relationship.....	39
Figure 3: Constant relating mica mass to thickness.....	48
Figure 4: Outline of automated image analysis:.....	53
Figure 5: Pore forming activity of fluorescent proteins.....	62
Figure 6: Bax binding assessed by Western Blot.....	66
Figure 7: eGFP-Bax binding to liposomes by fluorescence techniques.....	68
Figure 8: Bax binding to liposomes quantified by FIDA.....	70
Figure 9: FIDA of Bax binding to different sized liposomes.....	72
Figure 10: Bax membrane permeabilization activity.....	74
Figure 11: Autocorrelation and PCH data for different sample preparations.....	76
Figure 12: Planar membrane formation on mica substrate.....	78
Figure 13: Normalized autocorrelation data for diffusion in the plane of the membrane.....	79
Figure 14: Photostability of HiLyte488 and Atto647 compared to similar Alexa fluors.....	82
Figure 15: cBid specifically binds mitochondria-like SLBs.....	84
Figure 16: Bax specifically binds planar bilayers when cBid is present.....	86
Figure 17: Confocal images of cBid at the plane of the membrane and in solution.....	87
Figure 18: Objects detected by automated image analysis.....	89
Figure 19: Sorting of mobile protein streaks.....	92
Figure 20: Sorting of mobile protein spots.....	94
Figure 21: Characterizing cBid binding to supported bilayers.....	96
Figure 22: Characterizing Bax binding to supported bilayers.....	100

## List of Tables

Table 1: Absorbance properties of dyes.....	29
Table 2: Lipids and tracers used to prepare mitochondria-like liposomes and SLBs.....	30
Table 3: Summary of Bax constructs.....	33
Table 4: Parameter range for Gaussian fitting. ....	54
Table 5. Summary of protein labelling conditions.....	63
Table 6: Optimizing coverslip preparation and thickness.....	75
Table 7: Diffusion coefficients for lipids and tracers in planar membranes.....	79
Table 8: Membrane bound cBid quantified from confocal images .....	98

## List of abbreviations

AFM: Atomic force microscopy

ANTS: 8-aminonaphthalene-1,3,6-trisulfonic acid

BH: Bcl-2 homology

BSA: Bovine serum albumin

CHAPS: 3-[(3-Cholamidopropyl)dimethylammonio]-1-propanesulfonate

CPP: Count rate per particle

DAC: dimethylamino-4-methylcoumarin-3-yl

DiD: 1,1'-dioctadecyl-3,3,3',3'-tetramethylindodicarbocyanine, 4-chlorobenzenesulfonate

DiO: 3,3'-dioctadecyloxacarbocyanine perchlorate

DOPS: 1,2-dioleoyl-*sn*-glycero-3-phospho-L-serine

DMSO: dimethyl sulfoxide

DPX: p-xylene-bis-pyridinium bromide

DTT: dithiothreitol

EDTA: ethylenediamine tetraacetic acid

eGFP: enhanced green fluorescent protein

ER: endoplasmic reticulum

EPR: electron paramagnetic resonance

FCS: fluorescence correlation spectroscopy

FIDA: fluorescence intensity distribution analysis

FRET: fluorescence resonance energy transfer

GUV: giant unlamellar vesicle

HEPES: 2-[4-(2-hydroxyethyl)piperazin-1-yl]ethanesulfonic acid

HRP: Horseradish peroxidase

IAP: inhibitor of apoptosis protein

IMS: intermembrane space

LB: Luria broth

Liss-Rho: Lissamine Rhodamine B

MOM: mitochondrial outer membrane

MOMP: mitochondrial outer membrane permeabilization

MW: molecular weight

NA: numerical aperture

NBD: N-(7-nitrobenz-2-oxa-1,3-diazol-4-yl)

PC: L- $\alpha$ -Phosphatidylcholine

PCH: Photon counting histogram

PE: L- $\alpha$ -phosphatidylethanolamine

PI: L- $\alpha$ -phosphatidylinositol

PMSF: phenylmethanesulfonyl fluoride

ROI: region of interest

SANS: small angle neutron scattering

SDS-PAGE: sodium dodecyl sulphate polyacrylamide gel electrophoresis

SLB : supported lipid bilayer

SUV: small unilamellar vesicle

TBS-T: Tris Buffered Saline with Tween

TCEP: 3,3',3''-Phosphanetriyltriopropanoic acid

TIRF: total internal reflection microscopy

TNF: tumour necrosis factor

TOCL: 1,1',2,2'-tetraoleoyl cardiolipin

Tris: 2-Amino-2-hydroxymethyl-propane-1,3-diol

WT: wild-type

## **Declaration of Academic Achievement**

All data and findings presented in this thesis were the result of original experiments performed by the author. Certain proteins were purified and labelled by collaborators as follows. Alexa647-cBid and WT Bcl-XL was obtained from Aisha Shamas-Din. NBD-Bax134C was obtained from Mina Falcone. Equations in section 2.14 were derived by Dr. Cécile Fradin.

## **1 Introduction**

Apoptosis is a fundamental process regarding cell fate – the question of life or death at the cellular level. Bcl-2 family proteins are the regulators of apoptosis and can function to promote or inhibit cell death in both healthy and diseased states. Great efforts have been made to understand the protein-protein and protein-membrane interactions involved in apoptosis and the molecular mechanisms by which apoptosis is regulated. Still, specific questions regarding the state of Bcl-2 proteins, their interactions and conformational changes at the single molecule level have yet to be answered. In this thesis a novel interdisciplinary approach is presented to investigate Bcl-2 protein interactions in a mitochondria-like planar membrane model system allowing the detection and characterization of single molecules or molecular complexes.

### *1.1 Apoptosis, a form of programmed cell death*

Multicellular organisms must achieve a balance between the cell generating process of mitosis and cell death to maintain homeostasis and allow normal development. Cell death can occur by several processes that have distinct morphological and biochemical features. The earliest described type of cell death was necrosis in which external insults such as viral infection, poisons or trauma resulted in the loss of membrane integrity, cell/organelle swelling and eventual rupture (Edinger & Thompson, 2004). The contents released from necrotic cells detrimentally affect surrounding tissue and illicit an inflammatory response. As such, necrosis was classically thought of as “accidental” cell death due to injury. In contrast, apoptosis is a form of cell death that can be likened to cellular suicide – the cell kills itself in response to physiological death stimuli such as



DNA damage or absence of growth hormone. Apoptosis is characterized by nuclear condensation, preservation of cell membrane integrity and formation of apoptotic bodies whose cellular material is recycled by phagocytosis. This process is not accompanied by an inflammatory response (Kerr et al, 1972). As such, apoptosis is mainly beneficial to the organism by maintaining a regular turnover of cells, as well as killing vestigial cells during development (Kerr et al, 1972; Cotter, 2009). Considering ~60 billion cells are produced by mitosis each day in the average adult, apoptosis is a vital process that if deregulated can have disastrous effects. In situations when there is excessive apoptosis, prematurely dying cells lead to loss of tissue function. An example is cell death by apoptosis following a stroke or heart attack which can reduce brain/heart activity and prolong recovery time. The loss of neurons seen in Alzheimer's and Parkinson's disease is also the result of apoptosis. The inhibition or lack of apoptosis can be just as damaging. A hallmark of many cancers is resistance to apoptosis which allows unchecked cell proliferation (Cotter, 2009).

Apoptotic cell death can be separated into initiation and execution phases. During the initiation phase, the cell analyzes stimuli originating outside or within the cell to determine whether it should elicit an apoptotic response. If the cell is fated to die, the execution phase is marked by the activation of cellular caspases-2, -8 and -9 known as initiator caspases. The initiator caspases cleave and activate the executioner caspases-3, -6 and -7 which in turn cleave their respective target proteins in the cell causing cell dismantlement. The decision as to the cell's fate during the initiation phase can occur via two pathways: Type I (extrinsic) and Type II (intrinsic). In type I cells, ligand binding to

the TNF family of death receptors on the cell surface (ex. Fas, TNF receptors) leads to the activation of caspase-8 via downstream interaction with adaptor proteins. The extrinsic pathway is mainly used to get rid of unwanted cells during development and immune response (Boatright & Salvesen, 2003). The intrinsic (Type II) pathway involves mitochondrial outer membrane permeabilization (MOMP) leading to caspase-9 activation. The intrinsic pathway initiates apoptosis in response to cell damage resulting from radiation, organelle damage and chemotherapeutic drugs (Boatright & Salvesen, 2003).

Both extrinsic and intrinsic pathways converge at the mitochondria (although it is not necessary for the extrinsic (Type I) pathway to proceed this way). Several factors central to the Type II pathway normally reside in the intermembrane space (IMS) of mitochondria. When released into the cytoplasm by MOMP, these factors lead to caspase-9 activation. Cytochrome C is an IMS resident protein that has been well characterized for its role in oxidative phosphorylation (Voet & Voet, 2004). When released from mitochondria during MOMP, cytochrome C forms a complex with Apaf-1 and dATP known as the apoptosome which recruits procaspase-9 and initiates its self- cleavage into caspase-9 (Zou et al, 1999). Active caspase-9 goes on to cleave its target executioner caspases leading to cell death. Other IMS proteins are also released to alleviate the effects of inhibitors of apoptosis proteins (IAPs). IAPs bind to caspases and inhibit their function. A well studied IAP is XIAP which binds to caspase-3, -7 and -9. XIAP itself is inhibited by SMAC/DIABLO, another intermembrane space protein released during MOMP, thereby promoting caspase activity (Sun et al, 2002). In addition, factors are also

released that contribute to apoptosis in a caspase-independent manner. AIF is a protein that translocates to the nucleus and causes chromatin condensation upon release from mitochondria and can overcome caspase inhibition to induce apoptosis (Susin et al, 1999).

MOMP separates the initiation and execution phases of apoptosis and is the key step that irreversibly commits the cell to death. As such, it is the tipping point in the pathway where apoptosis can be modulated to change the outcome of disease states. MOMP is tightly controlled by the Bcl-2 family of proteins. There is also evidence for an ER-specific death pathway mediated by Bcl-2 proteins, but the mitochondrial pathway has been described in greater detail and will be discussed here.

### *1.2 Bcl-2 family proteins, the sentinels regulating apoptosis*

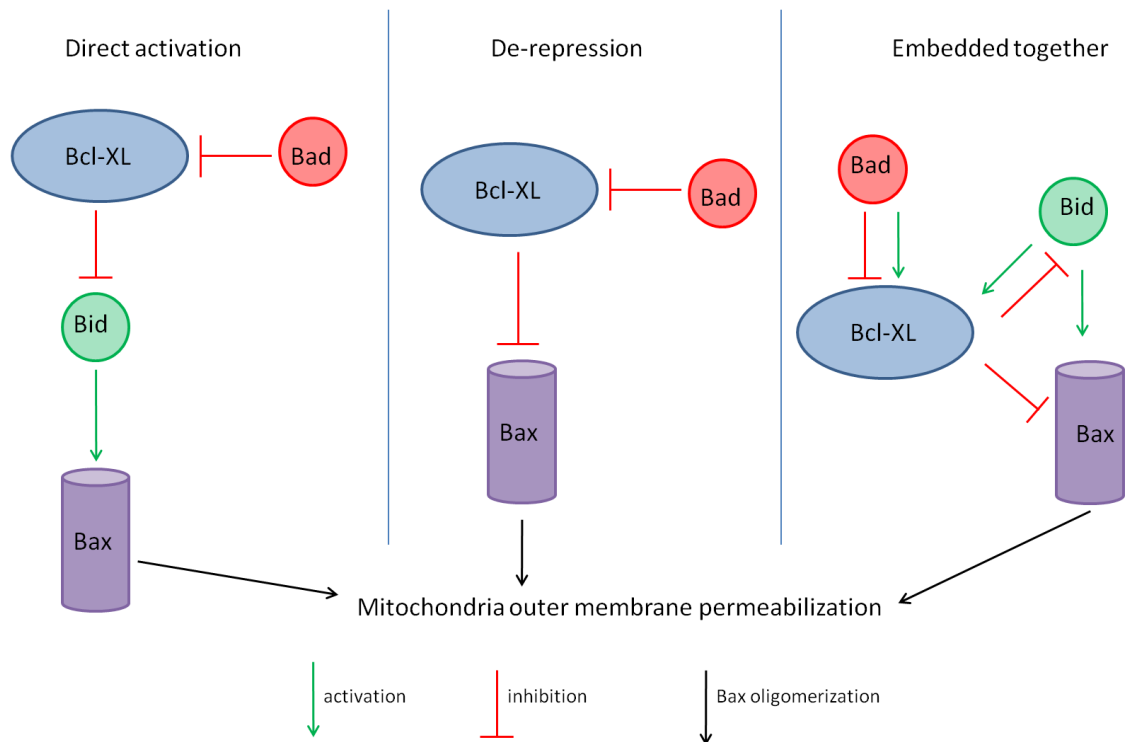
MOMP (and initiation of apoptosis) is tightly regulated by the Bcl-2 protein family. The namesake of the family, Bcl-2, was first identified as a potential oncogene in B cell lymphoma and when overexpressed was found to render cells resistant to a number of death stimuli (Tate and Green, 2010). Since Bcl-2 was first identified, some 20 members of the family have been described (Youle and Strasser, 2008). All Bcl-2 proteins share at least one of four conserved Bcl-2 homology (BH) regions (Antonsson and Martinou, 2000) and can be functionally grouped into 3 classes (Figure 1). Anti-apoptotic members (e.g. Bcl-2, Bcl-XL) possess all 4 BH regions and function to inhibit the onset of apoptosis. Pro-apoptotic Bcl-2 proteins are organized into 2 classes (Tate and Green, 2010; Chipuk et al, 2010; Youle and Strasser, 2008): the multi-domain pro-apoptotic proteins contain BH regions 1, 2 and 3 (Bax, Bak) and are capable of membrane permeabilization; the second class of pro-apoptotic proteins contain only the BH3 region

and can be further subdivided into 2 groups (Tate & Green, 2010; Chipuk et al, 2010; Youle & Strasser, 2008; Leber et al, 2007). Some BH3-only proteins (e.g. Bid, Bim) can directly bind and activate the multi-domain pro-apoptotic proteins and function as activators. The other subset of BH3-only proteins (e.g. Bad, Noxa) bind and inhibit the anti-apoptotic Bcl-2 proteins and are known as sensitizers (of apoptosis). Collectively, the function of the BH3-only inducers and sensitizers is pro-apoptotic. In the cell, the protein-protein interactions between the pro- and anti-apoptotic Bcl-2 family proteins determine its fate.

A striking feature about the Bcl-2 family is that despite the opposing functions of the multi-domain pro- and anti-apoptotic proteins, the solution structures of Bcl-XL and Bax (multi-domain Bcl-2 proteins) and Bid (a BH3-only protein) share a remarkably similar alpha helical secondary structure and fold (Petros et al, 2004). They contain a conserved core where the BH1, BH2 and BH3 regions of the protein define a hydrophobic pocket. When the proteins are in their inactive cytosolic form, this pocket is occupied by the C-terminal tail anchor helix (Chipuk et al, 2010). The BH3 region of activators and sensitizers also occupies this hydrophobic pocket when BH3-only proteins bind multi-domain proteins. Recently, the classical boundaries between the 3 groups of Bcl-2 proteins based on BH regions have been blurred by the identification of a novel BH4 consensus sequence in pro-apoptotic proteins such as Bid and Bax (Kvansakul et al, 2008). The putative BH4 domain is hypothesized to be a common structural element across the Bcl-2 family, although in Bcl-XL and Bcl-2 the BH4 domain confers anti-apoptotic function. It has been hypothesized that similarity in structure facilitates the

interaction between Bcl-2 family members by domain swapping. Indeed, there is evidence that Bcl-Xl homodimers (O'Neal et al, 2006), Bcl-Xl/Bax heterodimers (Suzuki et al, 2000) and Bcl-2/Bax heterodimers (Zha et al, 1996) are formed by BH3-BH3 interactions between monomers.

Initially, two models were proposed to explain the interactions between Bcl-2 proteins in regulating apoptosis (Figure 1) (reviewed by Leber et al, 2007). The direct activation model stipulates that the multi-domain pro-apoptotic proteins (Bax, Bak) are inactive unless directly activated by an activator (Bid, Bim) (reviewed by Leber et al, 2010). The activators themselves are normally in an inactive state or not expressed in the absence of apoptotic stimuli. Evidence for this model was derived primary from in vitro liposome systems or isolated mitochondria using recombinant proteins and peptides. When isolated mitochondria were incubated with tBid (a truncated activated form of Bid) in the presence of Bak (Wei et al, 2000) or tBid in combination with Bax (Eskes et al, 2002) cytochrome C was released indicating membrane permeabilization by the concerted effort of Bid activating Bak/Bax. In liposomes, recombinant cBid with Bax is sufficient to cause the release of encapsulated dextrans of sizes up to 2000kDa indicating the formation of large openings in liposomal membranes (Kuwana et al, 2002). BH3 peptides from activators appear to have the same pro-apoptotic effect as the full length proteins. Bak mediated cytochrome C release from isolated mitochondria is seen when Bak is activated by BH3 peptides from Bid and Bim, but not with BH3 peptides from sensitizers (Bad, Bik, Noxa) (Letai et al, 2002).



**Figure 1: Comparison of 3 models for Bcl-2 family interactions.** Here Bcl-XL, Bax, Bid and Bad are representative of anti-apoptotic, pro-apoptotic, BH3-only activator and BH3-only sensitizer proteins, respectively. The key difference between direct activation and de-repression is the activity of Bax. In direct activation, pro-apoptotic Bax is inactive until activated by Bid; BH3-only proteins are classified as either activators or sensitizers of apoptosis. The De-repression model states Bax is constitutively active and must be inhibited by Bcl-XL; BH3-only proteins are classified in terms of binding affinity for the anti-apoptotic proteins (no distinction between activators/sensitizers). Embedded together recognizes the role of BH3-only activators and sensitizers (as in direct activation) in addition to stipulating that BH3-only proteins can activate anti-apoptotic proteins by recruiting a molar excess of anti-apoptotic protein to bind the membrane. Once inserted, anti-apoptotic proteins are active and can bind pro-apoptotic proteins (as in de-repression). The role of the membrane is key, since it is required for the conformational changes required for activating many Bcl-2 proteins and many interactions occur while membrane-bound. Figure adapted from Leber et al, 2010.

In contrast, the de-repression model states that Bax/Bak are constitutively active and must be inhibited by anti-apoptotic proteins (reviewed by Leber et al, 2007). When apoptosis is triggered, BH3-only proteins inhibit the anti-apoptotic proteins. Evidence for de-repression was gleaned from data showing that certain BH3-only proteins were able to bind anti-apoptotic proteins specifically, and with high affinity, inhibiting their function (Chen et al, 2005). Furthermore, “addicted” cancer cells that are primed for death contain

membrane bound (activated) pro-apoptotic proteins which are constitutively inhibited by overexpressed anti-apoptotic proteins. In a series of experiments, once these proteins were knocked down or inhibited by BH3-only sensitizers, cancer cells underwent apoptosis lending further evidence to the de-repression model (Certo et al, 2006; Chipuk et al, 2008). Finally, in certain cases, the de-repression model allows for Bid and Bim to function as non-specific inhibitors of anti-apoptotic proteins. Compared to BH3 sensitizers which target specific anti-apoptotic Bcl-2 members, Bid and Bim BH3 peptides are able to bind multiple anti-apoptotic proteins in mouse embryonic fibroblasts and this binding increased after cellular insult (Willis et al, 2007). In addition, cells with a double knockout lacking Bim and Bid could still be induced to undergo apoptosis suggesting that Bid and Bim are not required to function as direct activators.

A shortcoming of the two models above is assuming that all interactions can occur in solution and therefore fail to incorporate the role of the mitochondrial outer membrane (MOM) in regulating Bcl-2 protein interactions (Leber et al, 2010). However, considering some Bcl-2 proteins are constitutively membrane bound (Bak, Bcl-2), while others need to bind the MOM to carry out their respective functions (Bax, Bcl-Xl) the membrane likely plays a significant role in the functions of the Bcl-2 family (Leber et al, 2007; Youle and Strasser, 2008; Chipuk et al, 2010). Also, the homology in structure, despite divergence in function, suggests a common affinity for the MOM (Leber et al, 2007; Kuwana et al, 2002). There is a large body of evidence that the specific lipid composition of membranes affects the permeabilization ability of Bax. Negatively charged lipids in particular, such as cardiolipin, are required for Bid mediated membrane permeabilization

by Bax (Kuwana et al, 2002; Lucken-Ardjomande et al, 2008). Furthermore, there is evidence that membrane permeabilization by Bax involves lipidic pores in which lipid and protein line the interior of the pore (Kuwana et al, 2002; Epand et al, 2002). To acknowledge to role of the MOM in mediating Bcl-2 family interactions and to reconcile some of the differences between the direct activation and de-repression models, Leber et al. proposed the “embedded together” model (Figure 1) (Leber et al, 2007 & 2010). This model recognizes that many functional Bcl-2 protein interactions require conformational changes adopted by the proteins upon membrane binding. Also, contrary to the other models, “embedded together” states that it is possible for certain BH3-proteins to not only inhibit anti-apoptotic proteins, but also activate them (Bogner et al, 2010). For example, Bid can cause the insertion of a 4-fold molar excess of Bcl-XL into the membrane (Billen et al, 2008). In this situation, Bcl-XL can adopt two different conformers to perform its anti-apoptotic function by either sequestering Bid (as in the direct activation model) or inhibiting Bax (as in the de-repression model). Finally, “embedded together” stresses that a large portion of the data that forms the basis of the 2 older models was obtained using truncations or peptides of Bcl-2 proteins that may already be “activated” without membrane insertion (Leber et al, 2007). Thus, the data obtained from such studies may not confirm physiologically relevant interactions in the absence of a membrane. Future work must try to use full length proteins in the correct context whether it is in solution or in membranes.

Since Bcl-2 proteins are the sentinels that control MOMP, there is great clinical demand for drugs that can modulate this process. Based on the disease state, it may be



necessary to promote or inhibit apoptosis as a treatment. Targets of particular importance are the proteins that play an essential role in the physical permeabilization of mitochondria.

### *1.3 BH3 interacting-domain death agonist, Bid*

Bid is a 22kDa protein comprised of 8 alpha helices first identified through interactive cloning as a protein that associated with Bax and Bcl-2 (Wang et al, 1996). Bid has been classically described as a BH3-only activator (Eskes et al, 2000; Kuwana et al 2002; Terrones et al, 2004), however more recent evidence suggests Bid is more similar to multi-domain Bcl-2 proteins than the BH3-only subgroup in many respects (reviewed in Billen et al, 2009). Unlike other BH3-only proteins which are intrinsically unstructured, Bid has a 3D fold in solution similar to Bax and Bcl-XL (Petros et al, 2004). This is especially evident for the BH3 region of Bid which always maintains a helical structure, as opposed to the BH3 region of some other BH3-only proteins which only adopt a helical structure upon binding to anti-apoptotic Bcl-2 family proteins (Hinds et al, 2007). More recently, Bid was found to contain a putative BH4 region, similar to other multi-domain Bcl-2 proteins (Kvansakul et al, 2008).

Bid function is regulated by a number of post-translational modifications. Of particular importance in apoptosis is cleavage of cytosolic Bid by caspase-8 in response to apoptotic stimuli. The 2 fragments of cleaved Bid, known as cBid, remain associated by hydrophobic interactions until cBid targets to mitochondria (Gross et al, 1999). In the presence of the MOM, the 2-fragments separate spontaneously and the larger p15 fragment known as truncated Bid, tBid, inserts into the MOM (Lovell et al, 2008). The

insertion of tBid into membranes is thought to be very similar to Bax membrane insertion, particularly N-terminal conformational changes and exposure of the BH3 region. It is thought the N-terminal (p7 portion) of Bid negatively regulates its apoptotic function (McDonnell et al, 1999); cleavage and subsequent separation of the p7 fragment allows tBid to bind membranes (Lovell et al, 2008). The space vacated by the p7 fragment allows the BH3 region of Bid to become exposed. Bax BH3 exposure upon membrane binding is also mediated by an N-terminal conformational change (Hsu & Youle, 1997). Bid membrane binding occurs by the insertion of helices 6, 7 and 8 into the MOM. An important difference in insertion into the MOM is that Bid membrane binding helices appear to embed in the membrane more parallel to the plane of the membrane (Oh et al, 2005) while Bax helices are thought to span the entire membrane (Annis et al, 2005).

It is believed that Bid binding to Bcl-XL and Bax is achieved by the BH3 helix of Bid binding the hydrophobic pocket present in the multi-domain Bcl-2 proteins, thereby displacing the tail anchor helix which occupies the pocket in solution; the multi-domain proteins then bind to the MOM. Interestingly, the solution structure of Bid has a region similar in structure to the hydrophobic cleft of multi-domain Bcl-2 proteins, though it is solvent exposed and not occupied by a tail anchor helix (Billen et al, 2009). The presence of this potential binding pocket in Bid suggests the possibility for dimerization with other Bcl-2 proteins as well as Bid-Bid interactions leading to homooligomerization similar to Bax. Indeed, there is evidence for Bid ion channel formation and dimerization in membranes, as detailed below.

The activated form of Bid (tBid) and a caspase-8 cleavage mimic (Bid $\Delta$ 1-55) cause ion release from liposomes and form ion channels in planar membranes, though this was not observed with full-length Bid (Schedel et al, 1999). The channels formed are voltage gated, and the methodology of measuring current fluctuations is macroscopic, suggesting the majority of Bid molecules in the system were involved in channel formation. tBid-tBid interactions that suggest oligomer formation have also been observed in live cells. tBid was found to be part of a 45kDa crosslinked complex present in the MOM following induction of apoptosis in 293T kidney cells. This complex did not contain Bax, Bak or other MOM proteins assayed for by Western Blot and appeared to be a tBid homotrimer (Grinberg et al, 2001). Furthermore, enforced tBid dimerization using a FKBP-tBid chimera resulted in cytochrome C release from mitochondria as well as caspase activation. A FKBP-tBid mutant unable to bind Bak or Bax was also found as homo-trimers and caused cytochrome C release, suggesting membrane permeabilization was not mediated by Bax or Bak. As a final confirmation, tBid-tBid FRET was observed in cells underlining a physical interaction between tBid molecules (Grinberg et al, 2001).

Bid has been classically characterized as a BH3-only activator capable of activating Bax or Bak mediated membrane permeabilization. However, there is evidence Bid can bind and cause membrane insertion of a molar excess of Bcl-XL, which is required for its anti-apoptotic function (Billen et al, 2008; Garcia-Saez et al, 2009). In this context, Bid can be considered an activator for Bcl-XL anti-apoptotic function. As Bid is uniquely capable of activating both pro- and anti-apoptotic proteins, it is an important mediator in tipping apoptosis towards cell death or survival. Thus, understanding the

molecular mechanisms regulating Bid apoptotic activity, and the accompanying conformational changes and molecular interactions is vital. If Bid is capable of oligomerization and pore formation, it is important to discern the size and stoichiometry of Bid complexes using full length proteins at physiological concentrations. It is also of interest to compare the formation of Bid complexes in the presence of Bax and Bcl-XL.

#### *1.4 Bcl-2 associated X protein, Bax*

Bcl-2 associated protein X, Bax, is a 22kDa pro-apoptotic protein first described as a co-precipitate with Bcl-2 in 1993 (Oltvai et al, 1993). Ironically, the initial interaction described was a detergent mediated artifact (Hsu & Youle, 1997), although subsequent studies verified Bcl-2 is able to bind Bax to exert its anti-apoptotic function. Currently, Bax is one of the few known Bcl-2 proteins (the others being Bak and possibly Bok) that can oligomerize to form pores and permeabilize membranes. Structurally, Bax is helical comprising 9 alpha helices. In the absence of apoptotic stimuli, Bax is located in the cytoplasm, in its inactive form, adopting a globular structure with hydrophobic helix 9, a tail anchor, sequestered in a hydrophobic binding pocket in the core of the protein surrounded by amphipathic helices (Suzuki et al, 2000).

Once the solution structure for Bax was solved, it was noted that hydrophobic helices 5 and 6 of Bax resembled the pore forming domain of Diphtheria toxin and bacterial colicins (Petros et al, 2004). Chemical labeling of residues along the length of these helices, and the C-terminal tail anchor helix 9, confirmed that helices 5, 6 and 9 insert upon membrane binding (Annis et al, 2005). The current model for Bax activation implicates an activator (Bid, Bim) that recruits cytosolic Bax to adopt a different

conformation and bind the membrane which occurs in a series of ordered steps (Lovell et al, 2008). Recently, the underlying structural changes accompanying membrane insertion were investigated. Activation of Bax at a “trigger site” by BH3 inducers causes displacement of the loop between helix 1 and 2 (Gavathiotis et al, 2008) accompanied by exposure of the N-terminal 6A7 epitope which is an indicator of activated Bax (Hsu & Youle, 1997). Following this, the helix 9 tail anchor is displaced from the hydrophobic pocket and initiates membrane binding. Displacement of the tail anchor causes the BH3 region of Bax to become exposed. There is much evidence suggesting the BH3 region of Bax is necessary for Bax homo-oligomerization (Walensky et al, 2004; Tan et al, 2006; Gavathiotis et al, 2010). Furthermore, it is thought that the BH3 region is also involved in autoactivation of subsequent Bax molecules to insert into the membrane, based on data collected using a Bax BH3 peptide to activate full-length Bax to permeabilize liposomes (Tan et al, 2006).

The observation that cytochrome C release from mitochondria soon followed Bax mitochondrial localization led to the suspicion that Bax may be involved in causing the release of factors from the intermembrane space (Desagher et al, 1999). This suspicion was confirmed when Bax was observed to oligomerize and form pores large enough for cytochrome C release in liposomes (Saito et al, 2000; Schlesinger & Saito, 2006; Heimlich et al, 2004). Annis et al. also suggested that membrane inserted Bax monomers oligomerize to form a pore in contrast to oligomerization prior to membrane insertion similar to some barrel pore channels. While helices 5, 6, and 9 of Bax insert upon membrane binding, helices 5 and 6 appear to be the pore forming helices required for

membrane permeabilization (Heimlich et al, 2004; Nouraini et al, 2000). Two models have been proposed to describe the formation of Bax pores from membrane inserted monomers. The asymmetric oligomerization model considers that Bax oligomers form similar to a growing polymer chain that can loop back to form a pore (Reed, 2006). Individual Bax monomers are added to the growing chain with only one type of Bax-Bax interface – the front surface of a Bax molecule interacts with the rear surface of its neighbour. In contrast, the symmetric model proposes that there are two distinct Bax-Bax interfaces in an oligomer (front-front and back-back). Evidence for this model was put forward when 2 Bax-Bax interacting regions were identified using site-specific crosslinking (Zhang et al, 2010). One interface is the BH3 region which is exposed when Bax monomers insert into the membrane. The exposed BH3 regions of two Bax monomers interact in dimer formation, consistent with evidence suggesting Bax dimerization occurs by BH3 domain swapping. Bax dimers then interact via a second interface on the opposite side from the BH3 pocket region, and oligomer formation proceeds in increments of two Bax molecules at a time (Zhang et al, 2010). Recently it has been shown that Bim BH3 peptide activation of Bax may be mediated via interaction at a previously uncharacterized site distal to the BH3 region (Gavathiotis et al, 2008). It is hypothesized that activation at a distal site allows the Bax hydrophobic pocket site free to interact with another Bax BH3 helix thereby providing a mechanism for symmetric Bax oligomerization.

Bax plays an essential role at the commitment step of apoptosis, and is an attractive drug target to modulate apoptosis. Drugs that can either inhibit or activate Bax

may be used to treat a variety of diseases depending on how apoptosis is deregulated. In situations of excessive cell death, a Bax inhibiting drug could be administered, for example during the recovery period following stroke or heart attack (Mattson et al, 2000). In cancer, the goal is to kill immortalized cancer cells by administering a Bax activator (or a Bax substitute) to promote MOM permeabilization and cause cancer cells to undergo apoptosis. To this end, Bax derived pore forming peptides have been shown to commit cancer cells to apoptosis and cause tumour regression (Valero et al, 2010). Evidence suggests that, Bax binding and oligomerization is the rate-limiting step in Bax activation leading to MOM permeabilization (Lovell et al, 2008). Since this step is the slowest, it would be the point at which drug intervention would have the greatest effect. However, to develop a potent Bax drug, a concrete understanding of the molecular interactions and structural changes associated with Bax membrane binding and oligomerization must first be known. To date, much work in the field has been put towards elucidating the stepwise molecular interactions during Bax activation from inactive cytoplasmic protein to oligomeric pores. The size (stoichiometry) of Bax pores on the membrane remains an unanswered question. Determining the amount of Bax present on the MOM as well as the size of Bax complexes at the point of no return is vital to determine dosage of potential drugs.

There have been several studies undertaken to determine the number of Bax molecules that make up a functional pore. Saito et al (2000) proposed that a Bax tetramer pore is sufficient to cause cytochrome C release based on vesicle leakage of fluorescently labeled cytochrome C from liposomes. However, studies using a variety of techniques

have since yielded a large variation in both the number of Bax molecules and size of the pore, ranging from Bax dimers to large pores with possibly hundreds of Bax present. Data using current measurements of ion release and of loss of membrane potential due to pore formation suggests that the majority of Bax pores are fairly small (Schlesinger & Saito, 2006). Relating ion release data as a function of pore size, and the number of Bax molecules that can be accommodated in a pore of certain size, yielded Bax dimers/tetramers (Schlesinger & Saito, 2006) to decamers (Martinez-Caballero et al, 2009).

Attempts have also been made to extract native Bax complexes from isolated mitochondria post induction of apoptosis. Gel filtration of extracted MOM fractions showed Bax as part of large complexes up to 260 kDa (Antonsson et al, 2001). However, the authors note that the complexes did contain other Bcl-2 proteins and not solely Bax. Isolating native Bax complexes has proved to be difficult due to the interaction between Bax and other resident MOM proteins. There is evidence that Bax interacts with TOM40 and VDAC among other MOM resident proteins (Ghibelli & Diederich, 2010). Recently Rack1 was found to promote Bax oligomerization, colocalize with Bax pores and mediate interactions with Bax through the BH3 region (Wu et al, 2010). If so, it is the first example of a non Bcl-2 protein interacting with Bax's BH3 region. Thus, high weight Bax complexes isolated from mitochondria may contain Bax in complex with other Bcl-2 or mitochondria resident proteins. Care must also be taken when choosing detergents to solubilize mitochondrial membranes to isolate Bcl-2 family proteins, since many detergents activate these proteins leading to detergent mediated artifacts (Hsu & Youle,



1997). To address this, Valentijn et al. used Blue-Native PAGE of mitochondrial membrane extracts, and found Bax was part of significantly large complexes ~200kDa, although these complexes likely contained other MOM proteins, not solely Bax (Valentijn et al, 2008).

The Bax pore is believed to be lipidic based on its toroidal appearance, and ability to “grow” with lipid head groups and possibly alpha helices lining the pore (Kuwana et al, 2002; Epand et al, 2002). Few studies have attempted to directly observe Bax pore formation. The first such study reported possible Bax pores 100-300nm in size containing up to 22 Bax molecules when imaging Bax oligomers on a planar membrane using atomic force microscopy (AFM) (Epand et al, 2002). However, the Bax in this study was expressed with a C-terminal truncation, activated by detergent and many times the physiological concentration of protein was used. This likely accounts for the unusually large pores observed. A recent study made use of electron paramagnetic resonance (EPR) spin labeling of Bax molecules in a biophysical approach to the question. EPR data was fit to a model that proposes 6 Bax monomers in a 3 homodimer complex forming a pore large enough for cytochrome C release (Bleicken et al, 2010).

The collective data suggests that there may be a variety of Bax pore sizes depending on the experimental techniques and Bax constructs used. Alternatively, the different methodology may be biased towards one Bax complex over another. The use of truncated proteins and peptides in place of full-length constructs or in the presence of detergent may additionally lead to artifacts. A final consideration is the possibility that Bax pores are dynamic in size and may exist as a population of different sized pores at a

given time. However, in such a population a pore size may predominate and comprise most of the oligomerized Bax. If such a preferred pore size exists, it would represent a stable Bax complex that is likely the structure to be inhibited by drugs against Bax. A recent study using a Bax pore forming domain peptide (helix 5-6) unexpectedly found Bax pores that shrink in size over time (Fuertes et al, 2010). Initial pores formed in giant unilamellar vesicles (GUVs) were large, however after two hours the pores that persisted at an equilibrium state were smaller as determined by subsequent dye leak-in. The authors concluded that the initially large pores relaxed to an equilibrium pore size after a few minutes due to stabilization of a lipidic pore. They further hypothesized that the equilibrium pores correspond to a stable complex of the full length protein. To determine if such a preferred pore size exists, a large number of individual pores must be observed to gauge the distribution of pore sizes.

### *1.5 Planar membrane model systems*

Much of the previous work in elucidating the interactions and molecular mechanisms of Bcl-2 family proteins has been done in live cells, isolated mitochondria and liposome model systems. Furthermore, the methods employed in these previous studies were mostly ensemble techniques where the data obtained represent the average for a population of molecules or oligomers. Yet, in complex systems, the average value may not give a complete description, as it says nothing about the distribution of individual molecules in the population. Consequently, specific questions as to the behaviour of individual proteins, their interactions and conformational changes cannot be addressed. Observing individual Bax pores is difficult in live cells and model liposome

systems. A planar membrane model system, such as a supported lipid bilayer (SLB), can be used to provide a membrane in which physiologically relevant interactions of proteins can be investigated. A SLB system offers certain advantages over liposome systems, in particular the opportunity to observe single protein molecules with good spatial and temporal resolution. Compared to immobilized GUVs, a SLB offers a more extended field of view when observing diffusion in a single plane by confocal microscopy or total internal reflection (TIRF) microscopy. This way, the spatial distribution of proteins interacting with the membrane can be visualized with accuracy. Such a system also offers the potential to observe multiple Bax pores at once and track single molecules and pores over time. Thus, SLBs provide a straightforward method to measure translational lipid and protein diffusion in the plane of the membrane (Kießling et al, 2008). A final advantage of SLBs is the opportunity to implement complimentary techniques such as atomic force microscopy (AFM) and neutron or x-ray reflectivity to further characterize membrane topology as well as the structure(s) of bound proteins.

Lipid diffusion in SLBs has been found to be somewhat slower than diffusion in free-standing vesicles (Chiantia et al, 2006; Garcia-Saez & Schwille, 2008). This is likely due to interactions of the solid substrate with lipids retarding translational motion particularly in the lower leaflet (Przybylo et al, 2006). The presence of the substrate may therefore impact protein insertion in SLBs. However, protein binding to planar membranes has been reported on numerous occasions, with proteins retaining their *in vitro* function (reviewed in Kießling et al, 2008). Another possible limitation of planar membranes is their lack of intrinsic curvature, whereas biological membranes are curved.

Curvature allows for dynamic changes in the shape of organelles and facilitates protein binding and insertion into membranes. It has been observed that Bax preferentially permeabilizes membranes containing lipids with an intrinsic positive curvature (Basanez et al, 2002), which is consistent with the idea that lipidic pores create lipid surfaces that too have positive curvature (Terrones et al, 2004). Lipidic pore formation may prove to be more difficult in SLBs, as membrane curvature is not allowed in a non-disturbed planar configuration. However, the presence of lipids with positive intrinsic curvature might mitigate this.

SLBs can be formed by depositing lipids onto a suitable solid substrate surface using various methods (reviewed in Kiessling et al, 2008). The earliest SLBs were formed by the Langmuir-Blodgett technique which involves dipping of a solid substrate into a trough containing a lipid monolayer on top of aqueous solvent. Each time the substrate is dipped and drawn through the air-liquid interface, a monolayer of lipid is deposited on the substrate. Repeating the process can add additional layers of lipid. Vesicle fusion, where small unilamellar vesicles (SUVs) are absorbed onto a surface, has been used previously for the formation of SLBs (Richter & Brisson, 2005; Reviakine & Brisson, 2000; Cremer & Boxer, 1999). Bilayer formation by this method occurs in stages (Richter et al, 2006): First, diffusing vesicles interact with the substrate surface and attach. Interactions between the lipid head groups and the surface cause flattening of the vesicle. The subsequent increase in surface tension at the edges causes vesicle rupture at one or both ends. The two bilayers then slide over one another until they are in the same plane. In addition to electrostatic interactions between lipids and the substrate and reduction in

vesicle surface tension, it has been proposed that a further driving force for SLB formation is the leading edge of a spreading planar bilayer may rupture attached vesicles on the substrate surface propagating bilayer formation (Cremer & Boxer, 1999; Richter et al, 2006). In this fashion, the membrane forms in patches until the entire sample surface is covered. Factors affecting vesicle fusion include temperature, humidity, lipid concentration, incubation time as well as the presence of calcium (Puu & Gustafson, 1997; Richter et al, 2006). Ideally, the amount of lipid should be several times greater than needed to entirely cover the sample surface to ensure complete coverage and fast spreading kinetics (Puu & Gustafson, 1997). Excess vesicles can then be washed off. Also, the substrate surface should be hydrophilic or charged to aid interaction with lipid head groups in the initial attachment of vesicles to the substrate surface. Muscovite (mica) is an effective substrate in that it is hydrophilic and atomically flat making it an ideal surface for the formation of SLBs free of defects and undulations (Benes et al, 2002). In this thesis, a SLB with a mitochondria-like composition is formed on mica to observe and characterize cBid and Bax binding to planar membranes.

#### *1.6. Fluorescence fluctuation techniques to characterize planar membrane systems*

Fluorescence correlation spectroscopy (FCS) is used in conjunction with confocal microscopy to quantify the mobility and specific brightness of single fluorescent particles diffusing through the confocal volume. This method is based on the statistical analysis of the temporal fluctuations of the detected fluorescence signal (Magde et al, 1974; Groves et al, 2008). The autocorrelation function of the fluorescence signal is first calculated, and then analyzed based on assumptions about how fluorescent molecules move through the

focal volume. For example, the average residence time (diffusion time,  $\tau_D$ ) of the fluorophores in the focal volume can be obtained from the autocorrelation function and be used to calculate the fluorophore's diffusion coefficient (Thompson, 1991). The diffusion coefficient can then be used to calculate other physical parameters which give rise to the fluorescence fluctuations that are observed. One such parameter is the hydrodynamic radius, which is related to particle size. Another parameter that can be extracted is the molecular weight of diffusing particles. FCS can also differentiate between multiple fluorescent species in a sample provided that their diffusion coefficients differ sufficiently (Magde et al, 1974). Applications of FCS range from measuring the diffusion coefficients of lipids and proteins, the concentrations of fluorescent species, and the size of fluorescent particles, to characterizing molecular aggregation, binding kinetics and conformational changes (Thompson, 1991; Groves et al, 2008).

Fluorescence intensity distribution analysis (FIDA) is a complimentary technique to FCS which is applied to photon counting histogram (PCH) data. FIDA can differentiate between multiple fluorescence species in a sample by difference in specific brightness (Muller et al, 2000). In FCS, the focal volume must be at a stationary position in the sample to accurately measure diffusion times of fluorophores, however this may result in photobleaching of slowly diffusing particles. FIDA on the other hand, can be applied while scanning the focal volume through the sample in order to reduce photobleaching and obtain accurate specific brightness and concentration of fluorescent molecules (Satsoura et al, 2007).

Previously, SLBs have been characterized by FCS with lipid and protein diffusion coefficients reported. Comparing SLBs with identical lipid composition, those formed on a mica substrate displayed lipid diffusion times of 4.5 ms compared to diffusion times of 14.8 ms with borosilicate (glass) substrate (Benes et al, 2002). This suggests that mica is preferable to glass as a substrate that allows for less hindered lipid diffusion resulting in diffusion coefficients that are comparable to those observed in free-standing membranes. Chiantia et al (2006) observed a number of different fluorescent lipids and membrane probes in SLBs on mica substrate via FCS, and reported diffusion coefficients in the range of  $1\text{-}5\mu\text{m}^2/\text{s}$ . As expected, these diffusion coefficients for the liquid disordered state are somewhat smaller than what has been observed in free-standing membranes, but are comparable. Recently, FCS and FIDA were employed to characterize binding and oligomerization of fluorescent Bax in a detergent micelle system (Ivashyna et al, 2009). Previous work suggested that detergent activated Bax is oligomeric (Hsu et al 1997; Antonsson et al 2000). Furthermore, it has been reported that detergent activated Bax appears as large complexes, larger than the mass of a single detergent micelle plus a Bax monomer, when subject to analytical gel filtration (Antonsson et al, 2000). These large complexes are thought to be attributed to Bax oligomerization when activated by high concentrations of detergent. Using single molecule techniques, Ivashyna et al simultaneously determined the molecular weight of Bax-containing micelles (from FCS) and number of Bax per micelle (from FIDA). Interestingly, the brightness of Bax-detergent micelles was equal to the brightness of monomeric Bax. This suggests that Bax is a monomer prior to, during and following interaction with detergent micelles when

assayed by FIDA (Ivashyna et al, 2010). The authors suggest that the large Bax-detergent complexes previously reported using ensemble methods are likely due to incorporation of additional detergent in micelles but not Bax oligomerization. A caveat to this study was the use of detergent activated Bax that was expressed as a C-terminal truncation. In this thesis, fluorescently labelled full length recombinant cBid and Bax binding to mitochondria-like liposomes and SLBs is investigated by FCS and FIDA. By normalizing the brightness of molecules in confocal images by the molecular brightness (CPP) of a monomeric protein in solution measured by FIDA, it is possible to determine the number of monomers per oligomer.



## **2 Materials and Methods**

### *2.1 General methods*

#### *2.1.1 Materials*

All lipids were purchased from Avanti Polar Lipids Inc.: PC from chicken egg (#840051C), PE from chicken egg (#841118C), PI from bovine liver (#840042C), DOPS (#840035C), TOCL (#710335C), NBD-PE (#810118C), Liss Rhod-PE (#810146C).

Fluorophores purchased from Molecular Probes®: DiO (#D275), DiD (#D7757), ANTS (#A-350), DPX (#X-1525), Alexa Fluor 488 (#A10254), Alexa Fluor 647 (#A20347).

Fluorophores purchased from ATTO-TEC GmbH: ATTO 488 (#488-41), ATTO 495 (#495-41), ATTO 647N (#647N-41).

HiLyte Fluor 488 was purchased from Anaspec Inc. (#81164).

General reagents purchased from Bioshop Canada Inc.: NaCl (#SOD002.10), Glycerol (#GLY002.4), Tris (#TRS003.10), SDS (#SDS001.1), Arabinose (#ARB222.500), Imidazole (#IMD 508), KCl (#POC308.5), Agarose (#AGA002.1), Bis-acrylamide (#BIS001.250), PMSF (#PMS123.25), Tricine (#TRI001.1), HEPES (#HEP005.1), RNase from Bovine pancreas (#RNA888.500), Ampicillin (#AMP201.100), Tween 20 (#TWN508.500), CHAPS (#CHA001.25),  $\beta$ -mercaptoethanol (#MER2.100), Tryptone (#TRP 402.205).

General reagents purchased from Sigma-Aldrich Ltd.: Bromophenol blue (#B0126), (Coomassie) Brilliant Blue R (#B0149), Octyl  $\beta$ -D-glucopyranoside(#O8001), Hydroxylamine (#159417), DNase from Bovine pancreas (#DN25).

Materials purchased from GE Healthcare Co.: Sepharose CL-2B (#17-0140-01), G-25 fine Sephadex (#17-0032-01), DEAE Sephadex Fast Flow (#17-0710-01).

Materials purchased from Bio-Rad Laboratories Inc.: (Bradford reagent) Bio-Rad Protein Assay (#500-0006), Polyporpylene chromatography columns (#732-1010).

Reagents purchased from Caledon Laboratories Ltd.:  $MgCl_2$  (#4720-1), DMSO (#4100-1)

Reagents purchased from EMD Chemicals:  $KPO_4$ -Cl (#PX1565-1), Yeast extract (#1.03753)

Other reagents used were obtained from the following companies:

PIN HALT protease inhibitor, 0.5 M ETDA (Thermo Scientific, 1861274)

TritonX-100 (BDH Inc, R06433)

Skim milk powder (No Name Brand)

### *2.1.2 Luria Broth (LB) preparation*

LB was prepared with 10 g NaCl, 5 g yeast extract and 10 g Tryptone (or 10 g Trypticase Peptone) per litre of water. LB was autoclaved prior to use.

### *2.1.3 SDS-PAGE*

Samples were mixed with an equal volume of SDS-PAGE loading buffer (4% SDS, 2 mM EDTA, 20% Glycerol, 0.1 M Tris-Cl pH 8.9, 0.1% Bromophenol blue, 0.25 M DTT), boiled for 10 minutes at 95 °C at briefly spun down (~15 seconds) in a microcentrifuge. Equal volumes of sample (15-25 µL) was loaded per well. 10% acrylamide tricine gels were run at 30 V for 30 minutes to stack samples and 50 mA per gel for 1 hour to separate. Gels were then either stained with Coomassie and scanned, or transferred to nitrocellulose membrane for Western blotting.

### *2.1.4 Western Blotting*

Following electrophoresis, gels were washed in Transfer Buffer (Tris, 20% MeOH) and proteins were transferred onto a nitrocellulose membrane (Pall Corp., #6648) using a semi-dry transfer apparatus (BioRad Trans-blot SD) run at 60 mA per gel for 1 hour. Following transfer, the nitrocellulose blots were blocked for 30 minutes in Blocking buffer (140 mM NaCl, 10 mM KPO<sub>4</sub> pH 7.4, 0.02% azide, 0.5% skim milk powder). Blots were probed with Bax monoclonal antibody 2D2 at a dilution of 1:4000 in monoclonal antibody buffer (140 mM NaCl, 10 mM KPO<sub>4</sub> pH 7.4, 0.02% azide, 0.1% Triton X-100, and 1% BSA) overnight at 4°C. Blots were washed in TBS-T buffer (10 mM Tris-Cl pH 7.4, 0.5 M NaCl, 0.2% Tween-20) 3 times for 10 minutes per wash and incubated with a donkey anti mouse secondary antibody conjugated to Horseradish peroxidase at a dilution of 1:10000 for 2 hours at room temperature. Blots were washed in TBS-T buffer 3 times for 10 minutes per wash. Immobilon Western HRP substrate

reagents (Millipore, #WBKLS0500) were added per manufacturer instructions and the blots were exposed to film (Kodak Scientific Imaging Film #1776699) in a dark room.

### 2.1.5 Quantifying Protein and Dye by Absorption

Absorption measurements were done on the Infinite M1000 plate reader (Tecan) using a quartz 96-well plate (Hellma). 300  $\mu$ L sample volumes and a path length of 0.8 cm were used. Buffer or solvent without dye/protein was used as a blank. Protein was quantified by absorbance at 280 nm. When quantifying dyes the following molar extinction coefficients and correction factors were used (Table 1).

**Table 1: Absorbance properties of dyes.**

Fluorophore	Peak absorbance (nm)	Extinction coefficient ( $M^{-1}cm^{-1}$ )	Correction Factor
Alexa Fluor 488	493	72000	0.11
ATTO 647N	644	150000	0.05
ATTO 488	501	90000	0.10
ATTO 495	495	80000	0.39
HiLyte Fluor 488	504(MeOH) / 502(H <sub>2</sub> O)	80460/70000	0.11
DiO	484	154000	
DiD	644	193000	

When quantifying labeled protein, correction factors were applied to account for dye absorption at 280 nm. The absorbance of the sample at the dye peak absorbance wavelength ( $A_{\text{visible}}$ ) is multiplied by the correction factor to give the dye absorbance at 280 nm. The concentration of labelled protein was then calculated as:

$$[\text{protein}] = \frac{A_{280_{\text{sample}}} - A_{280_{\text{blank}}} - (A_{\text{visible}} * \text{correction factor})}{(\text{Extinction coefficient} * 0.8)}$$

## 2.2 Preparing lipid films and liposomes

PC, PE, PI, DOPS and TOCL were obtained dissolved in chloroform and combined in a borosilicate tube to make a 1 mg lipid film with a mitochondria-like composition according to Table 2 below. In some cases, the lipid mix contained fluorescently labelled NBD-PE or Liss Rho-PE and the amount of non-fluorescent PE was adjusted accordingly. Lipophilic dyes DiO and DiD dissolved in chloroform were also added as membrane tracers in some experiments.

**Table 2: Lipids and tracers used to prepare mitochondria-like liposomes and SLBs.**

Lipid/Dye	Molecular Mass (g/mol)	Mass %	Mol %
PC	770.123	45.9	48
PE	726.076	25.3	28
PI	902.133	11.2	10
DOPS	810.025	10.1	10
TOCL	1501.959	7.5	4
NBD-PE	898.117	0.5	4.5
Rhodamine-PE	1275.678	0.05	0.32
DiO	881.717	0.00002-0.002	0.00018-0.018
DiD	1052.075	0.00002-0.002	0.00015-0.015

Chloroform was evaporated under a stream of nitrogen gas and trace amounts were further removed by vacuum drying for 2 hours. Films were then covered with argon gas, stored at -20 °C and used within 2 weeks. Lipid films were hydrated in 1 mL of 1X assay buffer (10 nM HEPES pH 7, 0.2 M KCL, 1 mM MgCl<sub>2</sub>, and 0.2 mM EDTA) and vortexed 2-3 times for 10 seconds to form vesicles. To form unilamellar vesicles, the vesicle solution was then freeze-thawed in liquid nitrogen 10 times and passed 11 times through a lipid extruder (Avanti, #610000) with membrane filter with pore sizes of 50,

100 or 200 nm (Whatman, #800308, #800309, #800281). Vesicles were kept on ice until use and stored for a maximum of 2 days.

## 2.3 Protein Purification

### 2.3.1 Purification of Bax

0.5-1 µg plasmid encoding Bax constructs summarized in Table 3 were transformed into 50 µL *E. coli* BL21 arabinose inducible (AI) cells by electroporation (Eppendorf Electroporator 2510) at 2000 V. Following electroporation, 500 µL of LB was added and the cells were allowed to recover for 30 minutes at 37 °C. 10 µL of cells were plated on 1.5% agar LB-ON containing 0.1 mg/mL ampicillin overnight at 37 °C. Single colonies were screened by growing 5 mL cultures for 4 hours and inducing with 2% arabinose for 3 hours. 1 mL samples of cells prior to and after induction were spun down and run on SDS-PAGE gels and Western blots were performed to assess the amount of protein produced. Uninduced samples were also frozen and stored. Colonies that showed highest amount of Bax protein after induction were selected for large scale growth. 100 mL LB containing 0.1 mg/mL ampicillin was inoculated with a small amount of frozen cells on the end of a pipette tip and grown overnight at 30 °C with shaking. Overnight seed cultures were used to inoculate 4-6 L of LB for large scale growth. The cultures were grown at 37 °C with shaking until an OD between 0.6-0.8 was reached. Induction was achieved by adding arabinose to 0.2% for 5 hours at 30 °C with shaking. Cells were spun down at 5000 g for 30 minutes at 4 °C in a Beckman centrifuge (J-26, JLA 8.1000 rotor). Supernatant was decanted and cell pellets were weighed and frozen at -20 °C, or kept on ice for immediate use. The pellet was thawed and

resuspended in 10 mL/2.5 g lysis buffer (10 mM HEPES pH 7, 100 mM NaCl, 0.2% CHAPS, 1 mM PMSF, 1X PIN). A small amount of DNase and RNase ( $\ll 1$  mg) was also added. PMSF and PIN were added just prior to lysis. Clumps of cells were broken by vortexing and passage through a 16 gage needle. Cells were lysed by at least 2 passes through a French Press or Homogenizer (Avestin V-EmulsiFlex-C5) at a pressure of 1000psi. Cell debris was removed by centrifugation at 15000 g for 30 minutes at 4 °C (Beckman JE, JA 25.50 rotor). The supernatant was incubated with 1.5-2 mL Chitin resin (NEB, #S6651L) for 1.5 hours at 4 °C with mixing. The slurry was then added to a 20 mL column (BioRad) that retained the resin. The flow through was passed once more over the bed of resin. The column was then washed with 50 mL of wash Buffer (10 mM HEPES pH 7, 500 mM NaCl, 0.5% CHAPS), followed by flushing with 3 bed volumes of cleavage buffer (100 mM HEPES pH 7, 200 mM NaCl, 0.2 mM EDTA, 0.1% CHAPS). The cleavage buffer also contained 100 mM  $\beta$ -mercaptoethanol in the case of WT Bax and eGFP-Bax and 100 mM hydroxylamine pH 7 for all other Bax mutants. The column was incubated with 1 mL of cleavage buffer remaining above the bed volume for 36-48 hours at 4 °C. (During eGFP-Bax purification, the column was wrapped in foil). The protein was then eluted in cleavage buffer and collected in 4x1 mL fractions. Samples of eluted protein were run by SDS-PAGE to ensure purity.  $\beta$ -mercaptoethanol and hydroxylamine were removed by dialysis in storage buffer (10 mM HEPES, 200 mM NaCl, 0.2 mM EDTA, 10% glycerol). Dialysis tubing with 10-14 kDa cut-off (Viscase, Membra-cel MD10-14) was used. 1 L dialysis buffer was changed three times typically in 6 hour-overnight-4 hour changes. Following dialysis, the Bax concentration was

determined by absorption at 280 nm. Typically the 2 most concentrated fractions were pooled for further use. Protein was either labelled, or made into aliquots and frozen in liquid nitrogen and stored at -80 °C.

**Table 3: Summary of Bax constructs.**

<b>Bax construct</b>	<b>Plasmid #</b>	<b>Mutations (to WT)</b>	<b>Extinction coefficient (<math>M^{-1}cm^{-1}</math>)</b>	<b>Description</b>
WT Bax	1572		37000	Wild-type human Bax C-terminal fusion to intein/chitin binding domain
Bax 126C	1731	C62A	36940	Single Cys mutant, only Cys at position 126
Bax 62C	1732	C126A	36940	Single Cys mutant, only Cys at position 62
Bax Cys-	1730	C62A, C126A	36880	Double mutant, contains no Cys
Bax 47C	2035	C62A, C126A, L47C	36940	Single Cys mutant, only Cys at position 47
Bax 5C	1999	C62A, C126A, G5C	36940	Single Cys mutant, only Cys at position 5
Bax 3C	1997	C62A, C126A, G3C	36940	Single Cys mutant, only Cys at position 3
Bax 134C	1736	C62A, C126A, R135C	36940	Single Cys mutant, only Cys at position 134
eGFP-Bax	2194		72000	N-terminal fusion to eGFP with 3 AA linker + A206K eGFP monomerizing mutation

### 2.3.2 Purification of Bid

Recombinant murine Bid with an N-terminal His-tag and C30S mutation (plasmid #2118) was purified as described for the Bax protein. Induction of *E. coli* BL21 AI cells was achieved by addition of 0.2% arabinose for 3 hours at 37 °C. Cell pellets were solubilised in lysis buffer (10 mM HEPES pH 7, 100 mM NaCl, 10 mM imidazole, 1 mM



PMSF, 1X PIN). A small amount of DNase and RNase ( $\ll 1$  mg) was also added. PMSF and EDTA-free PIN were added just prior to lysis. Clarified lysate was incubated with 1.5 mL Ni-NTA agarose resin (Qiagen, #1018244) for 1.5 hours at 4 °C with mixing. The slurry was then added to a 20 mL column (BioRad) that retained the resin. The flow through was passed once more over the bed of resin. The column was then washed with 50 mL of Wash Buffer (10 mM HEPES pH7, 300 mM NaCl, 1% CHAPS, 10 mM imidazole). The protein was eluted in buffer (10 mM HEPES pH 7, 100 mM NaCl, 200 mM imidazole, 0.1% CHAPS, 10% glycerol) and 1 mL fractions were collected. Samples of each collected fraction were run by SDS-PAGE and quantified by Bradford Assay. Fractions were snap frozen in liquid nitrogen and stored at -80 °C. When needed, a fraction was thawed on ice and either subject to cleavage with caspase-8 or labelled with a fluorophore prior to cleavage. For the cleavage reaction, the Bid buffer was adjusted (40 mM HEPES pH 7, 100 mM NaCl, 200 mM imidazole, 0.1% CHAPS, 1mM EDTA, 10mM DTT) by the addition of HEPES, CHAPS, EDTA, and DTT to the fraction. 500 units of caspase-8 was added and incubated for 16-18 hours at room temperature on a rotator. (If the protein was labelled prior to cleavage, the reaction was wrapped in aluminum foil). Following cleavage, the protein was dialysed 4x1 L in Bid storage buffer (10 mM HEPES pH 7, 100 mM NaCl, 0.1 mM EDTA, 10% glycerol), quantified by Bradford assay, frozen in liquid nitrogen and stored at -80 °C. For tBid production, following dialysis into storage buffer, the sample was incubated for 1.5 hours with 1 mL of Ni-NTA agarose resin at 4 °C on a rotator. The slurry was then loaded onto a column (BioRad) and the flow through was passed once more over the bed of resin. The protein

was eluted in 3 mL of Bid elution buffer containing octylglucoside (10 mM HEPES pH 7, 100 mM NaCl, 0.1 mM EDTA, 10% glycerol, 1.2% w/v octylglucoside). Centrifugation was used to remove octylglucoside detergent and concentrate the protein by using a centrifugal filter unit (Millipore, Amicon Ultra Ultracel 10K-UFC901024) at 2000 g for 15 minute periods. Eluted tBid was diluted to ~10 mL in Bid storage buffer and spun until 0.5-1 mL remained. The process of diluting and spinning was repeated 4 times. Protein concentration was determined by Bradford assay, and aliquots were frozen in liquid nitrogen and stored at -80 °C.

#### *2.4 Protein labelling*

Typically, single cysteine mutants were subject to labelling with thiol reactive fluorescent dyes. In all cases the thiol reactive group on the fluorophore was a maleimide with the exception of NBD which reacted via iodoester. A stock solution of dye was created by dissolving solid dye in DMSO. Dye concentration was determined by absorption using a dilution of the dye stock in methanol. Protein to be labelled was in storage buffer or was dialyzed into storage buffer to which CHAPS was added to a final 0.5% w/v. Labelling reactions contained dye at a 10-20X molar excess to protein and incubated at room temperature for 2-6 hours covered in foil on a rotator. In some cases, labelling conditions included a 2X molar excess of TCEP, 4 M Urea or pH 7.5 (labelling conditions are summarized in Table 5, see Results section). Unreacted dye was quenched by addition of 1 mM DTT and rotated for 10 minutes. Free dye was separated from labelled protein by gel filtration in a 15 mL G25 fine Sephadex column equilibrated with storage buffer. The labelling reaction (~1 mL) was added to the top of the column, and

250  $\mu$ L fractions were collected. Protein and Dye concentrations in collected fractions were determined by absorption. The degree of labelling was calculated as:

$$\text{Labelling efficiency} = [\text{dye}]/[\text{protein}] * 100$$

Fractions with acceptable protein concentration and good labelling efficiency were dialysed in storage buffer, aliquoted, frozen in liquid nitrogen and stored at  $-80^{\circ}\text{C}$ .

### *2.5 ANTS release pore formation assay*

The fluorophore ANTS and collisional quencher DPX were encapsulated inside mitochondria-like liposomes by adding 5.1 mg ANTS and 19.1 mg DPX to a 1 mg lipid film prior to hydration. Films were hydrated in 1X Assay Buffer, freeze-thawed 10 times and extruded 11 times through a 50 nm, 100 nm or 200 nm filter. To separate liposomes from unencapsulated dye, the solution was passed over a 12 mL CL-2B Sepharose column and eluted with 1X Assay buffer. 1mL fractions were collected and liposome-containing fractions were visually identified by turbidity. The 2 most concentrated fractions were pooled and kept on ice for use. Fluorescence measurements were performed on the Tecan and Envision (Perkin Elmer) plate readers. Conditions used on the Tecan were as follows: Excitation: 355 nm/bandwidth: 5 nm, Emission: 520 nm/bandwidth: 12 nm, gain: 140, z-position: 22500. Conditions used on the Envision were as follows: Excitation filter: Umbelliferone 355, Emission filter: YFP 535, gain: 20, flashes: 10, measurement height: 6.5 mm. 100  $\mu$ L reactions contained 0.04-0.80 mg/mL lipid, 0-20 nM cBid and 0-200 nM Bax in 1X Assay Buffer. Prior to adding protein, the background fluorescence of the liposomes alone was measured for 30 minutes. Proteins

were added and the reaction was allowed to proceed for 2-3 hours until endpoint. Finally, 0.5% Triton X-100 was added to lyse all remaining liposomes and measurements were taken for 10 minutes. Measurements were taken at 2 minute intervals. Pore forming activity was measured as an increase in ANTS fluorescence as it was released from liposomes and dequenched. This was calculated as the percent of ANTS released from liposomes normalized to triton release:

$$\% \text{ ANTS release (t)} = (F_{(t)} - F_{\text{background}}) / (F_{\text{triton}} - F_{\text{background}}) * 100 \quad (1)$$

where,  $F_{\text{background}}$  is the average background value,  $F_{\text{triton}}$  is the average value after adding Triton and  $F_{(t)}$  is the value at time point, t, after adding protein. To correct for bleedthrough when using fluorescently labelled proteins, the first measurement after adding protein was taken as the background value.

### *2.6 Bax oligomerization measured by FRET*

Bax single cysteine mutants were labelled with DAC and NBD which form a FRET pair with DAC as the donor and NBD as the acceptor fluorophore. Labelling conditions for DAC-Bax126C are summarized in Table 5. NBD-Bax134C was obtained from Mina Falcone. 300  $\mu$ L samples were prepared in a 96-well quartz plate (Hellma) and measured in the Tecan plate reader using excitation at 383 nm and recording emission at 463 nm. Sample components were added in the following order: Assay buffer, liposomes, 20 nM DAC-Bax126C (donor), 100 nM NBD-Bax134C (acceptor, when present) and 24 nM tBid. Prior to adding tBid, samples were allowed to equilibrate and the background fluorescence,  $F_B$ , was recorded. Following the addition of tBid, donor fluorescence was

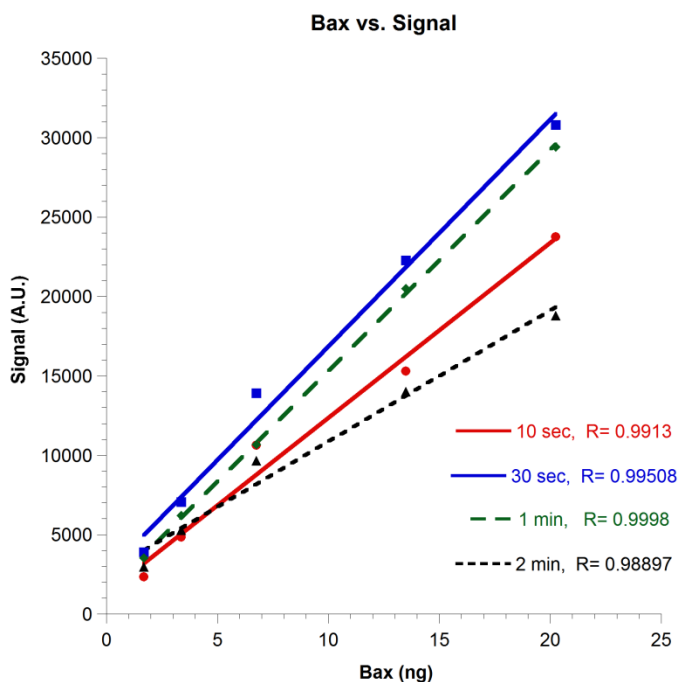
recorded over time,  $F(t)$ . Bax oligomerization was measured as a reduction of donor fluorescence due to FRET by considering the normalized donor fluorescence =  $[F(t) - F_B] / [F(0) - F_B]$

Controls with no liposomes or unlabelled WT Bax substituted for acceptor NBD-Bax134C were performed to ensure no FRET occurred in these cases.

### *2.7 Characterizing Bax binding to liposomes by quantitative Western blot*

250  $\mu$ L reactions containing different concentrations of lipid, 20 nM tBid and 100 nM Bax were carried out in 1X Assay Buffer and incubated for 2 hours at 37 °C. If fluorescent vesicles and proteins were used, the protein binding was further assessed using fluorescence fluctuation measurements. Reactions were then passed over a 2.5 mL CL-2B Sepharose column to separate vesicle-bound and free protein and eluted with Assay buffer in 12x250  $\mu$ L fractions. The protein concentration in each fraction was determined by Western blot or fluorescence measurements.

For quantitative Western blot, it is necessary to ensure that a linear signal-to-protein relationship exists in the range of protein concentration used. A titration in the range of concentrations measured in the collected fractions (1-50 nM) was done to ensure a linear relationship between the amount of Bax in a given fraction and the signal detected (Figure 2). A linear-Bax-to-signal relationship existed for all exposure times used.



**Figure 2: Bax vs. Western blot signal displays a linear relationship.** A titration of Bax in the expected concentration range found in targeting experiments was performed. The blots were exposed to film for the exposure times indicated and signal was quantified as explained in the text. All data were fit with a linear function with the R values displayed.

Western blots were performed to assess the amount of Bax bound to membranes.

Following size-exclusion chromatography, collected fractions were run by SDS-PAGE gels and transferred to nitrocellulose membrane and probed with Bax monoclonal antibody 2D2. For all results presented, 30 s and 1 min exposure times were used.

Developed films were scanned and quantified using ImageJ. Each scanned blot was converted to an 8-bit image, inverted for colour and the background intensity around each band was subtracted based on the “rolling ball” algorithm described by Sternberg (1983).

The summed intensity from fractions 1-5 was taken as the amount of membrane-bound Bax. Binding was quantified as follows:

$$\% \text{ Bax bound} = \text{intensity of fractions 1-5} / \text{intensity of all protein fractions} * 100 \quad (2)$$

## *2.8 Fluorescence fluctuation experiments*

### *2.8.1 Measurements*

Measurements were performed on the Insight confocal microscope (Evotech Technologies) set up to compute autocorrelation functions and photon counting histograms simultaneously from the recorded fluorescence signal. Excitation was done using a 488 nm continuous wave laser (Sapphire 488-20 CDRH, Coherent), a 523 nm pulsed laser (Picoquant) or a 637 nm continuous wave laser (Radius 635-25, Coherent). Laser beams were attenuated by a neutral density filter and a beam expander then passed through a dichroic and into the objective via a scanning mirror. A 40X, water immersion, 1.15 NA objective (Olympus, UAPO) was used. The scanning mirror was controlled by two piezoelectric actuators (Physik Intrumente, S-334). Fluorescence emission from the sample was collected by the same objective, passed through a dichroic mirror and band pass filter prior to detection by avalanche photodiodes capable of single photon counting (Perkin Elmer, SPCM-CD3017).

Prior to taking measurements, the microscope was aligned to ensure optimal signal to noise. The instrument was aligned in “FCS” or “FIDA” mode by adjusting the pinhole diameter for a smaller (FCS) or larger (FIDA) focal volume. Calibration dyes with a known molecular brightness (Alexa 488 and Alexa 647) were used to align the blue and red channels respectively. The calibration samples were prepared to resemble the assay samples as closely as possible. For measurements of supported bilayer samples, a calibration coverslip with mica was used. All alignment steps were performed with the beams focused completely in solution, with the focal volume approximately 150  $\mu\text{m}$

above the glass or the glass/mica interface. For imaging SLBs the focal volume was brought down to 30  $\mu\text{m}$  above the mica surface, as detected by a reflected laser beam, for the final round of calibration. This was the minimum height above the interface that signal could still be detected without loss. Alignment was done in successive rounds until the expected count rate per particle for the calibration dyes was observed. Following alignment, FCS and FIDA measurements of the buffer alone, calibration dyes in buffer and the soluble monomeric fluorescent protein in buffer were performed.

Fluorescence measurements for Bax binding to vesicles were done with the instrument in FIDA alignment. 250  $\mu\text{L}$  samples were measured in a 96-well plate with coverslip bottom (Whatman, 7706-2370). All measurements were performed in solution at a distance of 150  $\mu\text{m}$  above the glass. FCS measurements were performed without beam scanning and FIDA measurements with circular beam scanning (radius of scan: 45  $\mu\text{m}$ , frequency of scanning: 25 Hz). It was assumed that beam scanning eliminated photobleaching. Measurements were recorded for one channel at a time with illumination with one laser to reduce crosstalk and bleedthrough between channels.

Measurements involving SLBs were done in FCS alignment. For measurements of protein in solution, the beam was focused at a distance of 150  $\mu\text{m}$  above the glass/mica interface. For measurements at the plane of the membrane it was necessary to first locate the membrane by acquiring an image through the X, Z plane. The beam was focused at coordinates near the centre of the membrane in the image prior to taking measurements.



### 2.8.2 FCS Analysis

Data analysis of fluorescence fluctuation measurements was performed with Acapella research software. Analysis was done assuming a 3D Gaussian focal volume with a radius,  $w_0$ , and height,  $z_0$ . For a species with diffusion coefficient  $D$  and in the absence of beam scanning, the autocorrelation function is expected to have the form (Rigler et al, 1993):

$$G(t) = \frac{1/N}{\left(1 + \frac{t}{\tau_D}\right) \sqrt{1 + \frac{t}{S^2 \tau_D}}} \left[ 1 + \frac{T}{1-T} e\left(\frac{-t}{\tau_T}\right) \right], \quad (3a)$$

where  $N$  is the average number of fluorophores in the focal volume,  $\tau_D = w_0^2/4D$  is the average residence time of the fluorophore in this volume,  $\tau_T$  is the relaxation time of the fluorophore triplet state,  $T$  is the average fraction of fluorophores in the triplet state and  $S = z_0/w_0$  is the aspect ratio of the focal volume.

When beam scanning is present, the autocorrelation function is expected to become:

$$G_S(t) = G(t) e\left[ -\frac{\left(\frac{t}{\tau_S}\right)^2}{\left(1 + \frac{t}{\tau_D}\right)} \right], \quad (3b)$$

where  $\tau_S = w_0/(2\pi fR)$  would be the residence time of an immobile fluorophore in the scanning detection volume,  $f$  is the scan frequency and  $R$  is the radius of scanning.

When multiple fluorescent species are present, additional terms for the additional diffusing species must be added so that the autocorrelation function becomes:

$$G(t) = 1 + \frac{1}{N} \sum_{i=1} \frac{A_i}{\left(1 + \frac{t}{\tau_{Di}}\right) \sqrt{1 + \frac{t}{S^2 \tau_{Di}}}} \left[ 1 + \frac{T}{1-T} e\left(\frac{-t}{\tau_{Ti}}\right) \right], \quad (3c)$$

where  $A_i$  is the fractional contribution of fluorescent species,  $i$ , to the total number of detected particles,  $N$ .

### 2.8.3 FIDA

Using FIDA, the molecular brightness (i.e. the fluorescence intensity produced by a single fluorophore placed at the centre of the detection volume) and concentration of a fluorophore diffusing in solution can be accurately measured. For FIDA, photon counting histograms were fitted with one or two-component models assuming the presence of one or two types of diffusing fluorescent species according to Satsoura et al. (2007). The background signal was fixed at the value obtained for buffer alone with no fluorophore present. The parameters  $A_0$  and  $A_1$ , which describe the light excitation profile, were fixed at values determined for the analysis of a calibration dye (Alexa 488 when using the blue laser, Alexa 647 when using the red laser) diffusing in buffer.

### 2.8.4 Dye photostability in fluorescent protein constructs

To determine the laser power at which molecular brightness saturates for each dye, the laser power was varied between 5  $\mu\text{W}$  - 350  $\mu\text{W}$ . FCS and FIDA measurements were recorded at each laser power. Fluorescence intensity as a function of laser power was fit with (Davis et al, 2005):

$$F(I) = \frac{C}{\left(1 + \frac{I}{I_s}\right)}, \quad (4)$$

where  $I$  is the laser power in  $\mu\text{W}$ ,  $I_s$  is the laser power at which the molecular brightness saturates and  $C$  is a constant which takes into account: the net collection and detection efficiency, fluorescence decay rate, fluorescence lifetime, phosphorescence lifetime and

triplet crossing yield. The diffusion time,  $\tau_D$ , was also measured by fitting the data with Eq. 3a to assess the effect of laser power on this parameter.

A characteristic photobleaching time (i.e. the time required to photobleach a fluorophore at a given laser power) was also measured for each dye by scanning the confocal volume at speeds varying between 0-10000  $\mu\text{m/s}$  at high laser power (250  $\mu\text{W}$ ) and recording FIDA data. Normalized fluorescence intensity was plot as a function of scan speed and fit with the following equation (Satsoura et al, 2007):

$$F(v) = NB\tau_P \left( \frac{3}{4\tau_D} + \frac{2v}{3w_0} \right) \left\{ 1 - e^{\left[ -\frac{1}{\tau_P \left( \frac{3}{4\tau_D} + \frac{2v}{3w_0} \right)} \right]} \right\}, \quad (5)$$

where  $v$  is the scan speed,  $w_0$  is the radius of the confocal volume,  $\tau_D$  is the average residence time of the fluorophore in the confocal volume and  $\tau_P$  is the photobleaching time.

### 2.8.5 FCS analysis of eGFP-Bax binding to liposomes

Autocorrelation functions obtained for samples with eGFP-Bax incubated with liposomes were analysed assuming the presence of two fluorescent species: unbound (soluble) eGFP-Bax and liposomes with bound eGFP-Bax. Soluble Bax was assumed to have a much faster diffusion time than Bax bound to liposomes. For FCS analysis, the diffusion time of soluble Bax ( $\tau_{D1}$ ) was fixed at the value for soluble monomeric Bax obtained during the calibration step,  $\sim 0.5$  ms. The diffusion time of liposomes with bound fluorescent Bax ( $\tau_{D2}$ ) was left to vary. Analysis resulted in two amplitudes which are related to the fraction of unbound eGFP-Bax and vesicles with bound eGFP-Bax. The

amplitudes ( $A_i$ ) are related to the fraction of particles,  $f_i$  and the molecular brightness of each species  $Q_i$  according to:

$$A_i = \frac{f_i Q_i^2}{(f_1 Q_1^2 + f_2 Q_2^2)} \quad (6)$$

To a very fine approximation (at low protein concentration), the fraction of bound protein is:

$$f_{\text{bound}} = A_2$$

Using this method, the fraction of bound eGFP-Bax is accurate when there is one or less Bax molecule bound per liposome ( $Q_2=Q_1$  and  $A_2=f_2$ ). But in cases where there is multiple Bax molecules bound to a vesicle ( $Q_2>Q_1$ ), this method leads to an overestimate of the bound protein fraction ( $A_2>f_2$ ).

#### 2.8.6 FIDA of eGFP-Bax binding to liposomes

FIDA analysis of PCHs resulted in the molecular brightness ( $Q_i$ ) and average number of fluorophores ( $N_i$ ) in the detection volume. FIDA can accurately determine the number of particles of different fluorescent species (assuming their molecular brightness differs) in the sample even when beam scanning is used. Analysis in the red (liposome) channel was performed assuming one component, while analysis of the green (eGFP-Bax) channel was done assuming two components corresponding to unbound ( $Q_1^{\text{green}}$ ,  $N_1^{\text{green}}$ ) and vesicle-bound eGFP-Bax ( $Q_2^{\text{green}}$ ,  $N_2^{\text{green}}$ ). For FIDA, the molecular brightness of soluble monomeric eGFP-Bax ( $Q_1^{\text{green}}$ ) was fixed at 8kHz and  $Q_2^{\text{green}}$  was left to vary.

The average number of eGFP-Bax molecules per liposome with at least one Bax was calculated as:  $n = Q_2^{\text{green}} / Q_1^{\text{green}}$ ,

and the total eGFP-Bax concentration as:  $N^{\text{green}} = N_1^{\text{green}} + nN_2^{\text{green}}$

Combining the above 2 equations, an estimate for the fraction of bound eGFP-Bax was calculated as:

$$f_{\text{boundFIDA}} = \frac{N_2^{\text{green}} Q_2^{\text{green}} / Q_1^{\text{green}}}{N_1^{\text{green}} + N_2^{\text{green}} Q_2^{\text{green}} / Q_1^{\text{green}}} \quad (7)$$

The above equation returns an exact value when  $Q_2 > Q_1$  (more than 1 Bax bound per liposome), however when  $Q_2 = Q_1$  FIDA cannot distinguish between bound and soluble Bax and leads to an underestimation of bound eGFP-Bax.

FIDA data from the red (liposome) channel was also analyzed to determine the exact concentration of lipid in samples,  $N^{\text{red}}$ . The molecular brightness of vesicles,  $Q^{\text{red}}$ , was fixed to the value determined from a calibration sample of only liposomes at high concentration.

The fraction of liposomes carrying eGFP-Bax was:  $F = N_2^{\text{green}} / N^{\text{red}}$  (8)

The measured Bax-to-liposome ratio was:  $r = N^{\text{green}} / N^{\text{red}}$

Actual protein and liposome concentrations were calculated as  $c = NV_0$ , where  $V_0 = 10$  fL is the experimentally determined focal volume in FIDA alignment.

### 2.9 A Simplified model for Bax binding to liposome membranes

Bax binding to liposomes, as measured in FIDA experiments, can be compared to a simple binding model which assumes a partition between soluble and membrane bound Bax according to (Ben-Tel et al, 1996):

$$P_{\text{bound}} = KLP_{\text{free}}, \quad (9)$$

where  $K$  is the apparent association coefficient ( $K_D=1/K$ ) between protein and lipid,  $L$  is the lipid concentration and  $P_{bound}$  and  $P_{free}$  are the concentrations of membrane bound and soluble protein, respectively. Thus, the fraction of bound Bax depends on the Bax-to-lipid ratio according to:

$$f_{bound} = \frac{KP}{KP + \left(\frac{P}{L}\right)} = \frac{KL}{1 + KL}, \quad (10)$$

where  $P$  is the total protein concentration. The ratio of bound Bax to liposomes can be calculated as:

$$m(P/L)f_{bound},$$

where  $m$  is the number of lipids in a liposome. It is expected that at high  $P/L$ , Bax will be randomly distributed on liposomes. In this case, the average number fraction of liposomes carrying at least one Bax,  $f_{bound}^L$ , and the average number of Bax bound per liposome,  $n$ ,

can be calculated as:

$$f_{bound}^L = 1 - e^{-\frac{mKP}{1+KL}} \quad (11)$$

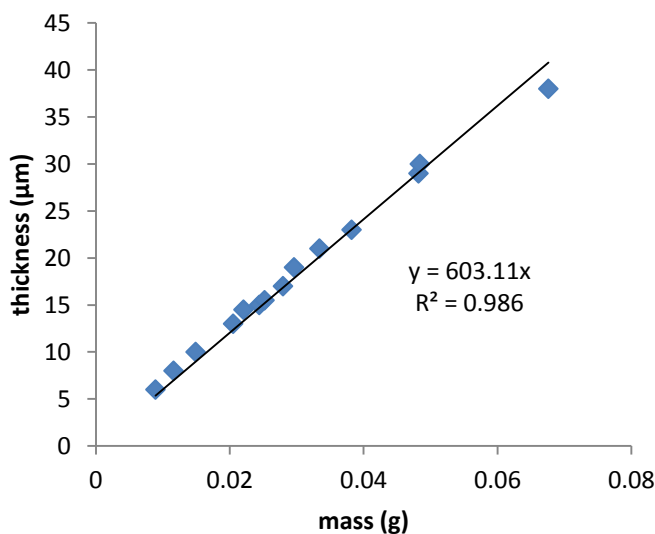
and

$$n = \frac{mKP/(1+KL)}{1 - e^{-mKP/(1+KL)}} \quad (12)$$

## 2.10 Supported Lipid Bilayers

### 2.10.1 Mica substrate preparation

V-1 grade mica obtained in round 25mm diameter discs (SPI Supplies, #01926-MB) was cleaved to 6-12 $\mu$ m thick and glued to #1.5 glass coverslips (Biotech, #40-1313-0319). Thickness of cleaved mica was assessed by relating the mass of circular cut pieces of mica to thickness using a calibration curve (Figure 3). It was possible to reproducibly cleave mica to a thickness between 6 and 12 $\mu$ m. Coverslips were heated to 50 °C and 10.5  $\mu$ L of optical adhesive (Norland Products, #NOA 88) was placed in the



**Figure 3: Constant relating mica mass to its thickness.** Circular pieces of mica of varying thickness were weighed on an analytical balance accurate to 0.0001 g and thickness was measured with a Mitutoyo micrometer accurate to 1 µm. A constant of 603 was calculated relating mass to thickness. The difference between the measured thickness of a piece of mica and the thickness predicted by the linear fit is ~0.5 µm. Therefore a cleaved circular piece of mica weighing less than 0.019 g has a thickness less than 12 µm.

centre of the coverslip and allowed to heat up to aid in even spreading. Cleaved mica was pressed onto the centre of the coverslip and left for ~2 minutes at 50 °C to allow the surface to be coated with glue. Care was taken not to trap any air bubbles in the glue. The mica was pressed to the glass and excess glue at the edge of the mica was wiped off using a kimwipe. The sample was then placed under a UV lamp for 30 seconds to fix the glue. The total sample thickness (coverslip + glue + mica) was verified to be less than 220 µm using a calliper micrometer (Mitutoyo, #500-196). Just prior to incubating the substrate with vesicles, the top layers of mica were lifted off with clear packing tape to expose a clean, freshly cleaved surface.

### 2.10.2. Planar membrane formation

Mitochondria-like 100 nm liposomes at a lipid concentration of 0.5mg/mL in 1X Assay buffer were added to a ~400 µL perfusion chamber (Bioptech, #060319-2) containing the mica substrate ensuring no bubbles were trapped in the chamber. Typically 600 µL-1 mL liposomes was injected. The chamber was incubated at 37 °C for one hour

to aid in vesicle fusion and spreading. Excess vesicles were removed by washing the membrane with 3-5 mL of buffer (Assay buffer). Buffer was pumped through the chamber at a rate of approximately 1.5 mL/min by hand using a syringe (roughly 1 drop a second from the chamber outlet). While washing, care was taken to avoid injecting bubbles into the chamber. Following washing with buffer, the membrane sample was incubated at 37 °C for 10-15 min to recover. The sample was then imaged or protein was added. WT cBid or fluorescent Atto647-cBid was diluted in Assay buffer and added at a concentration of 400 pM in 1 mL injection volume. For some experiments, fluorescent HiLyte488-Bax, unlabelled WT Bax or unlabelled WT Bcl-XL was diluted in Assay buffer and added at a concentration of 2 nM in 1 mL injection volume concurrently with 400 pM cBid. Protein was pumped through the chamber at approximately 1.5 mL/min and care was taken not to inject bubbles into the chamber. Once protein was added, the samples were incubated at 37 °C for 10-15 min (cBid alone) or for 2 hours (cBid with Bax/Bcl-XL) prior to imaging. Prior to imaging, samples with unbound fluorescent Bax in solution were washed with 1 mL of buffer.

## *2.11 Conditions for resolving single molecules on planar membrane*

### *2.11.1 Resolution of the microscope*

According to Rayleigh's criterion, the resolution of the microscope can be no better than the Airy disc radius (Inoue, 1990). Thus, two point sources can only be just resolved if they are separated by at least the distance of the Airy disc radius; correspondingly the center of the Airy disc of the first point falls on the first minimum of the Airy pattern of the second point (Hecht, 1998). This is summarized by the equation:



$$d = 1.22\lambda/(2n \sin \alpha) \approx 0.61\lambda/NA$$

where  $d$  is the Airy disk radius (resolution limit),  $\lambda$  is the wavelength of light,  $n$  is the refractive index of the medium,  $\alpha$  is the opening angle of the lens aperture, and  $NA = 2n \sin \alpha$  is the numerical aperture.

For 633 nm excitation and using a 40X water objective with  $NA = 1.15$  the airy disc radius is given by:  $d = 0.61\lambda/NA = 0.61(633)/(1.15) = 336$  nm. For the blue 488 nm laser,  $d = 259$  nm. The Airy disc radius can also be experimentally determined by the diffusion rates of dyes in solution, since it corresponds to the radius of the focal volume ( $w_0$ ) in the

focal plane:

$$\tau_D = \frac{w_0^2}{4D} \quad (13)$$

Where,  $\tau_D$  is the residence time of the fluorophore in the focal volume,  $D$  is the diffusion coefficient for the fluorophore, and  $w_0$  is the radius of the focal volume (Airy disc radius). This value for the Airy disc radius obtained experimentally may deviate from the calculated theoretical value, but will be more accurate as to the actual resolution of the instrument.

### *2.11.2 Conditions for single molecule detection*

In order to observe single proteins, the concentration must be such that a homogenous distribution of protein on the membrane allows for adequate spatial separation between individual molecules that is greater than or equal to the Airy disc radius. Using the red laser, assuming a sample area of  $1\text{cm}^2$ , a homogenous distribution of

protein and 100% binding to the membrane, the number of molecules, N, that can be resolved is:

$$N = \text{Sample area/area of single resolved molecule} = 10^{15} \text{ nm}^2 / \pi(336 \text{ nm})^2 = 4.68 \times 10^{-16} \text{ mols}$$

Assuming a sample volume of  $V = 400 \mu\text{L}$ , the concentration of protein necessary to resolve individual molecules is:  $C = n/V = 0.00117 \text{ nM}$ . With 100% binding to the planar bilayer, the concentration at the membrane is then  $2.82 \text{ protein}/\mu\text{m}^2$ .

This represents the highest theoretical amount of protein that could be added to membrane to still resolve individual molecules at the highest possible resolution of the microscope. In practice, the amount of Bid could be somewhat higher to account for not all Bid binding to the membrane and less than 100% labelling efficiency.

### *2.12. Confocal Image Acquisition*

Images were acquired on the Insight confocal microscope. Prior to imaging, the instrument was aligned in the FCS configuration, using a larger excitation beam diameter producing a smaller focal volume. A  $10 \times 10 \mu\text{m}$  or  $100 \times 100 \mu\text{m}$  area was imaged by raster scan into  $100 \times 100$  pixel images. Typically,  $100 \times 100 \mu\text{m}$  images through the X, Z plane were first acquired to locate the membrane in the z-dimension and to ensure imaged areas were free of defects (scratches on the mica substrate or unfused vesicles attached to the membrane). The plane of the membrane was then imaged by acquiring a stack of  $10 \times 10 \mu\text{m}$  images through the X, Y plane in the region of the membrane starting below the plane of the membrane and finishing above the membrane at  $1 \mu\text{m}$  intervals in the z-dimension.

Imaging conditions used were optimized to offer the best compromise between oversampling to resolve spots and avoiding photobleaching the sample. The pixel dwell time was 1 millisecond and the laser power used was 25  $\mu\text{W}$  unless otherwise stated. The acquired images were converted to 16-bit TIFF files using Acapella software to allow for further analysis using ImageJ.

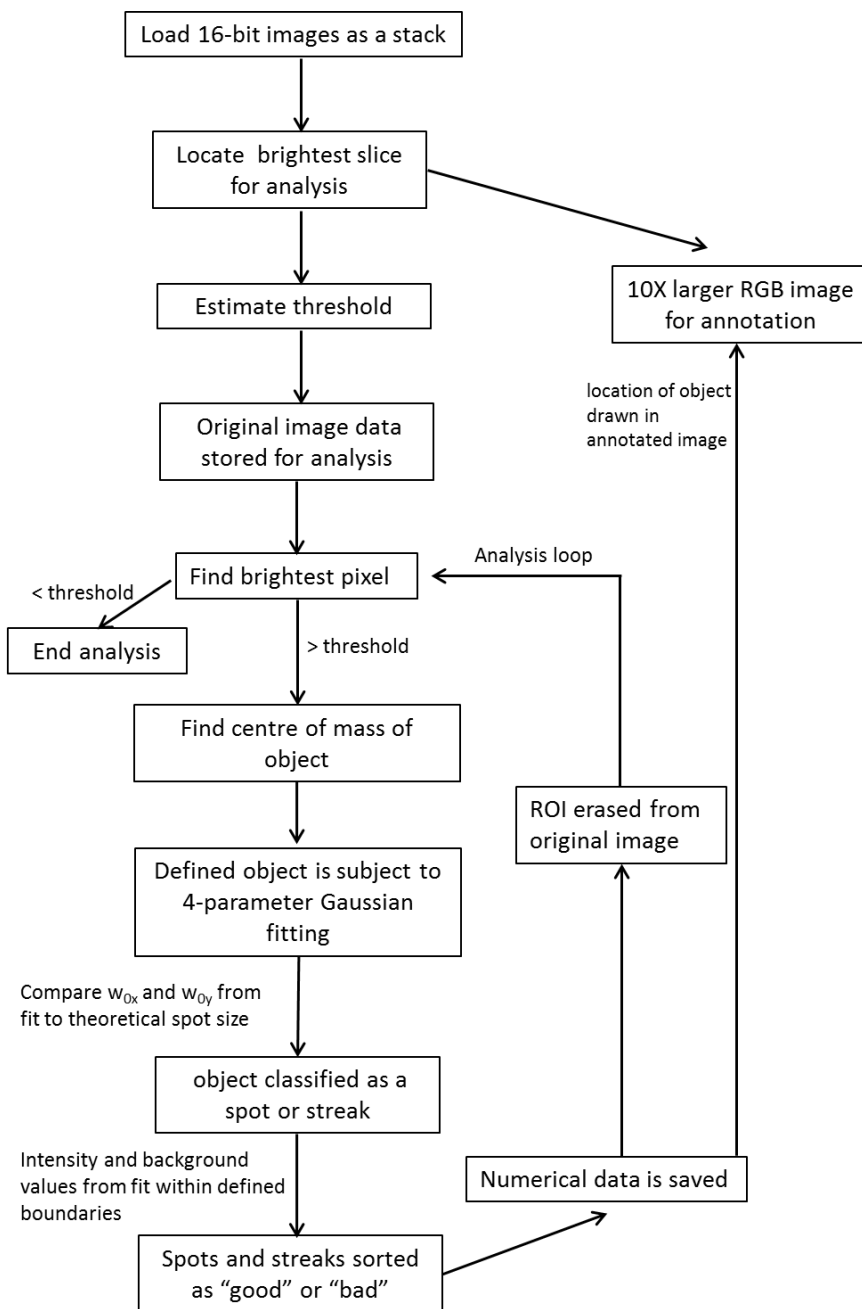
### 2.13. Automated Image Analysis

An ImageJ plugin was written for automated image analysis based on an analysis method by Henriques et al (2010) (Figure 4). Images were loaded into ImageJ as 16-bit TIFFs in a stack. The brightest image in the stack was identified as the plane of the membrane. Background noise was estimated for each image by finding the average value of the pixels with lowest intensity. A threshold for each image was calculated as the average pixel intensity plus 50% of the molecular brightness (CPP) of a protein monomer as measured in solution by FIDA. The pixel with highest intensity was selected and the position of the centre of mass for a defined area around that pixel was calculated. To determine if the object had a Gaussian-like intensity profile (expected for diffraction limited spot produced by a single molecule), 2D Gaussian fitting was performed in the region of interest (ROI):

$$I = I_{fit} e^{\frac{-2x^2}{w_x^2}} e^{\frac{-2y^2}{w_y^2}} + B_{fit}, \text{ varying the 4 following parameters:}$$

1. Maximum intensity,  $I_{fit}$  (peak of Gaussian):  $I_{fit} = (I_{max} - B) + \frac{i(I_{max}-B)}{2I_{range}}$ , (14)

where,  $I_{\max}$  is the intensity of the brightest pixel in the ROI;  $B$  = average pixel intensity + estimated noise in the image; and  $i$  was an integer varied in the range shown in Table 4.



**Figure 4: Outline of automated image analysis:** Main steps in image analysis program are shown in the flow chart with the primary decision criteria for classification and sorting of streaks and spots.

2. Background,  $B_{\text{fit}}$  (points where Gaussian falls towards 0):

$$B_{\text{fit}} = B_{\text{est}} + \frac{i(2I_{\text{avg}} - B_{\text{est}})}{B_{\text{range}}}, \quad (15)$$

where,  $i$  is an integer varied as described in Table 4,  $I_{\text{avg}}$  is the average pixel intensity in the image,  $B_{\text{est}}$  is the estimated background noise from pixels of low intensity in the image.

3. Size of object in x-dimension,  $w_x$  (full width at  $1/e^2$  max in x direction):

$$w_x = w_{\text{user}} + \frac{i(w_{\text{user}})}{2w_{\text{range}}}, \quad (16)$$

where,  $i$  is an integer varied as described in Table 4;  $w_{\text{user}}$  is the theoretical Airy disc radius at the wavelength used.

4. Size of object in y-dimension,  $w_y$  (full width at  $1/e^2$  max in y direction):

$$w_y = \frac{p}{2} + \frac{i(2w_{\text{user}} - p)}{z_{\text{range}}}, \quad (17)$$

where,  $i$  is an integer varied as described in Table 4;  $w_{\text{user}}$  is the theoretical Airy disc radius at the wavelength used;  $p$  is the pixel size in nm.

**Table 4: Parameter range for Gaussian fitting.**

	Min $i$	Max $i$	Min value	Max value	Increment size
$I_{\text{fit}}$	-5	5	$0.5(I_{\text{max}} - B)$	$1.5(I_{\text{max}} - B)$	$0.1(I_{\text{max}} - B)$
$B_{\text{fit}}$	0	30	$B_{\text{est}}$	$2I_{\text{avg}}$	$(2I_{\text{avg}} - B_{\text{est}})/30$
$w_x$	-5	10	Blue laser–120 nm Red laser–140 nm	Blue laser–480 nm Red laser–560 nm	Blue laser–24 nm Red laser–28 nm
$w_y$	0	20	Blue laser–50 nm Red laser–50 nm	Blue laser–380 nm Red laser–460 nm	Blue laser–16.5 nm Red laser–20.5 nm

A chi-square value was calculated for every parameter combination:

$$X^2 = \frac{\sum_{x,y} (I_{(x,y)} - B_{fit} - I_{fit} e^{-2((x-m)(p/w_x))^2} e^{-2((y-n)(p/w_y))^2})^2}{(\text{Area of ROI})(I_{max})}$$

where, I is the intensity at pixel (x, y) in the ROI;  $I_{fit}$  is calculated from Eq. 14;  $B_{fit}$  is from Eq. 15;  $w_x$  is from Eq. 16;  $w_y$  is from Eq. 17; m is the ROI centre of mass in the x direction; n is the ROI centre of mass in the y direction; p is the pixel size in nm.

$I_{fit}$ ,  $B_{fit}$ ,  $w_x$  and  $w_y$  were varied within the boundaries outlined in Table 4 to get the lowest chi square value. Following Gaussian fitting, the object was classified as a (diffraction limited) immobile spot or mobile streak based on the fit-obtained values for  $w_x$  and  $w_y$ . If the values for  $w_x$  and  $w_y$  were both between  $1/2$  and  $1 1/2$  of the theoretical Airy disc radius, the object was deemed to be a spot. If  $w_x$  or  $w_y$  fell outside the defined range for spot size, the object was deemed a streak. Further, spots and streaks were sorted as “good” or “bad” Gaussian objects. An object was “good” if  $I_{fit}$  and  $B_{fit}$  fell within (but did not equal) the boundary values for those parameters (Table 4). All objects deemed “good” were included in subsequent data analysis, while “bad” objects were discarded. Object intensity, position, values obtained from Gaussian fitting, and the parameters used for analysis were output as a text file and annotated images showing the location of detected objects. The full analysis script with annotations is in the Appendix.

#### *2.14 Object intensity distribution (complex size distribution) analysis*

Objects detected in automated image analysis were grouped into 2 categories: mobile streaks and immobile spots at the membrane. The intensity data was normalized by dividing the fit-obtained intensity value ( $I_{fit}$ ) by the molecular brightness of a

monomeric protein measured in solution by FIDA, CPP. The data was binned and plotted as % occurrence as a function of normalized intensity (i.e. oligomer size). To describe the normalized intensity distribution of objects in confocal images, we assumed a Gaussian confocal volume where the pixel intensity for a particle with molecular brightness (CPP),  $I_{CPP}$ , placed at position  $(x, y, z)$  with respect to the centre of the confocal volume is on average:

$$\langle i(x, y, z) \rangle = I_{CPP} e^{-\frac{2x^2}{w_0^2}} e^{-\frac{2y^2}{w_0^2}} e^{-\frac{2z^2}{z_0^2}}$$

Also, we assumed that the confocal scanning velocity along the Y-axis,  $v$ , is high enough that particles have mainly linear trajectories with respect to the confocal volume (this condition is fulfilled if the diffusion coefficient of the particles,  $D$ , is less than  $vw_0/4$ , that is  $\sim 15\mu\text{m}^2/\text{s}$  in the conditions of the experiment). Considering this, the average maximum intensity achieved by a particle depends solely on its  $(x, z)$  coordinates:

$$\langle i_{\max}(x, y) \rangle = I_{CPP} e^{-\frac{2x^2}{w_0^2}} e^{-\frac{2z^2}{z_0^2}}$$

Finally, we assumed that particles remain at a well-defined position during pixel acquisition, that is  $D \ll 100\mu\text{m}^2/\text{s}$ . This is true when protein is membrane bound, but not in solution.

#### *2.14.1 Expected probability distribution of mobile streaks at the membrane for a single and multiple fluorescent species*

At the membrane diffusion takes place in the X, Y plane and is constrained to 2D diffusion, compared to 3D diffusion in solution. For a homogenous particle distribution in the X, Y plane, the probability of obtaining a maximum intensity comprised between  $i$

and  $i+di$  is proportional to the length  $dL$  along the x-axis for which a particle will achieve maximum intensity:

$$p_{2D}(\langle i_{\max}^p \rangle) d\langle i_{\max}^p \rangle = \frac{dx(\langle i_{\max}^p \rangle)}{x_0}$$

where  $x_0 = w_0 \sqrt{2 \ln(I_{CPP}/t_D)}$  is the linear cross-section over which particles are detected if the detection threshold is  $t_D$  and where

$$|dx(\langle i_{\max}^p \rangle)| = w_0 \left[ 2 \ln(I_{CPP} / \langle i_{\max}^p \rangle) \right]^{-\frac{1}{2}} \langle i_{\max}^p \rangle^{-1} d\langle i_{\max}^p \rangle$$

in the end:

$$p_{2D}(\langle i_{\max} \rangle) = \left[ 2 \ln\left(\frac{I_{CPP}}{t_D}\right) \right]^{-\frac{1}{2}} \left[ 2 \ln\left(\frac{I_{CPP}}{\langle i_{\max} \rangle}\right) \right]^{-\frac{1}{2}} \langle i_{\max} \rangle^{-1}$$

Because of photon noise, however, actual detected maximum intensities are distributed around their average value, and the distribution can be approximated as:

$$p_{2D}(i_{\max}) = \frac{1}{\sigma \sqrt{2\pi}} \int_{t_D}^{I_{CPP}} \bar{p}_{2D}(\langle i_{\max} \rangle) e^{-\frac{(i_{\max} - \langle i_{\max} \rangle)^2}{2\sigma^2}} d\langle i_{\max} \rangle ,$$

where  $\sigma$  is the width of the distribution due to photon noise. For the case where more than one fluorescent species is present because of oligomer formation (such that we have fluorescent species with brightness of  $I_{CPP}$ ,  $2I_{CPP}$ ,  $3I_{CPP}$ , etc) we considered a simple oligomer formation process, where the same dissociation constant ( $K$ ) is associated with oligomers with different sizes. In this case:

$$p_{2D}(i_{\max}) = \sum_{n=1}^{\infty} f_n \frac{1}{\sigma \sqrt{2\pi}} \int_{t_D}^{nI_{CPP}} \left[ 2 \ln\left(\frac{I_{CPP}}{t_D}\right) \right]^{-\frac{1}{2}} \left[ 2 \ln\left(\frac{I_{CPP}}{i_{\max}}\right) \right]^{-\frac{1}{2}} \langle i_{\max} \rangle^{-1} e^{-\frac{(i_{\max} - \langle i_{\max} \rangle)^2}{2\sigma^2}} d\langle i_{\max} \rangle$$



$$= \sum_{n=1}^{\infty} \frac{\bar{n}^n e^{-\bar{n}}}{(1 - e^{-\bar{n}})} \frac{1}{\sigma \sqrt{2\pi}} \int_{t_D}^{I_{CPP}} \left[ 2 \ln \left( \frac{I_{CPP}}{t_D} \right) \right]^{-\frac{1}{2}} \left[ 2 \ln \left( \frac{I_{CPP}}{i_{max}} \right) \right]^{-\frac{1}{2}} \langle i_{max} \rangle^{-1} e^{-\frac{(i_{max} - \langle i_{max} \rangle)^2}{2\sigma^2}} d\langle i_{max} \rangle$$

where  $f_n$  is the probability to encounter an oligomer of size  $n$ :

$$f_n = \left( \sqrt{K_D/c_0 + \frac{(K_D/c_0)^2}{4}} - \frac{K_D/c_0}{2} \right) \left( 1 + \frac{K_D/c_0}{2} - \sqrt{K_D/c_0 + \frac{(K_D/c_0)^2}{4}} \right)^{n-1} \quad (18)$$

In the above equation,  $c_0$ , is the total protein concentration. We also considered the case

where the formation of the dimer associated with the difference dissociation constant ( $K_1$ )

than the formation of higher order oligomers ( $K_2$ ). In this case we have:

$$f_1 = \frac{K_1/c_0 + K_1 K_2/c_0^2 - \sqrt{K_1/c_0} \sqrt{K_1/c_0 - 2 K_1 K_2/c_0^2 + 4 K_2^2/c_0^2 + K_1 K_2^2/c_0^3}}{2(K_1/c_0 - K_2/c_0)}$$

And for  $n > 1$ :

$$f_n = \frac{f_1^n}{(K_1/c_0)(K_2/c_0)^{n-2}} \quad (19)$$

To relate the probability distributions calculated above to the binned data plotted as a %

occurrence, one has to multiple the probability distribution,  $p_{2D}$ , by  $100 \cdot b$ , where  $b$  is the

bin size.

#### 2.14.2 Expected probability distribution of immobile spots at the membrane

Since immobile particles appear as diffraction limit spots, their maximum intensity,  $\langle i_{max} \rangle$ , can be determined from Gaussian fitting. However, photon noise must

be considered and will result in the broadening of the intensity distribution. For a single type of particle, the expected distribution is then:

$$p_{1D}(i_{\max}) = \frac{1}{\sigma\sqrt{2\pi}} e^{-\frac{(i_{\max} - I_{\text{CPP}})^2}{\sigma^2}}$$

This distribution, due to photon noise, is Poisson, but can be approximated by a normal distribution with high signal and background. For a collection of particles with specific brightness  $I_{\text{CPP}}$ ,  $2 I_{\text{CPP}}$ , up to  $N I_{\text{CPP}}$  the expected distribution becomes:

$$\bar{p}_{1D}(i_{\max}) = \frac{1}{\sigma\sqrt{2\pi}} \sum_{n=1}^N f_n e^{-\frac{(i_{\max} - nI_{\text{CPP}})^2}{\sigma^2}} \quad (20)$$

where  $f_n$  is the probability to encounter an oligomer of size  $n$ . Assuming that photon noise is mainly due to background noise, the standard deviation,  $\sigma$ , is the same for all sizes of oligomers.

### 2.15 Determining concentration of protein from images

The concentration of protein can be quantified by combining intensity data from confocal images and the molecular brightness measured by FIDA. Concentration of protein,  $c_0$ , at the membrane was calculated as:

$$c_M = \frac{I_{\text{avg}} - \langle B_{\text{fit}} \rangle}{I_{\text{CPP}}}, \quad (21)$$

where  $I_{\text{avg}}$ , is the average pixel intensity in the image,  $\langle B_{\text{fit}} \rangle$  is the average fit obtained value for background from all detected objects with a good Gaussian fit, and  $I_{\text{CPP}}$  is the molecular brightness of monomeric protein measured by FIDA in solution. For protein in solution, the concentration was calculated as:

$$c_S = \frac{I_{avg} - B_{est}}{I_{CPP}}, \quad (22)$$

where  $B_{est}$  is the estimated level of background signal of the buffer alone measured by FIDA.  $B_{est}$  has a value of 0.3 kHz and for the red channel and a value of 0.9 kHz for the blue channel.

### 2.16 Binding constants for protein binding to planar bilayers

Binding to SLBs was assessed by the same model as for Bax binding to liposomes assuming a partition between soluble and membrane bound protein (Ben-Tel et al, 1996).

From Eq. 9, the associated equilibrium constant can be expressed as:

$$K_D = \frac{P_{free}L}{P_{bound}} = \frac{c_S L}{c_M} = \frac{2c_S}{Ac_M},$$

where  $c_S$  and  $c_M$  are the concentrations of protein in solution and at the membrane, respectively. In the equation above, the lipid concentration,  $L$ , in the planar bilayer can be expressed as  $2/A$ , where  $A=0.75\text{nm}^2$  is the surface area of a single lipid.

To relate these quantities to the measured fluorescence intensities we first calculate the expected intensity measured in solution (after background subtraction):

$$\langle I_S \rangle = \iiint c_S I_{CPP} e^{-2x^2/w_0^2} e^{-2y^2/w_0^2} e^{-2z^2/z_0^2} dx dy dz = c_S I_{CPP} \left(\frac{\pi}{2}\right)^{\frac{3}{2}} w_0^2 z_0$$

Then we calculate the expected intensity measured at the membrane (after background subtraction):

$$\langle I_M \rangle = \frac{\langle I_S \rangle}{2} + \iint c_M I_{CPP} e^{-2x^2/w_0^2} e^{-2y^2/w_0^2} dx dy = \frac{\langle I_S \rangle}{2} + c_M I_{CPP} \frac{\pi}{2} w_0^2$$

Therefore:

$$s = \frac{\langle I_M \rangle}{\langle I_S \rangle} = \frac{1}{2} + \sqrt{\frac{2}{\pi}} \frac{c_M}{c_S} \frac{1}{z_0} = \frac{1}{2} + \sqrt{\frac{2}{\pi}} \frac{2}{AK_D} \frac{1}{z_0}$$

Since at equilibrium,  $s$  is a constant, we expect  $\langle I_M \rangle$  to vary linearly with  $\langle I_S \rangle$ , and the slope to be  $s$ . The  $K_D$  can then be easily calculated from the slope:

$$K_D = \frac{2\sqrt{2}}{s \sqrt{\pi A z_0}}$$

In the above expression,  $K_D$  is in units of  $\text{nm}^{-3}$ , given  $A$  and  $z_0$  are expressed in nm. To express it in  $\mu\text{M}$  instead and assuming  $z_0 \sim 2\mu\text{m}$  we write:

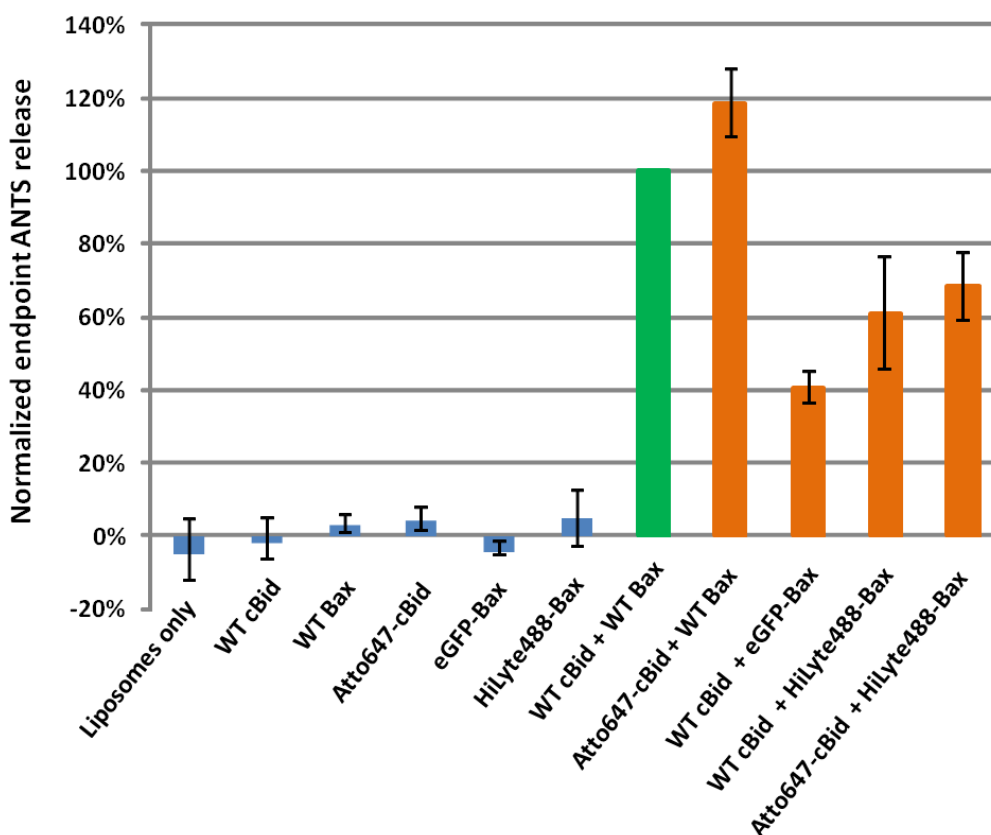
$$K_D = \frac{2\sqrt{2}}{s \sqrt{\pi A z_0}} \frac{10^7}{6.02} = \frac{1767 \mu\text{M}}{s} = \frac{1767 \mu\text{M}}{c_M/c_S} \quad (23)$$

where  $c_M$  and  $c_S$  are the concentrations of protein at the membrane and solution calculated from Eqs. 21 and 22, respectively.

### 3 Characterization of Bax binding to liposomes

#### 3.1 Protein labelling and pore forming activity

WT cBid and WT Bax, when incubated together with liposomes, resulted in 70-80% ANTS release after 2 hours calculated by Eq. 1. This amount of ANTS release was normalized to 100% as a positive control to assess the relative activity of fluorescent protein constructs (Figure 5). In the ANTS assay, eGFP-Bax used for experiments of Bax binding to liposomes, displayed approximately 40% of the pore forming activity of WT Bax.



**Figure 5: Pore forming activity of fluorescent proteins.** Fluorescent proteins were assayed by ANTS release assay to determine if they retained activity after mutation and labelling with fluorescent dyes. Endpoint values after 2 hours calculated by Eq. 1 were corrected for bleed through and normalized to triton release within a given experiment. Above, data were normalized to WT cBid + WT Bax considered as having 100% activity. Blue bars are negative controls lacking one or both cBid and Bax. The green bar is the positive control using WT cBid and Bax. Orange bars show the activity of fluorescent protein constructs. Error bars indicate standard deviation (N=3).

**Table 5. Summary of protein labelling conditions**

Trial	Dye / MW (Da) / charge*	Single construct/ plasmid #	Labelling conditions					Labelling efficiency	
			Standard**	TCEP	Overnight at 4°C	4M Urea	4-6 hour reaction (room temp)		pH 7.5
BID									
1	Atto647N / 868 / positive	126C/# 2118	X						70%
BAX									
2	DAC / 298 / neutral	126C/ #1731	X						83%
3	Alexa 488 / 720 / negative	126C/ #1731	X						36%
4			X	X					42%
5		3C/ #1997	X						42%
6			X	X					52%
7				X	X				27%
8	Atto 488 / 1067 / positive	126C/ #1731	X						42%
9					X				16%
10			X			X			6%
11					X	X			13%
12								X	
13	Atto 495 / 574 / positive	126C/ #1731	X						8%
14			X						12%
15		47C/ #2035	X						39%
16					X				25%
17					X	X			32%
18	HiLyte 488 / 567 / neutral	3C/ #1997	X						48%
19		47C/ #2035	X						65%
20		47C/ #2035		X			X	X	81%
21		WT/ #1572		X			X	X	155%
22		Cys-/ #1730		X			X	X	11%

\*Charge at pH 7.0 - 7.5

\*\*standard labelling conditions: 2 hour reaction at room temperature; 20X molar excess dye, 0.5% CHAPS and pH ~7.0 was used in all reactions except when indicated otherwise

For use in single molecule experiments, purified Bid and Bax single cysteine mutants were labelled using thiol reactive dyes. Labelled Bid was obtained with good yield and high labelling efficiency (Table 5, trial 1) using standard labelling conditions as per the manufacturer's instructions. Following labelling, the Atto647-Bid was cleaved with caspase-8 and Atto647-cBid was obtained. Atto-labelled cBid appears to have slightly higher activity than wild-type cBid and causes an endpoint release that is higher than the positive control (Figure 5). Alone, neither WT cBid nor Atto647-cBid is able to permeabilize MOM-like liposomes in the ANTS release assay.

Labelling Bax single cysteine mutants with a high degree of labelling required for single molecule experiments proved difficult. Although single cysteine sites that have previously been shown to be accessible to solvent (Annis et al., 2004) were chosen to improve the chance of labelling, under standard conditions, bright, photostable dyes (Alexa and Atto series) did not label with efficiency over 50% in the various Bax mutants tried (Table 5, trials 3-17). Optimization of the standard conditions was required to increase the amount of labelled protein obtained. In general, smaller dyes (low MW) with neutral charge allowed for better labelling. A parallel labelling experiment (Table 5, trial 2 and 14) demonstrated that under identical conditions, the small, neutral dye DAC labelled the protein with 82% efficiency compared to the larger, positively charged dye Atto495 which resulted in 12% labelling. A small, neutral charged, photostable dye was identified in the HiLyte series. Using HiLyte 488 and conditions to favor the reaction of thiol and maleimide groups on the protein and dye respectively, Bax was obtained with an adequate degree of labelling (Table 5, trial 20). To increase the labelling efficiency, the

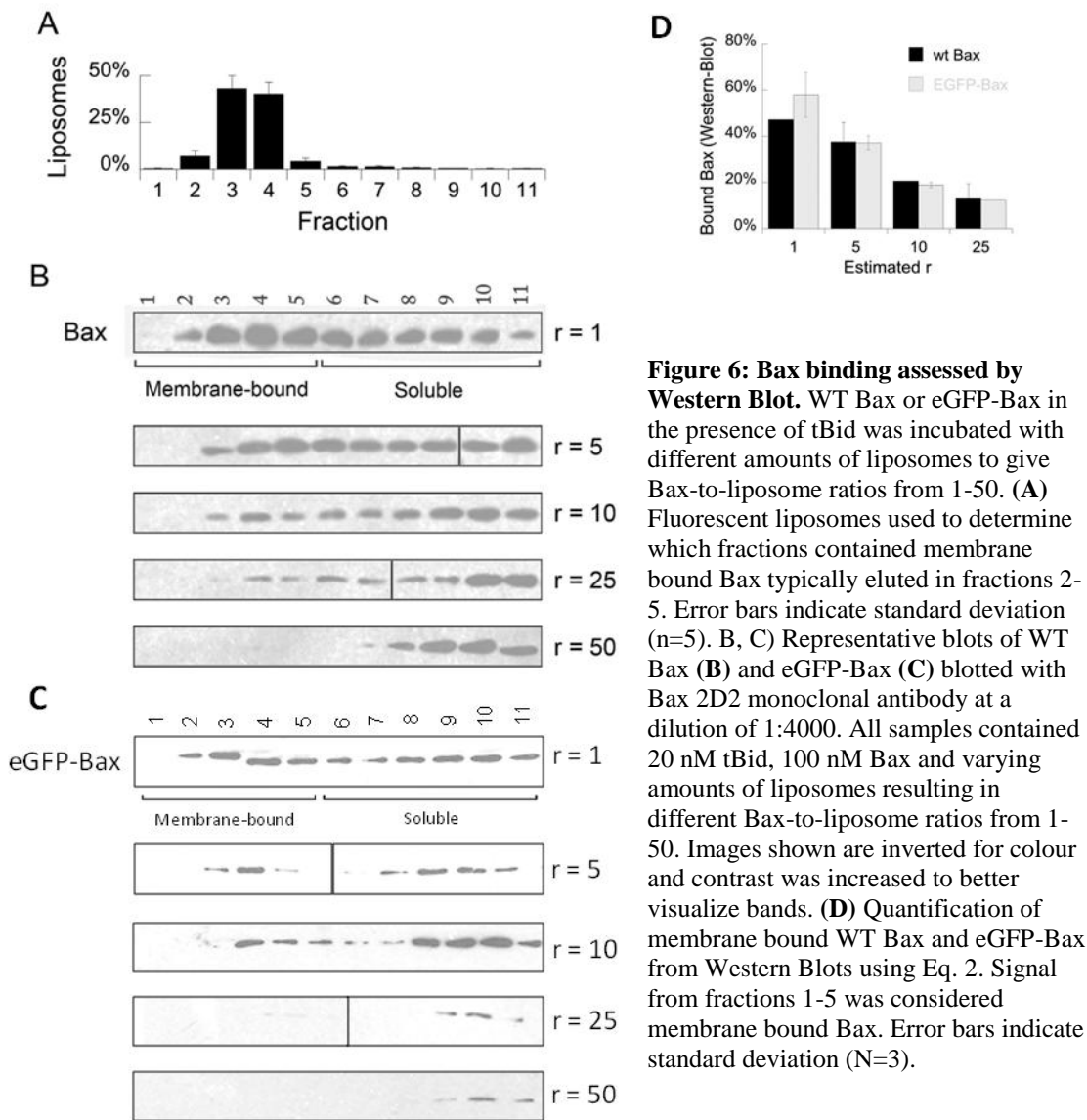
reaction was carried out at pH 7.5 to promote reduction of the thiol group and the labelling reaction was allowed to proceed for 2-4 hours longer than standard conditions. These optimizations allowed for approximately 80% labelling efficiency of Bax 47C. To ensure that these stringent labelling conditions did not result in non-specific labelling of the protein, control labelling reactions were performed using a cysteine-less mutant and the wild-type Bax protein which contained two endogenous cysteines (Table 5, trials 20-22). As expected, labelling the wild-type protein resulted in a labelling efficiency higher than 100% while the cysteine-less mutant showed a low amount of non-specific labelling of approximately 11%.

Labelled Bax protein retained pore forming activity in the ANTS release assay, though to a lesser extent compared to the wild-type protein (Figure 5). HiLyte488-Bax showed approximately 61% of the intrinsic pore forming activity of wild-type Bax in the presence of cBid. Although this is not ideal, the dye labelled Bax showed higher pore forming activity than eGFP-Bax. Thus, HiLyte488-Bax was preferred to eGFP-Bax for subsequent experiments. Negative controls (blue in Figure 5) lacking one or both cBid and Bax did not show any significant ANTS release as expected.

### *3.2 Bax binding to liposomes by Western blot*

Western blotting was performed to assess WT Bax and eGFP-Bax binding to liposomes at different Bax-to-liposome ratios (Figure 6). 100 nM Bax activated by 20 nM tBid was incubated with different amounts of liposomes to achieve a Bax-to-liposome ratio,  $r$ , between 1-50 estimated from the total amounts of protein and lipid used to prepare samples. Following incubation, membrane-bound protein was separated from





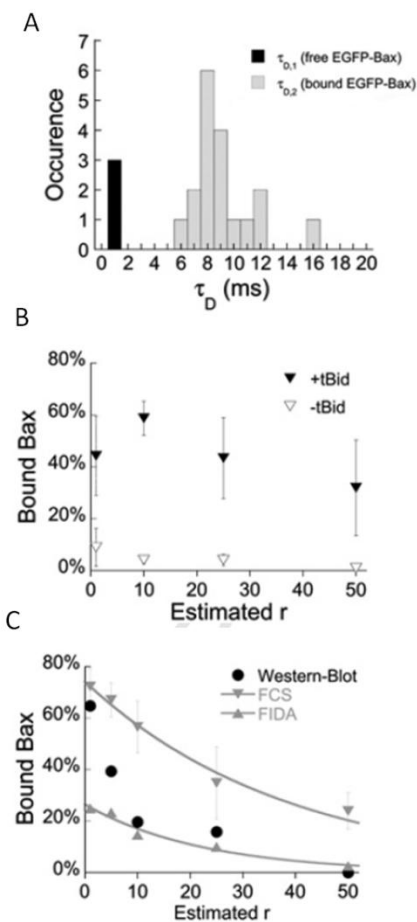
**Figure 6: Bax binding assessed by Western Blot.** WT Bax or eGFP-Bax in the presence of tBid was incubated with different amounts of liposomes to give Bax-to-liposome ratios from 1-50. **(A)** Fluorescent liposomes used to determine which fractions contained membrane bound Bax typically eluted in fractions 2-5. Error bars indicate standard deviation (n=5). **(B, C)** Representative blots of WT Bax **(B)** and eGFP-Bax **(C)** blotted with Bax 2D2 monoclonal antibody at a dilution of 1:4000. All samples contained 20 nM tBid, 100 nM Bax and varying amounts of liposomes resulting in different Bax-to-liposome ratios from 1-50. Images shown are inverted for colour and contrast was increased to better visualize bands. **(D)** Quantification of membrane bound WT Bax and eGFP-Bax from Western Blots using Eq. 2. Signal from fractions 1-5 was considered membrane bound Bax. Error bars indicate standard deviation (N=3).

unbound soluble protein by gel filtration and detected by Western Blot. DiD labelled liposomes were used to identify liposome containing fractions which always eluted in fractions 2 to 5 (Figure 6A). Membrane bound Bax is also present in these fractions. Free Bax proteins in solution eluted, in absence of liposomes, in fraction 6 and higher. Representative blots show the targeting of WT Bax and eGFP-Bax to liposomes (Figure 6B and 6C respectively). The Bax elution profile contrasts that of tBid in immunoblotting

experiments which showed that at all protein-to-liposome ratios, 90% of tBid was associated with the membrane (data not shown) whereas Bax showed saturation of binding at higher  $r$  values (Figure 6D). At low Bax-to-liposome ratios the majority of Bax is membrane bound and elutes with liposomes in fractions 2 to 5. As  $r$  increased, increasing amounts of unbound Bax appeared in fractions 6 and higher. This phenomenon was observed at low (Figure 6) and high protein (Satsoura et al 2012, Table 1) concentrations. Saturation of membrane binding at high Bax-to-liposome ratios was true for both WT Bax and the eGFP fusion protein. In the absence of Bid, less than 10% of Bax was membrane bound at  $r=1$  (data not shown). The membrane binding behaviour of WT and eGFP-Bax was almost indistinguishable when Western blots were quantified (Figure 6D). It appears that Bax and eGFP-Bax both bind to liposomes with similar affinity at a given Bax-to-liposome ratio.

### *3.3 Bax binding to liposomes by fluorescence techniques*

To compliment Western Blot experiments, the amount of Bax bound to liposomes was also assayed by fluorescence fluctuation measurements prior to, and following gel filtration. From FCS, a clear difference in the diffusion time of soluble and membrane bound eGFP-Bax was observed as expected (Figure 7A). The amount of Bax bound to liposomes in the absence of tBid assessed by FCS was found to always be less than 10% for all Bax-to-liposome ratios (Figure 7B). This was a robust observation also reflected in the Western blot data suggesting that Bax does not bind liposomal membranes in the



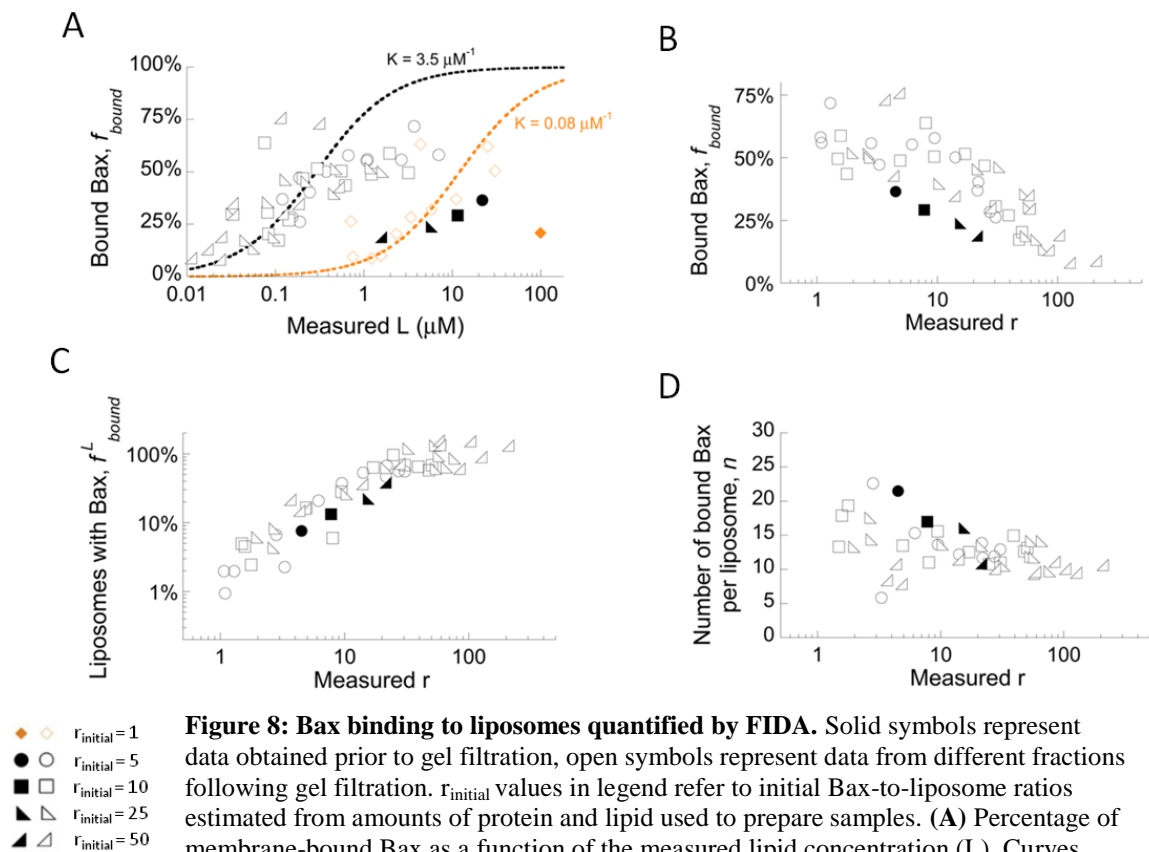
**Figure 7: eGFP-Bax binding to liposomes by fluorescence techniques.** 100 nM eGFP-Bax and 20 nM tBid (when present) were incubated with varying amounts of liposomes giving Bax-to-liposomes ratios between 1-50. The estimated ratios were determined from the initial amounts of protein and lipid used to prepare samples. **(A)** Distribution of diffusion times calculated from Eq. 3c for eGFP-Bax when incubated with liposomes in the presence of tBid in one representative experiment. **(B)** Bax binding to liposomes in the presence and absence of tBid measured by FCS in one representative experiment. Error bars indicate standard deviation (n=10). **(C)** Percentage of Bax bound at different Bax-to-liposome ratios determined by Western Blot, FCS and FIDA. Percent of Bax bound by FCS was obtained from Eq. 6, and the amount of Bax bound by FIDA was calculated using Eq. 7. One representative series of measurements is shown. Error bars indicate standard deviation (n=10).

absence of tBid as reported previously (Lovell et al, 2008;). The 3 methods of measuring the amount of Bax bound to liposomes were directly compared in a single experiment (Figure 7C). Although saturation of membrane binding at high Bax-to-liposome ratios was a robust feature observed across all experiments, the fraction of bound Bax at a given r varied for each method. In general, the FCS method resulted in higher amounts of Bax bound at a given r, while FIDA showed lower amounts of Bax binding. The Western blot data showed intermediate amounts of binding compared to the fluorescence techniques. As expected, at low Bax-to-liposome conditions, the Western blot and FCS data show a

similar amount of bound Bax, while at high Bax-to-liposome conditions, the Western blot is in accordance with FIDA data.

### *3.4 Bax binding can be described by a simple binding equilibrium*

To accurately determine the exact Bax-to-liposome ratio, fluorescent liposomes (labelled with DiD) were used in experiments with eGFP Bax. This allowed for measuring the precise Bax and liposome concentrations in samples and calculating a measured Bax-to-liposome ratio (measured  $r$ ), opposed to the estimated  $r$  based on sample preparation conditions. It was found that the measured  $r$  was often higher than the estimated  $r$ , although the relative increments in lipid concentration between samples remained constant. The discrepancy in  $r$  values was likely due to a lipid concentration that was lower than expected owing to the loss of lipid during the resuspension and extrusion steps in liposome preparation. As a result, there was significant variation between experiments in the amount of Bax bound at a given estimated  $r$ . To overcome this, the actual lipid and protein concentrations were measured for all samples prior to and following gel filtration in order to calculate a measured  $r$  value and gauge the real dependence of the amount of bound Bax on  $r$ . The measured  $r$  values using 50 nm liposomes, were found to range from  $r \sim 1$  to  $r \sim 100$ . FIDA was used to calculate the amount of membrane bound Bax in samples prior to and following gel filtration (Figure 8A-B) as well as the percent of liposomes carrying a Bax (Figure 8C) and the number of Bax molecules per liposome (8D). Samples that had an initial (estimated)  $r \geq 5$  (at a constant Bax-to-Bid ratio of 5, in which case the Bid-to-liposome ratio is  $>1$ ) showed the



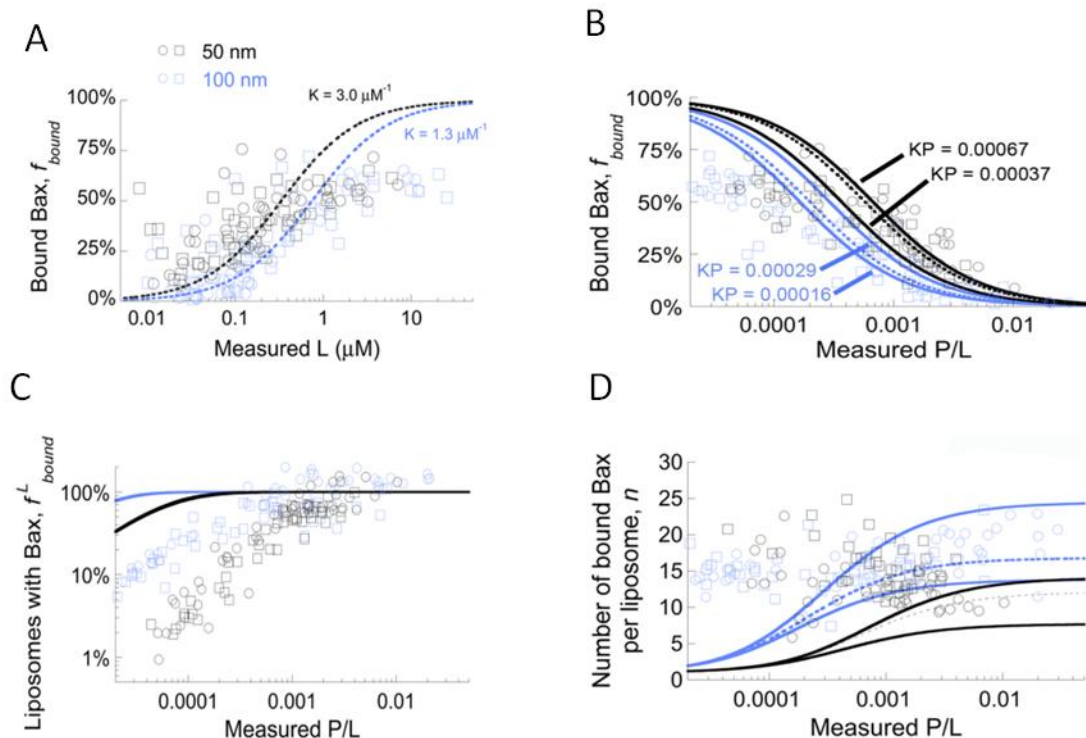
**Figure 8: Bax binding to liposomes quantified by FIDA.** Solid symbols represent data obtained prior to gel filtration, open symbols represent data from different fractions following gel filtration.  $r_{\text{initial}}$  values in legend refer to initial Bax-to-liposome ratios estimated from amounts of protein and lipid used to prepare samples. (A) Percentage of membrane-bound Bax as a function of the measured lipid concentration (L). Curves were fitted with Eq. 10 for low  $r_{\text{initial}} < 5$  (orange curve) and high  $r_{\text{initial}} > 5$  (black curve). (B) Percentage of membrane bound Bax as a function of measured Bax-to-liposome ratio,  $r$ . (C) Number of liposomes with at least one Bax bound as a function of  $r$ . (D) Average number of Bax bound per liposome as a function of  $r$ .

amount of membrane bound Bax was solely dependent on the total lipid concentration, L (Figure 8A). The data agrees with a simple partition equilibrium (Eq. 10) considering that the bound Bax fraction measured by FIDA is only accurate at high  $r$  (i.e. low lipid concentration), resulting in an apparent Bax binding constant of  $3.5 \pm 0.4 \mu\text{M}^{-1}$  ( $K_D = 0.286 \mu\text{M}$ ) (Figure 8A, black curve). At low initial  $r$  ( $< 1$  Bid per liposome), data still follows the simple partition equilibrium, but with a lower binding constant of  $0.08 \pm 0.02 \mu\text{M}^{-1}$  ( $K_D = 12.5 \mu\text{M}$ ) (Figure 8A, orange curve). The measured Bax-to-liposome ratio, was also

a good predictor of the amount of membrane bound Bax (Figure 8B), the number of liposomes with bound Bax (Figure 8C) and the average number of Bax molecules bound per liposome (Figure 8D). The amount of bound Bax decreases with increasing  $r$ , while the amount of liposomes carrying Bax increases reflecting what was observed in the Western Blot data. Strangely, the data obtained before gel filtration (filled data points) shows lower Bax binding and fewer liposomes carrying Bax, but with more Bax molecules per liposome compared to data obtained after gel filtration (open data points). A possible reason is that some eGFP-Bax becomes trapped on the column and also samples were incubated for 2 hours prior to gel filtration while samples after gel filtration were incubated for longer periods due to the difficulty in measuring many fractions quickly.

### *3.5 Bax binding to different size liposomes*

The effect of liposome size on Bax binding was assayed by comparing Bax binding to 50 nm and 100 nm diameter liposomes. Liposomes larger than 100 nm diameter were not used for FIDA experiments as they may not behave as point objects. Bax binding was quantified assuming a simple partition equilibrium between solution and the membrane (Eq. 10). At the same measured lipid concentration,  $L$ , a higher fraction of Bax binds to 50 nm liposomes than to 100 nm liposomes reflected in apparent binding coefficients of  $3.0 \pm 0.4 \mu\text{M}^{-1}$  for 50 nm liposomes and  $1.3 \pm 0.2 \mu\text{M}^{-1}$  for 100 nm liposomes (Figure 9A). Similarly at a given Bax-to-lipid ratio,  $P/L$ , the data shows higher binding to 50 nm liposomes (Figure 9B) when the data is fit with Eq. 10. The dashed curves represent data fitted with  $P/L > 0.005$  for 50 nm liposomes and  $P/L > 0.0012$  for 100 nm



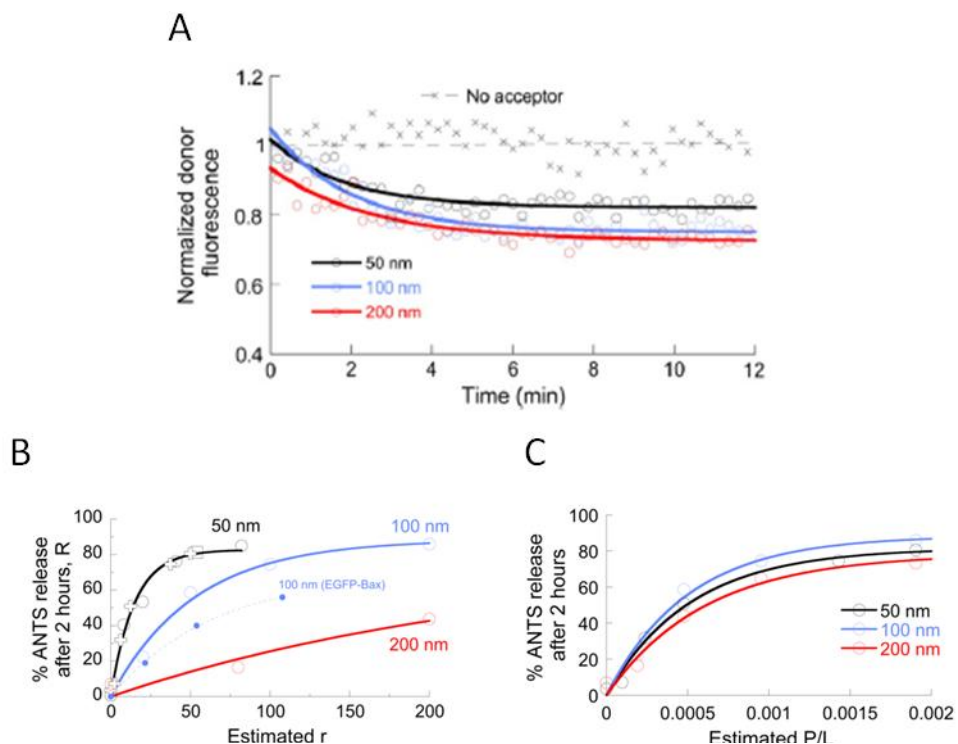
**Figure 9: FIDA of Bax binding to different sized liposomes.** Black symbols are data for 50 nm vesicles, blue symbols are data for 100 nm vesicles; circles and squares represent two different repeats of the experiment for all samples irrespective of  $r_{\text{initial}}$ . **(A)** Percent of bound Bax as a function of lipid concentration for fractions collected following gel filtration. Only data where measured  $r > 10$  is plotted since this is the range in which FIDA is accurate. **(B)** Percentage of membrane-bound Bax as a function of the protein-to-lipid ratio (P/L). Dashed lines represent fitted data with  $P/L > 0.005$  for 50 nm liposomes and  $P/L > 0.0012$  for 100 nm liposomes. Solid lines show data fit where  $0.002 \text{ nM} < P < 0.01 \text{ nM}$  and  $0.2 \text{ nM} < P < 1 \text{ nM}$ . In (A, B) lines represent fits to the data using Eq. 10. **(C)** Percentage of liposomes with Bax bound as a function of P/L. **(D)** Number of bound Bax per liposome as a function of P/L. In (C) and (D), lines show expected values according to Eqs. 11 and 12 respectively, using KP values from 11B.

liposomes reflecting the range in which FIDA is accurate. Since the amount of bound Bax is also dependant on Bax concentration, P, subsets of data where  $0.002 \text{ nM} < P < 0.01 \text{ nM}$  (low protein concentration) and  $0.2 \text{ nM} < P < 1 \text{ nM}$  (high protein concentration) were fit with Eq. 10 indicated by solid curves (Figure 9B). This returned separate KP values for 50 and 100 nm liposomes at low and high Bax concentrations. Subsequent coefficient values for K using the average P value for each subset were calculated as being  $K = 2.4 - 6.3 \cdot 10^6 \text{ M}^{-1}$  for Bax binding to 50 nm liposomes and  $0.8 - 2.9 \cdot 10^6 \text{ M}^{-1}$  for binding to 100 nm

liposomes. The K values obtained were always higher for smaller liposomes. Using the K values from Figure 11B, the number of liposomes with Bax (Figure 9C) and the number of Bax bound per liposome (Figure 9D) were fit with Eqs. 11 and 12 respectively. The fits are in good accordance with the data at high P/L as expected for FIDA.

It has been reported that Bax is unable (or hindered) to oligomerize in liposomes smaller than 200 nm in diameter (Lucken-Ardjomande et al, 2008). To ensure that Bax oligomerization and membrane permeabilization occurs in the small liposomes used in this study, FRET and dye release assays were performed. First to investigate Bax oligomerization, Bax-Bax FRET was carried out using liposomes of 50, 100 and 200 nm diameter. Fluorescent liposomes were used to accurately quantify lipid concentration and ensure the same lipid concentration was present across all samples. In the presence of tBid and excess acceptor Bax, the fluorescence of donor Bax decreased over time for all liposome sizes (Figure 10A). In the absence of acceptor Bax (replaced with unlabelled WT Bax), the donor signal remained fairly constant indicating that Bax-Bax FRET (and oligomerization) occurred when acceptor Bax was present. The fluorescence decrease over time due to FRET occurred to a similar extent for all liposome sizes indicating Bax oligomerization is as efficient in 50 nm liposomes as it is in larger 200 nm liposomes. The ability of Bax to permeabilize liposomes of different size was assayed by ANTS release. ANTS release was higher for smaller liposomes at a given estimated  $r$  (Figure 10B), but similar for all size liposomes at a given measured P/L (Figure 10C). Compared to WT Bax, eGFP-Bax is able to permeabilize membranes but less efficiently (comparing the 100 nm data in Figure 10B).





**Figure 10: Bax membrane permeabilization activity.** (A) Bax-Bax FRET as a measure of Bax oligomerization in liposomes of different size at a constant estimated protein:lipid=0.0017. 20 nM DAC-Bax134C (donor) and 24 nM tBid were incubated with liposomes in the presence or absence of 100 nM NBD-Bax134C (acceptor). WT unlabelled Bax was substituted in the absence of acceptor. Lines are exponential fits to the data. (B) Percentage of ANTS release after 2 hours as a function of estimated Bax-to-liposome ratio ( $r$ ). Crosses represent data at low lipid concentration (0.04 g/L or 50  $\mu$ M) while squares represent data at high lipid concentration (7.3 g/L or 9.5 mM). Open circles represent data obtained in one experiment using DiD labelled liposomes to ensure relative Bax-to-liposome ratios were exact when using different size liposomes. eGFP-Bax ANTS release for 100 nm vesicles is shown for reference (C) Same data as (B) plotted as a function of measured Bax-to-lipid ratio (P/L).

## 4 Characterization of cBid and Bax binding to supported bilayers

### 4.1 Optimization of coverslip preparation

Mica substrate was glued onto a glass coverslip (#1.5, 170  $\mu\text{m}$  thickness) in order to be able to prepare supported lipid bilayers that could be observed by confocal microscopy. However, these mica containing samples showed a decreased total fluorescence signal and CPP when performing FIDA measurements on solutions of Alexa 488 compared to samples that were observed through a standard glass coverslip only (Table 6). This was unsatisfactory, since a low CPP entails that single molecule experiments will not be possible, and since it is essential to accurately measure the CPP in order to determine the oligomeric state of protein from the measured fluorescence intensity.

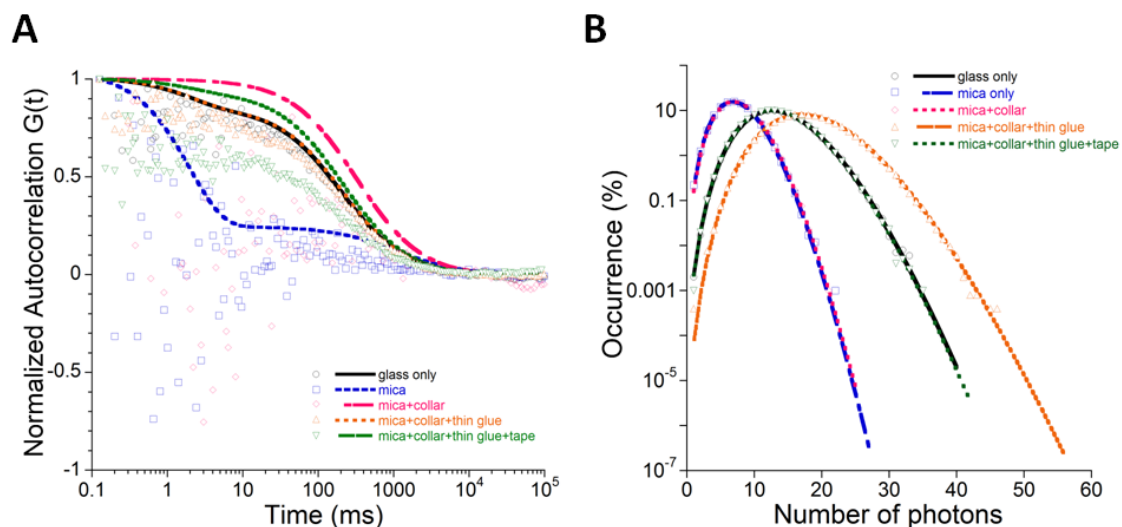
**Table 6: Optimizing coverslip preparation and thickness.**

Sample preparation	Coverslip total thickness ( $\mu\text{m}$ )	Count rate (% of glass sample)	CPP (% of glass sample)
Glass	170		
Mica	250-300	$50.8 \pm 0.1$	$3.1 \pm 2.0$
Mica + collar	250-300	$52.1 \pm 0.1$	$4.1 \pm 2.4$
Mica + collar + thin glue	220-240	$90.8 \pm 1.6$	$76.2 \pm 0.3$
Mica + collar + thin glue + tape	190-220	$95.4 \pm 1.4$	$97.4 \pm 0.5$

**Table 6:** 5-10 s measurements of Alexa 488 in solution were performed with the focal volume positioned 150  $\mu\text{m}$  above the coverslip. The CPP was calculated from FIDA. Description of samples: Glass – standard #1.5 glass coverslip. Mica – mica glued to coverslip; Collar – adjustment of collar on microscope objective to correct for different cover slip thickness; Thin glue – glue was heated to 50  $^{\circ}\text{C}$  prior to adhesion of mica to cover slip; Tape – mica was pressed onto cover slip, excess glue wiped away and top layers of mica removed with tape. Error on measurements is standard deviation from at least 5 measurements.

It has been reported the likely factor contributing to the reduced signal is the additional thickness of the glue and mica layers that are absent in glass only samples (Chiantia et al, 2006). The high numerical aperture objective used for experiments is optimized for

coverslip thickness in the range of 150-250  $\mu\text{m}$ . By adjusting the objective correction collar to a thicker coverslip setting, a modest increase in the count rate and CPP was seen (Table 6). The glass coverslips have a fixed thickness of 170  $\mu\text{m}$ , and mica disks could be reproducibly cleaved to 6-12  $\mu\text{m}$  thick (see Figure 3), thus thinning the glue layer was attempted by several means. By heating the glue to aid in spreading, less adhesive was applied thereby reducing the overall thickness to 220-240  $\mu\text{m}$  which was within the working range of the objective (up to 250  $\mu\text{m}$ ). The resulting improvement in signal was a markedly higher count rate and CPP, up to 80% of the CPP of glass only coverslips. Initially, the freshly cleaved mica was placed onto a drop of glue and allowed to spread under its own weight without being touched further to preserve a pristine surface for a freshly cleaved surface could be formed. This final optimization resulted in recovering ~95% of the count rate and approximately 100% of the CPP of glass only samples.



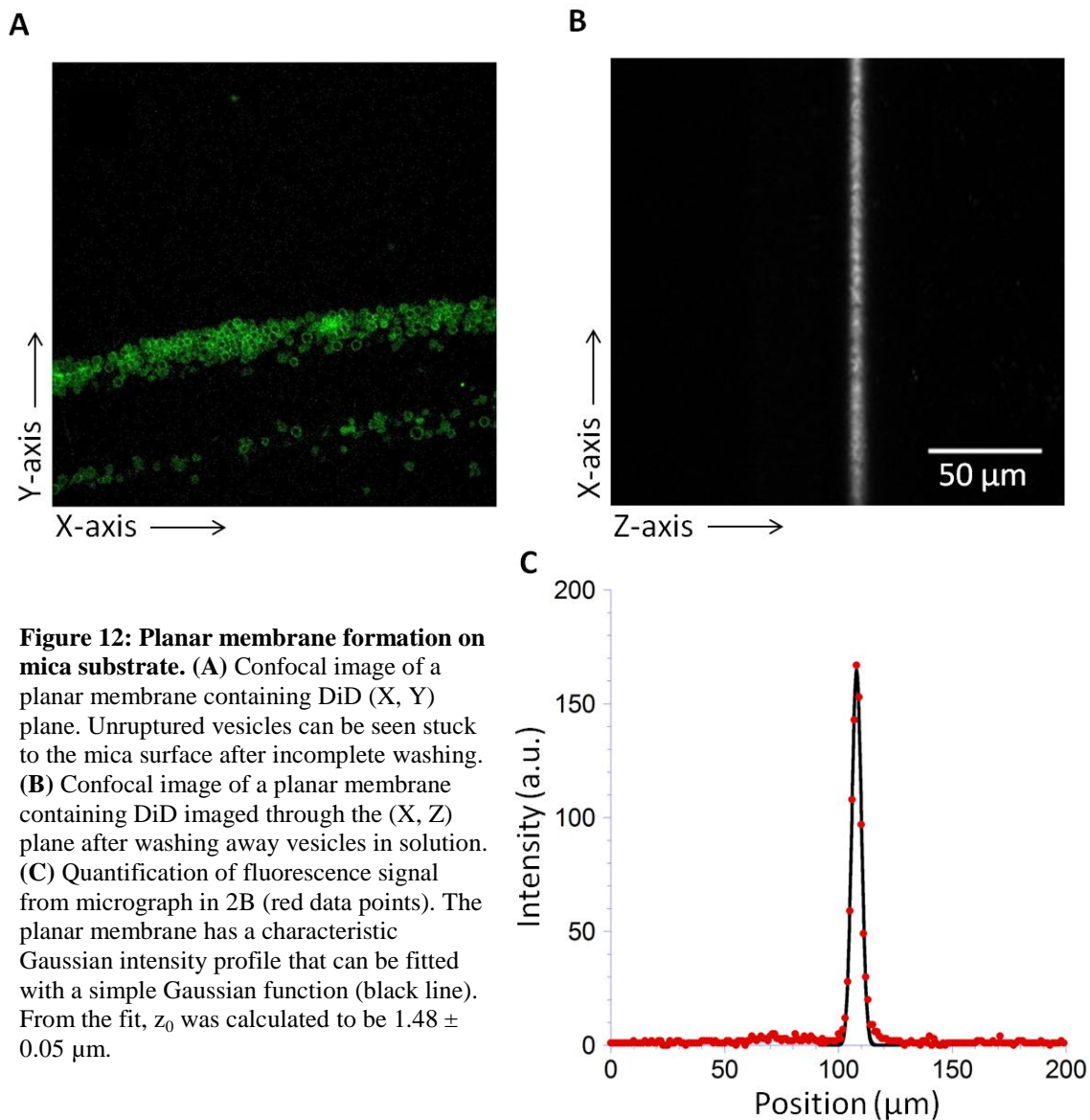
**Figure 11: Autocorrelation and PCH data for different sample preparations.** (A) Normalized autocorrelation data of Alexa488 in solution for different sample preparations. Displayed curves are representative 10 second measurements showing raw data (open symbols) and fits (lines) using Eq. 3a. (B) Photon counting histograms for the same data as in (A). Curves are representative 10 second measurements without beam scanning fitted with a one component model with a double Poisson distribution.

Comparing the FCS and FIDA curves for glass only coverslips to the final optimized preparation (mica + collar + thin glue + tape), the autocorrelation and PCH data are almost identical (Figure 11).

#### *4.2 Characterization of supported lipid bilayer*

Planar membranes were formed via vesicle deposition by incubating mitochondria-like SUVs with the mica substrate. In Figure 12A, vesicles can be seen attached to the mica surface prior to washing away unfused vesicles. After washing, a thin layer of fluorescence corresponding to the dye-labelled membrane can be seen when imaging the membrane in the (X, Z) plane (Figure 12B). This layer only formed in the presence of the mica substrate and was not observed forming on glass coverslips or coverslips with glue (data not shown). Quantifying the fluorescence intensity from the membrane (Figure 12C), it can be seen that the signal corresponding to the membrane is confined to a small diffraction limited thickness in the Z dimension as expected. From the Gaussian fit, a value for  $z_0$ , the radius of the focal volume in the axial dimension, was calculated to be  $1.48 \pm 0.05 \mu\text{m}$ . This value is close to the value measured by FCS,  $1.30 \mu\text{m}$ .

To assess the fluid properties of the planar membrane that was forming, diffusion in the plane of the membrane was measured by FCS. A Lipophilic membrane tracer or dye-labelled lipid was included in the mitochondria-like lipid mixture and their translational diffusion in the membrane was observed (Table 7, Figure 13). The values suggest that diffusion in the plane of the membrane occurs with a diffusion coefficient of  $3\text{-}6 \mu\text{m}^2/\text{s}$  depending on the dye used. These rates are slightly faster than those previously



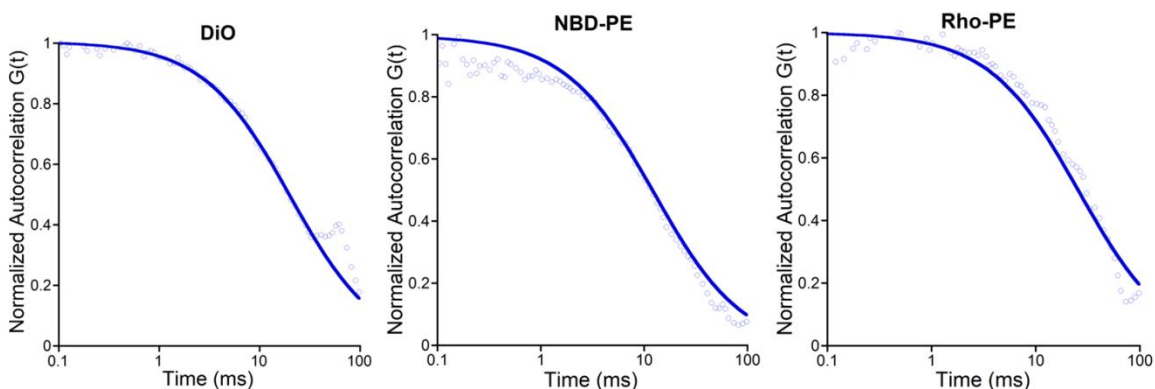
reported for similar planar membrane systems (Chiantia et al 2006; Huang et al 1992), but are well within the expected range for lipid diffusion.

Next, the lamellarity of the membrane was assessed. Ideally, it is desired that the planar membrane should be a single planar bilayer, and not membrane stacks, so that pore forming proteins such as Bax do not tunnel through multiple membrane layers. The average brightness per surface area for the SUVs used to form the membrane was

**Table 7: Diffusion coefficients for lipids and tracers in planar membranes**

Dye/lipid	Mass %	Mol %	Diffusion coefficient ( $\mu\text{m}^2/\text{s}$ )	Published diffusion coefficients ( $\mu\text{m}^2/\text{s}$ )	Number of particles (N)	Molecular brightness (kHz)
DiO	0.002	0.018	$5.8 \pm 0.6$	$1.73 \pm 0.12$ (Chiantia et al, 2006)	$0.69 \pm 0.39$	$2.34 \pm 0.45$
NBD-PE	0.5	4.48	$5.8 \pm 1.8$	1.2-2.5 (using FRAP, Huang et al, 1992)	$18.6 \pm 17.1$	$20.5 \pm 27.2$
Rho-PE	0.05	0.315	$3.1 \pm 1.7$		$2.31 \pm 1.95$	$28.1 \pm 27.3$

**Table 7:** Fluorescently-labelled lipids or a lipophilic tracer (DiO) were added 1mg mitochondria-like lipid films in the amounts indicated. Diffusion in the plane of the membrane was measured by FCS, with the focal volume centered close to the plane of the membrane. The error indicated is the standard deviation from at least 5 measurements.



**Figure 13: Normalized autocorrelation data for diffusion in the plane of the membrane.** Curves are representative measurements of fluorescently labelled PE or the lipidic tracer DiO. Open circles show the raw data and solid lines show the fits to the data with Eq. 3a. All measurements were recorded with the focal volume centered at the plane of the membrane.

compared to the average brightness per surface area in the planar membrane that formed.

Vesicle surface area was calculated as the surface area of a sphere with radius 50nm multiplied by 2 (for each leaflet). Planar membrane surface area was calculated from the dimensions of the imaged area multiplied by 2. Since SUVs were used for vesicle fusion,

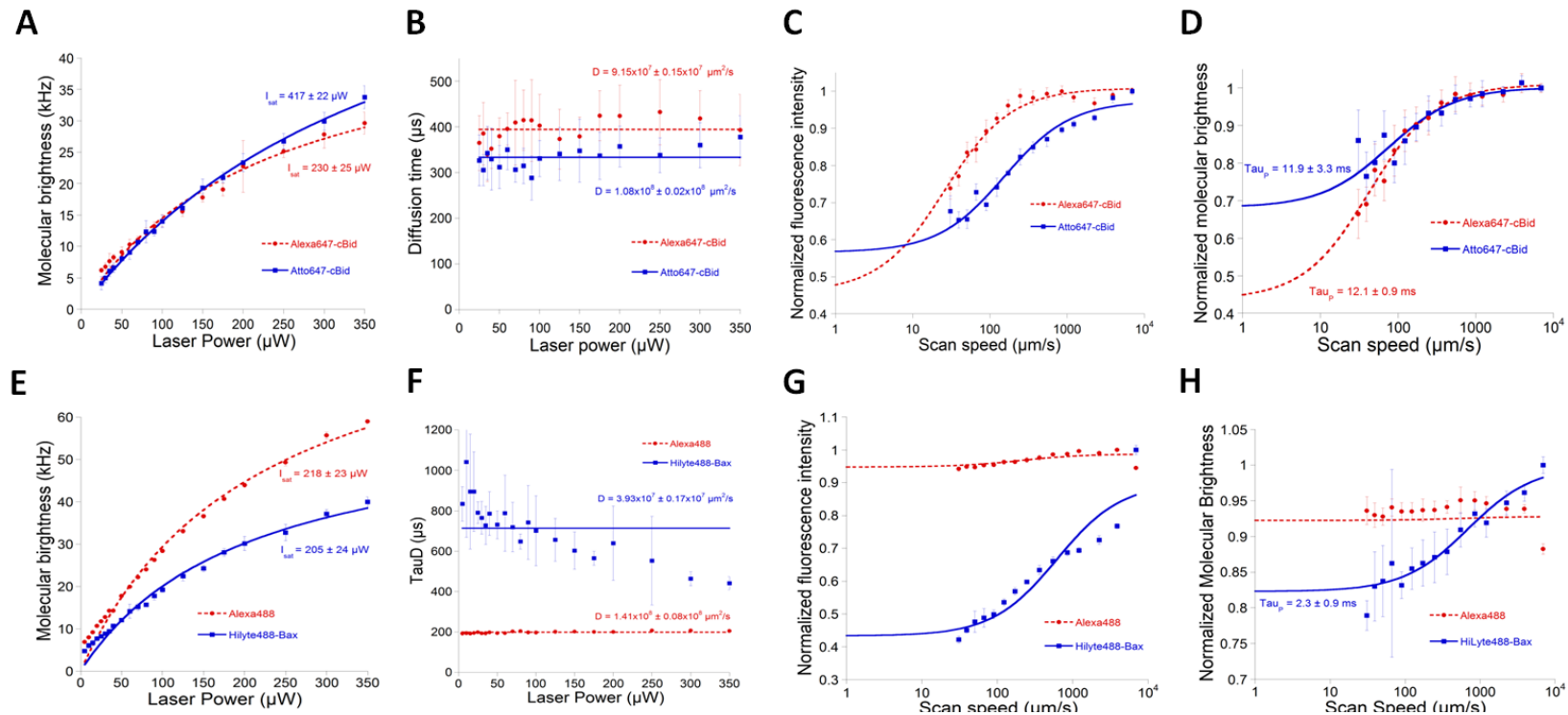
the resulting planar membrane was expected to be a single bilayer. If a single planar bilayer was present, the brightness per surface area in the planar bilayer and SUVs would be equal. Using FIDA, the brightness of vesicles was determined by measuring a sample of SUVs in solution, and the brightness in the planar membrane was measured imaging the planar membrane through the X, Z plane and quantifying brightness per area from micrographs. Doing so resulted in a 2-fold deficit in brightness per surface area in the planar membrane compared to SUVs measured in solution by FCS. This would suggest that the planar membrane layer exists as a monolayer and not the expected bilayer. Alternatively the planar membrane may have formed in patches. However, confocal imaging showed that the membrane was continuous across areas up to 200  $\mu\text{m}$  wide (Figure 12B). To dismiss the possibility that not all the dye in vesicles was being incorporated into the planar membrane, samples with different concentrations of dye were used. An increase in dye corresponded to a proportional increase in the fluorescence signal at the membrane suggesting that the dye was successfully being incorporated (data not shown). The confocal imaging method used here assumes that for the total signal from the membrane to be recorded, the plane of the membrane must pass through the centre of the confocal volume during imaging. Since the expected thickness of the planar bilayer ( $\sim 5$  nm) is a fraction of the axial length of the focal volume (1.48  $\mu\text{m}$ ), it is possible that the centre of the focal volume (the maximum intensity of the excitation beam) may not exactly pass through the plane of the membrane. As a result, the maximum signal from the membrane will not be detected. Furthermore, since dye in the planar membrane is restricted to diffusion in 2 dimensions, and diffuses much slower

(perhaps not diffusing at all in the lower leaflet) than SUVs diffusing in solution, photobleaching is a factor that may reduce the recorded intensity. The difference in the position of the focal volume center relative to the plane of the membrane and photobleaching effects, might account for the lower than expected fluorescence of the planar membrane.

#### *4.3 Assessing dye photostability*

To assess the suitability of the fluorescent protein constructs for single molecule measurements, the effect of short term photobleaching on fluorophore brightness was investigated. The Alexa series of dyes have been extensively used and characterized in single molecule fluorescence fluctuation experiments and are used here as standards. Samples of cBid labelled with Alexa647 and Atto647 in buffer were compared. HiLyte488 labelled Bax was compared to Alexa488 free dye in buffer. Fluorescence fluctuation experiments were carried in a 96-well microplate with coverslip bottom. Equal concentrations of cBid labelled with Alexa647 or Atto647 were measured with increasing laser power in the absence of beam scanning. The measured diffusion times (Figure 14B) of the labelled proteins were in the range of 300-400  $\mu$ s as expected for monomeric protein diffusing in solution. The fluorescence profile of the two dyes was very similar. Molecular brightness (Figure 14A) increased with laser power, with saturation occurring at 230  $\mu$ W for Alexa647 and 417  $\mu$ W for Atto647 based on the fit of the data. Still the molecular brightness of both dyes appeared almost identical. The photobleaching times ( $\tau_P$ ) measured for the dyes as a function of scan speed, using a method developed by Satsoura et al (2007) (Figure 14D) are similar, though it appeared that Alexa647 ( $\tau_P=12.1$





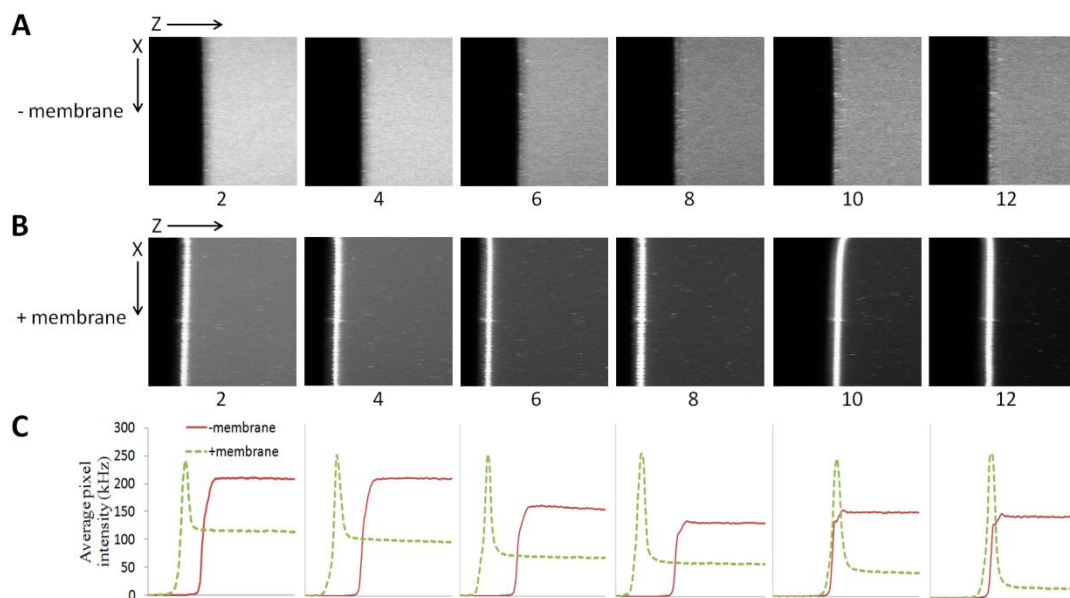
**Figure 14: Photostability of HiLyte488 and Atto647 compared to similar Alexa fluors.** A-D) cBid labelled with Alexa647 and Atto647 were measured in assay buffer. (A) Molecular brightness as a function of laser power fit with Eq. 4. (B) Diffusion times for labelled proteins in buffer obtained from fitting ACFs from (A) in the absence of beam scanning. (C) Normalized fluorescence intensity and (D) normalized specific brightness as a function of scan speed with circular beam scanning radius of 45  $\mu\text{m}$  and scanning frequency varied from 0-24.5 Hz at a constant laser power (250  $\mu\text{W}$ ). Data was fitted using Eq. 5. E-H) Alexa488 (Carboxylate salt) and Bax labelled with HiLyte488 were measured in assay buffer. (E) Molecular brightness as a function of laser power fit with Eq. 4. (F) Diffusion times for fluorophores in buffer obtained from fitting ACFs from (e) in the absence of beam scanning. (G) Normalized fluorescence intensity and (H) normalized specific brightness as a function of scan speed with circular beam scanning radius of 45  $\mu\text{m}$  and scanning frequency varied from 0-24.5 Hz at a constant laser power (250  $\mu\text{W}$ ). Data was fitted with Eq. 5. For all plots error bars indicate standard deviation ( $n=9$ ).

ms) is marginally more resistant to photobleaching than Atto647 ( $\tau_p = 11.9$  ms). As expected, higher scanning speeds reduced photobleaching of both Alexa- and Atto647 indicated by increases in both the normalized fluorescence intensity (Figure 14C) and molecular brightness (Figure 14D).

For blue laser excitable dyes, HiLyte488 was compared to Alexa488. Equal concentrations of HiLyte488 labelled Bax and Alexa488 (free carboxylate salt) in assay buffer were measured in a 96-well microplate. The diffusion time for HiLyte488-Bax showed a high degree of variability, but generally decreased with increasing laser power (Figure 14F). However, as expected the diffusion time for the labelled protein was always higher than the diffusion time of the free Alexa488 dye. Molecular brightness as a function of laser power was similar for both HiLyte488-Bax and Alexa488, with saturating intensities of 205  $\mu\text{W}$  and 218  $\mu\text{W}$ , respectively (Figure 14E). When normalized intensity (Figure 14G) and normalized molecular brightness (Figure 14H) as a function of scan speed was assessed, there was little dependence on the scan speed for Alexa488 brightness (as expected for a fast diffusing fluorophore for which little photobleaching would happen in the absence of scanning). This was also reflected in a long photobleaching time of 87.8 ms. In contrast HiLyte488-Bax showed a marked increase in molecular brightness at high scan speed indicating photobleaching occurred at low speeds (Figure 14H, data taken at high laser power  $P = 250$   $\mu\text{W}$ ). This was also reflected in the photobleaching time for HiLyte488-Bax which was 2.3 ms.

#### 4.4 cBid and Bax bind supported bilayers with specificity

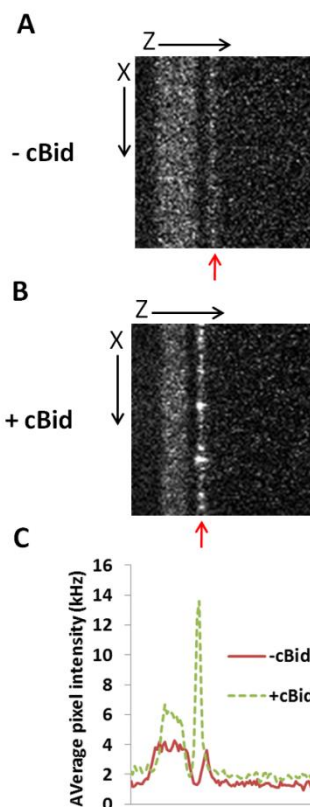
Once Atto647-cBid and HiLyte488-Bax photostability and activity was confirmed, the interaction of labelled proteins with planar membranes was characterized by confocal imaging. When a SLB is present, cBid rapidly accumulates at the plane of the membrane (compare Figure 15B where a membrane is present with Figure 15A when no membrane is present). In the presence of a membrane, upon addition of 25 nM cBid, the signal at the membrane becomes saturated at ~250 kHz within 2 minutes of adding cBid (Figure 15C). However, the cBid signal in solution steadily decreases over time (compare Figure 6C green curve at time 2 min vs. 12 min) suggesting some non-specific binding to the sides of the sample chamber. In the absence of a SLB, there is no discernible cBid



**Figure 15: cBid specifically binds mitochondria-like SLBs.** A-B) Time course confocal images through the (X, Z) plane at 2 minute intervals after addition of Atto647-cBid (25 nM) incubated with (A) mica substrate alone or (B) mica with a SLB present. The top of the sample is towards the right of the images. Imaging conditions: 100x100  $\mu\text{m}$  area imaged in 100x100 pixels; pixel dwell time was 1ms; laser power  $P = 25 \mu\text{W}$ . (C) Intensity profile of micrographs. The average pixel intensity at every position along the Z-axis for the images above is plotted. When a membrane is present, cBid signal at the membrane saturates within 2 minutes.

binding even after 12 min (Figure 15A) with a large amount of cBid remaining in solution (compare Figure 15C red vs. green curves after 12 min). In the absence of a membrane, a gradual decrease in the solution signal was also observed, likely due to non-specific binding, and stabilized after 6 minutes. Taken together, the data suggests that cBid binds with high specificity to mitochondria-like SLBs but not to mica surfaces.

In liposomes, cBid is required for Bax membrane binding and permeabilization. To further validate the mitochondria-like SLB, it was necessary to determine if cBid was required for Bax binding. In the absence of cBid, some HiLyte488-Bax appears to bind the membrane (Figure 16A). The average pixel intensity at the plane of the membrane was ~4 kHz in this case compared to ~14 kHz in the presence of cBid (Figure 16C). This shows that Bax membrane binding is promoted by cBid. The area of signal below the plane of the membrane (area of signal to the left of the membrane in images 16A-B) is likely due to the layer of glue which appears to fluoresce weakly when excited with the 488nm laser. This signal from the glue is low (4-6 kHz), but appears since the intensity at the membrane itself is relatively low due to the low concentration of protein used and due to washing prior to imaging.

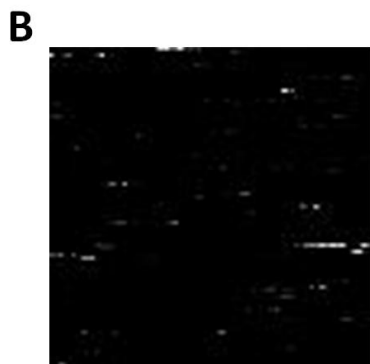
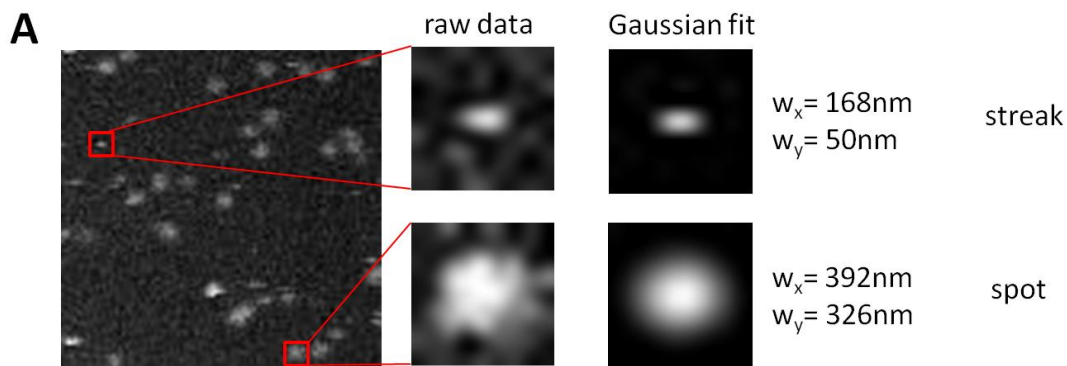


**Figure 16: Bax specifically binds planar bilayers when cBid is present.** A-B) Confocal images through the Z, X axes of Hilyte488-Bax (2 nM) incubated with SLBs for 1 hour (A) without or (B) with cBid. The protein remaining in solution was washed away with buffer prior to imaging in order to better locate the plane of the membrane (indicated by the red arrow). The top of the sample is towards the right of the images. Imaging conditions: 100x100  $\mu\text{m}$  area imaged in 100x100 pixels; pixel dwell time was 1 ms; laser power  $P = 5 \mu\text{W}$ . (C) Intensity profile of micrographs. The average pixel intensity at every position along the Z-axis in (A) and (B) is plotted. Average pixel intensity at the plane of the membrane was  $\sim 4$  kHz in the absence of cBid and  $\sim 14$  kHz when cBid was present.

#### 4.5 Confocal imaging of protein binding to SLBs with single molecule resolution

Once it was established that fluorescently labelled cBid and Bax were able to bind planar membranes with specificity, confocal imaging was performed to observe protein binding to SLBs with single molecule resolution. As described in methods section 2.11.2., a theoretical cBid concentration of 4.68 pM was calculated in order to resolve single molecules bound to planar membranes in the experimental setup used. In practice, such a low concentration did not yield sufficient protein binding to observe diffraction limited spots when imaging the membrane. By increasing the cBid concentration to 400 pM, diffraction limited spots of membrane bound cBid were observed. Unexpectedly, streaks (similar to protein diffusing in solution) were also observed at the plane of the membrane

(Figure 17). This suggested that cBid at the membrane exists in two populations: immobile membrane bound protein (diffraction limited spots) and mobile membrane associated protein (streaks). This is supported by TIRF video imaging of fluorescent cBid and Bax incubated with SLBs that clearly shows immobile membrane bound protein and mobile diffusing protein. Since TIRF can only illuminate particles within ~200 nm of the coverslip surface, it can be said that the mobile proteins are closely associated with the membrane since mobile spots remained in focus for extended periods up to 10 seconds before leaving the plane of the membrane or photobleaching. Interestingly, the dynamics seen in TIRF movies show mobile protein that became immobile (and the converse) during the course of video imaging. Confocal imaging lacks temporal resolution such that dynamics of protein diffusion can only be seen as a single point in time since the time



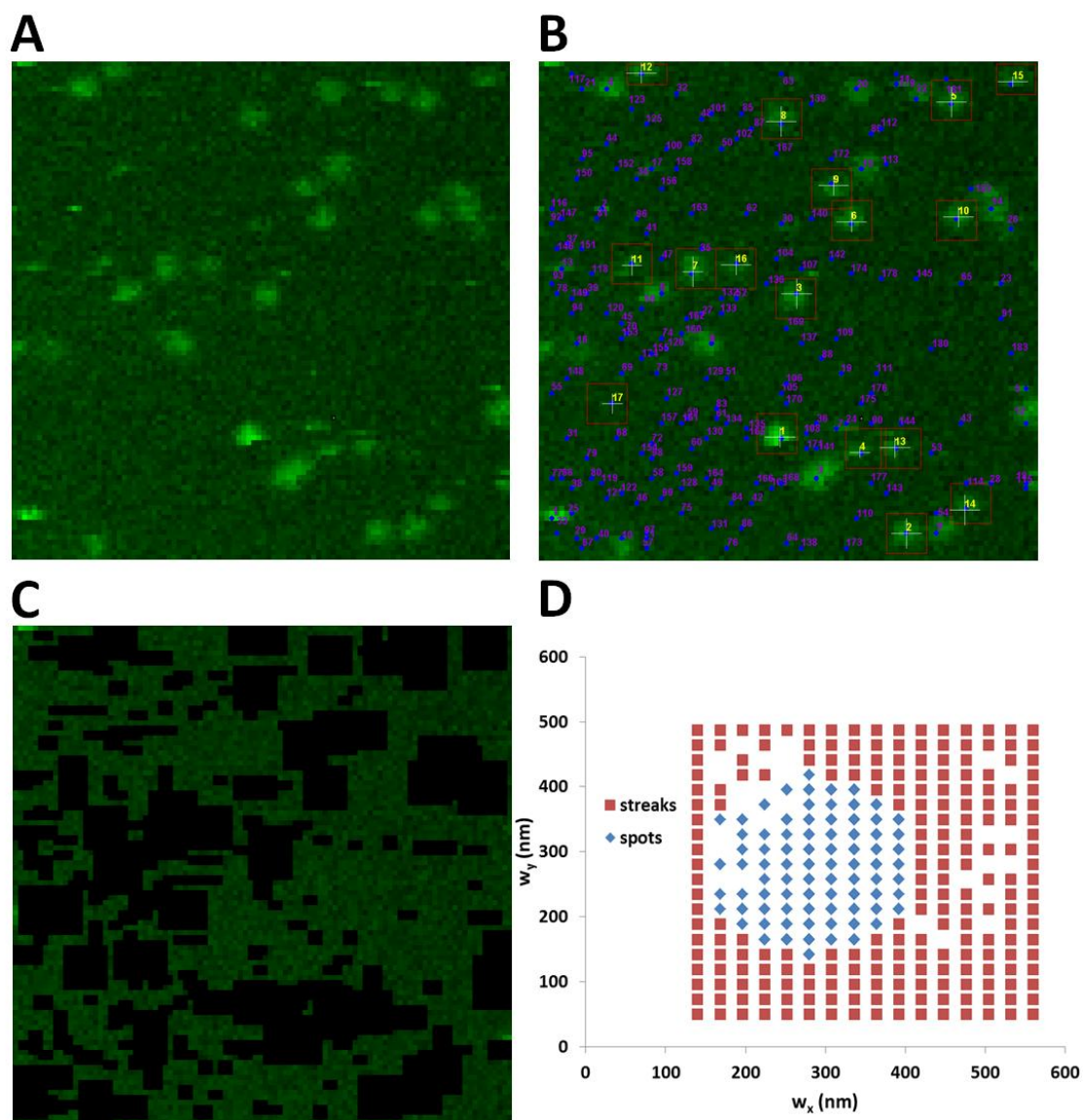
**Figure 17: Confocal images of cBid at the plane of the membrane and in solution.** Imaging conditions: 10x10  $\mu\text{m}$  area acquired in 100x100 pixels. Pixel dwell time of 1ms and laser power  $P = 25 \mu\text{W}$ . **(A)** 400 pM cBid spots and streaks at the plane of the membrane. Average pixel intensity was 39.5 kHz, with a minimum pixel intensity of 20.4 kHz (1 pixel). Close up images of a streak and spot with corresponding  $w_x$  and  $w_y$  fit values are shown. **(B)** 400 pM cBid imaged in solution. Average pixel intensity was 4.9 kHz with a minimum pixel value of 2.1 kHz (549 pixels).

required to acquire the image is much greater than the rate of protein diffusion. Thus, it is not unexpected that mobile proteins appear as streaks in confocal images. It is important to note that a mobile protein will only appear “streak-like” (as a line in the image) if the particle happens to be slow enough to appear immobile on the time scale of a line scan or if it happens to travel in the same direction as the scan. For fast moving particles not moving in the direction of the scan, streaks will only appear at a single pixel in the image.

#### *4.6 Automated image analysis for detection and sorting of fluorescent proteins*

Once it was discovered that protein in the plane of the membrane is present as immobile spots and mobile streaks, automated image analysis was used to sort and quantify the data in confocal images. A program was written to classify objects in confocal images as either streaks or (diffraction limited) spots and to quantify their intensity using a Gaussian fitting procedure based on the method of analysis developed by Henriquez et al. (2010) (see Appendix). Objects were detected in order from highest to lowest intensity with each detected object erased from the image prior to locating the next object with highest intensity. Thus, the numbers in Figures 18-20 indicate the order objects were detected and also go in sequence from highest to lowest intensity. Note that spots and streaks are numbered as two separate groups.

Figure 18 shows all detected objects at the plane of the membrane for an image of Atto647-cBid. Images at the plane of the membrane had a significant level of background signal indicated by few (often one) pixels of low intensity value compared to images acquired completely in solution which contained many pixels with low intensity value of 0-4 kHz (Figure 17). Typically, for an image of Atto647-cBid at the plane of the



**Figure 18: Objects detected by automated image analysis.** (A) RGB copy of the original representative  $10 \times 10 \mu\text{m}$  16-bit confocal image for 400 pM Atto647-cBid at the plane of the membrane. (B) Numbers refer to the order of detected spots (yellow numbers) and streaks (violet numbers). Blue points show the brightest pixel in each object detected. Crosses are centred at the calculated centre of mass for spots. Length of crosses in the x and y dimension correspond to  $w_x$  and  $w_y$  respectively. Red boxes are visual aids to locate spots. (C) Regions with detected objects erased. (D)  $w_x$  and  $w_y$  values from Gaussian fitting for all detected objects. cBid spots (blue) cluster in the same region and are distinct from streaks (red). Data shown is from 21 images comprising 3 separate experiments.

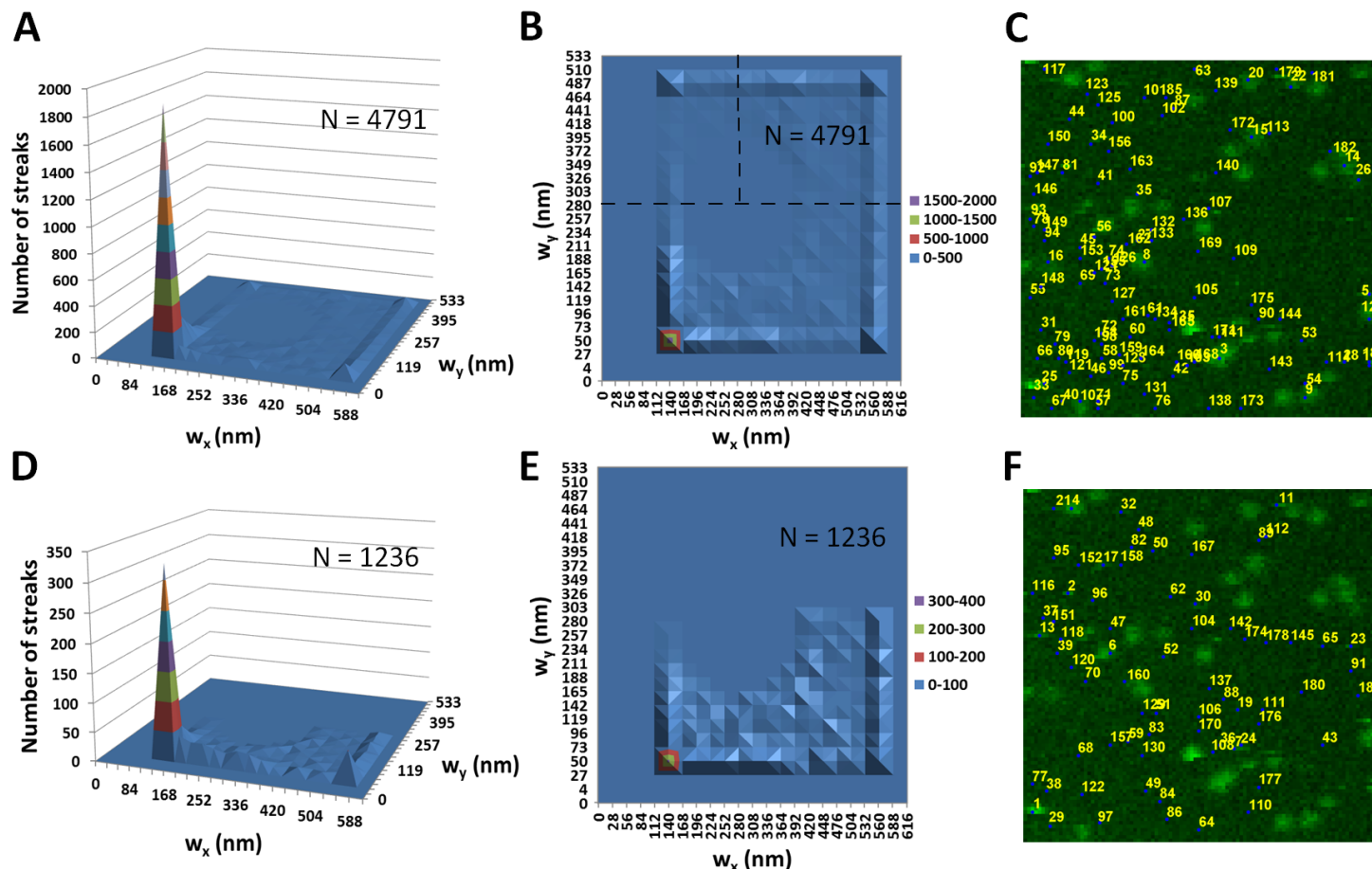
membrane, the lowest pixel value was 20-40 kHz. A threshold was set for each image: the average pixel intensity in the image plus 50% of the CPP of the fluorescent protein



measured in solution by FIDA (refer to Methods 2.13). This threshold was sufficient to detect all objects of interest (compare Figure 18A and 18C). Around all pixels above the threshold, an area corresponding to the Airy disc radius of point sources under the imaging conditions used was defined. The centre of mass for the area was calculated and Gaussian fitting was performed to obtain an accurate estimate for the intensity of detected objects to assess the oligomeric state of fluorescent proteins. For Gaussian fitting 4 parameters were varied: the maximum intensity, the noise level, the height and widths of the Gaussian along the X and Y axes (refer to Methods 2.13). The primary criteria for classifying detected objects as spots or streaks was the fit-obtained values for  $w_x$  and  $w_y$ , calculated using Eqs. 16 and 17 respectively, which correspond to the Airy disc radius in the x and y dimensions. Objects with both  $w_x$  and  $w_y$  within the accepted boundaries (Table 4) were classified as spots (Figure 18B, outlined in red with yellow numbers), while all other objects were deemed streaks (numbered in violet). As expected, cBid diffraction limited spots clustered around the theoretical value of 280 nm for  $w_x$ ,  $w_y$  (Figure 18D).

Stringent criteria were used such that only objects that were diffraction limited, sufficiently resolved and had a Gaussian intensity profile were used in subsequent analysis. The detected spots and streaks were further sorted as “good” or “bad” Gaussian objects based on the fit-obtained values for intensity ( $I_{fit}$ ) and background ( $B_{fit}$ ) calculated by Eqs. 14 and 15, respectively. The majority of streaks detected clustered at small values of  $w_x$ ,  $w_y$ , as expected, corresponding to the lower limit of the fitting range for those parameters (Figure 19A). However, there were also a number of streaks that had

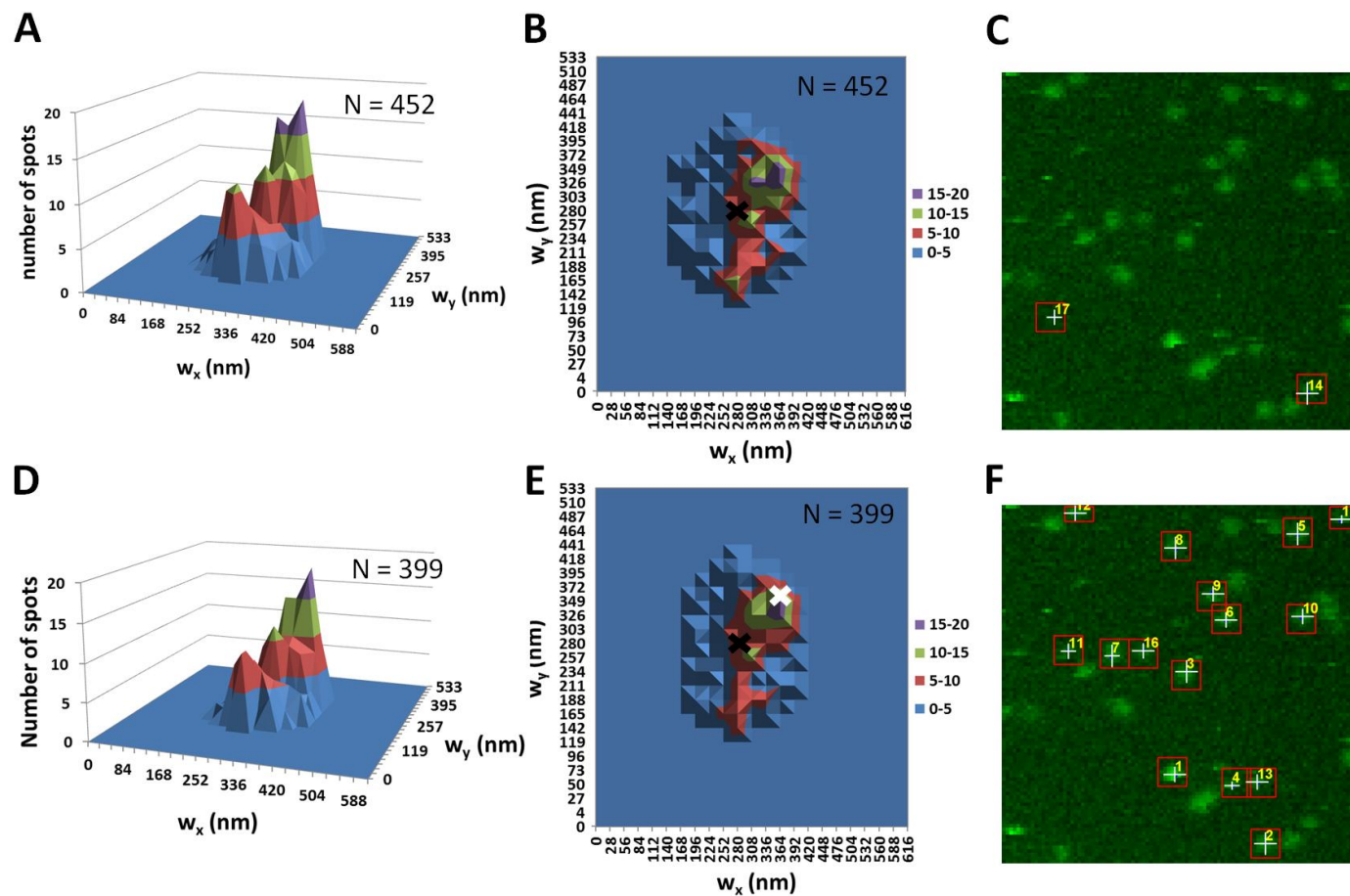
unexpectedly large values for  $w_y$  greater than 280 nm. Based on the imaging conditions, it should not be possible for streaks to have large values of  $w_y$  greater than 280 nm since the same streak can not to be imaged across two adjacent rows of pixels. However, a large  $w_y$  component could result from 3 scenarios: (1) Streaks with a large  $w_y$  component, but a small  $w_x$  component were the result of multiple streaks (or a streak and a spot) that were adjacent to each other and fitted as a single object (e.g. streak #179 in Figure 19C). These streaks clustered in the top left quadrant in Figure 19B. (2) Streaks with a large  $w_y$  component and a small  $w_x$  could also result from a streak being adjacent to a previously erased area thereby cutting short its  $w_x$  component. These streaks also clustered in the top left quadrant in Figure 19B. (3) Streaks with a large  $w_y$  and large  $w_x$  component (e.g. streak #9, # 14 in Figure 19C) were the result of out-of-focus spots or two spots that were not sufficiently resolved as distinct objects. These “streaks” clustered in the top right quadrant in Figure 19B. In the three aforementioned cases, those objects were classified as “bad” and excluded from further analysis since their intensity cannot be accurately determined by Gaussian fitting. Thus, any streak with a  $w_y$  component greater than 280 nm for Atto647-cBid or greater than 240 nm for HiLyte488-Bax was excluded from analysis. A further complication is spots located near the edges of the image may be mistakenly classified as streaks due to having one long  $w$  component and one short. To avoid this, pixels located in the outer 3 rows of pixels in the image were not analyzed when finding points of highest intensity. However, Gaussian fitting of objects that extended into the outer 3 rows of pixels was allowed provided the brightest pixel was not located in one of the outer 3 rows.



**Figure 19: Sorting of mobile protein streaks.** Data shown in A, B, D and E is from 21 images comprising 3 separate experiments. N values are the total number objects in the plotted distribution.  $w_x$  and  $w_y$  values were obtained from Gaussian fitting of objects and calculated using Eqs. 16 and 17, respectively. (A) Size distribution for all streaks detected. (B) Same data as (A) plotted in 2D. The horizontal line bisecting the y-axis at 280 nm is the  $w_y$  cutoff value for good streaks. The vertical line is the boundary between out-of-focus spots and rejected streaks. (C) Representative image showing locations of "bad" streaks. (D) Size distribution of streaks classified "good." (E) Same data as (D) plotted in 2D. (F) Representative image showing locations of "good" streaks.

The size distribution of well fitted Gaussian streaks is shown in Figure 19D. The distribution of “good” streaks mirrors the general distribution for all streaks (with the exception of those excluded for large  $w_y$ ). However, the number of good streaks clustered at low  $w_x$  and  $w_y$  is much lower (compare number of streaks at low values in Figure 19A with 19D). This was due to the majority of small streaks being classified as “bad” for the intensity component of the fit ( $I_{\text{fit}}$ ) reaching the lower boundary of the fit range (refer to Table 4). In other words, these streaks had a low intensity not sufficiently above the background to result in a good Gaussian fit.

The size distribution of “good” cBid spots (Figure 20D, E) was nearly identical to the distribution of all detected spots (Figure 20A, B). Both distributions were centered on the theoretical  $w_x$ ,  $w_y$  value of 280 nm because of the choice made in the analysis routine to identify spots as objects with radii around this value. Strikingly, most good spots clustered around the experimentally determined  $w_0$  value of 360 nm (white “X” in Figure 20E) determined by measuring Alexa647 diffusion in solution by FCS and calculating  $w_x$  from Eq. 13. As stated in section 2.11.1 this value is closer to the actual resolution of the instrument and implies that most of the spots are indeed diffraction limited. Of the objects classified as spots, the majority fit the above criteria and were accepted as “good” (Figure 20F). The few spots that were rejected (Figure 20C) were all due to the intensity component of the fit ( $I_{\text{fit}}$ ) reaching the lower boundary of the fit range. For fluorescent Bax images the same general criteria for classifying spots and streaks and sorting good and bad Gaussian fitted objects was applied. However, the cut-off values for the size of the objects were modified, since the blue 488 nm laser was used for excitation, and

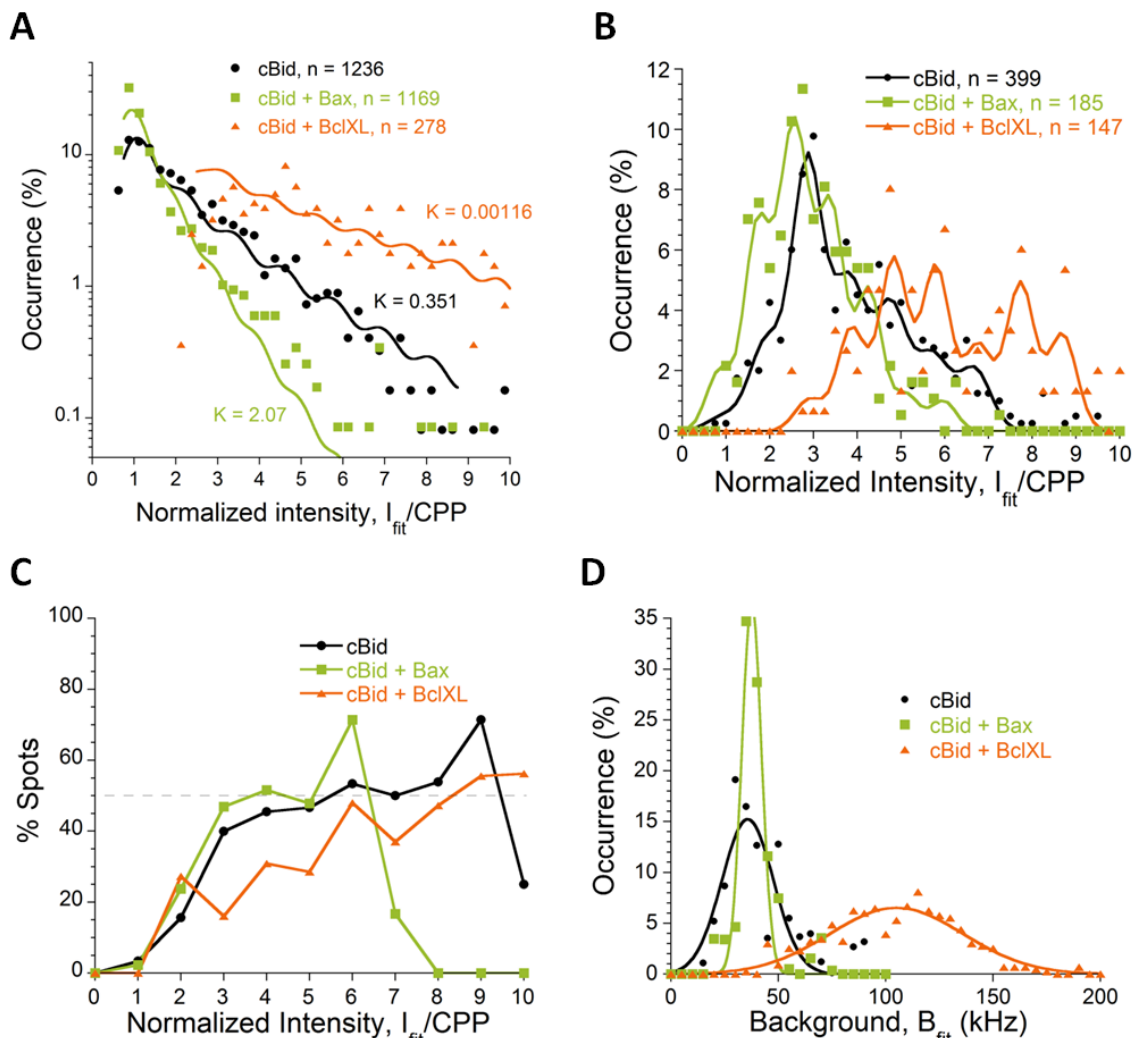


**Figure 20: Sorting of mobile protein spots.** Data shown in A, B, D and E is from 21 images comprising 3 separate experiments.  $N$  values are the total number objects in the plotted distribution.  $w_x$  and  $w_y$  values were obtained from Gaussian fitting of objects and calculated using Eqs. 16 and 17, respectively. **(A)** Size distribution for all spots detected. **(B)** Same data as (A) plotted in 2D. The black "X" indicates the theoretical value for  $w_y$  and  $w_x$  (280 nm) **(C)** Representative image showing locations of "bad" spots. **(D)** Size distribution of spots classified "good." **(E)** Same data as (D) plotted in 2D. The black "X" indicates the theoretical value for  $w_y$  and  $w_x$  (280 nm). The white "X" indicates the experimentally determined value for  $w_x$  by FCS (360 nm) **(F)** Representative image showing locations of "good" spots.

therefore the diffraction limited spots observed were smaller. Consequently, the corresponding  $w_y$  cut-off for rejecting streaks was chosen to be 240 nm. At 488 nm excitation, the experimentally determined value for  $w_x$  was 320 nm calculated using Eq. 13 by measuring Alexa488 in solution by FCS.

#### *4.7 Quantification of cBid binding to supported bilayers*

Confocal images of Atto647-cBid binding to SLBs were quantified by automated image analysis. The intensity value obtained from Gaussian fitting of detected objects ( $I_{\text{fit}}$ ) was normalized by the molecular brightness (CPP) of monomeric cBid measured in solution by FIDA. Data was then binned according to intensity values to better illustrate trends and clusters. It is important to note that normalized data represent the relative and not absolute size of complexes, owing to 71% cBid labeling efficiency and photon noise in the system. Thus intermediate values between integers are expected and are observed when the data is binned. In Figure 21 the probability distribution of the relative size of mobile and immobile Atto647-cBid complexes suggest that cBid is able to form complexes in SLBs and that these complexes have a higher probability of being immobile than the monomer. Considering the data for mobile cBid at the membrane (Figure 21A), most mobile particles appear to be monomers when cBid alone was incubated with SLBs. On the contrary, for immobile cBid complexes, larger oligomers were more abundant (Figure 21B). In the presence of a Bcl-2 binding partner (Bax or Bcl-XL) a shift in the relative size of these mobile cBid complexes was seen. In the presence of Bax, the vast majority of mobile cBid at the membrane still appears to be monomeric with an overall shift toward smaller cBid complexes. When cBid was incubated with Bcl-XL on the



**Figure 21: Characterizing cBid binding to supported bilayers.** 400 nM Atto647-cBid alone (circles), or with 2 nM WT Bax (squares) or with 2 nM WT Bcl-XL (triangles) were incubated with SLBs and imaged. The CPP for monomeric cBid measured by FIDA was 20 kHz. Data for cBid alone was quantified from 18  $10 \times 10 \mu\text{m}$  confocal images comprising 3 separate experiments. Data for cBid + Bax/Bcl-XL was quantified from 18 images in a single experiment. In (A, B) a bin size of 0.25 was used for normalized intensity data. In (C) a bin size of 1 was used. (A) Distribution of mobile cBid (streaks) at the membrane. Symbols show experimental data and solid lines are probability distributions calculated from Eq. 18. The cBid-cBid dissociation constant,  $K$ , in units of molecules/ $\mu\text{m}^2$  was calculated from Eq. 18. (B) Distribution of immobile Bid (spots) at the membrane. Symbols show experimental data and solid lines are fits calculated using equation 21. (C) The percentage of immobile cBid (spots) as a function of normalized intensity. At 50% (dashed line) an equal amount of immobile and mobile cBid exists at a given normalized intensity. (D) Distribution of background ( $B_{fit}$ ) values for data in (A) and (B). Lines are Gaussian fits to the data.

other hand, a shift to larger mobile complexes was seen. A similar tendency was observed for immobile cBid complexes (Figure 21B). Data for cBid alone showed an

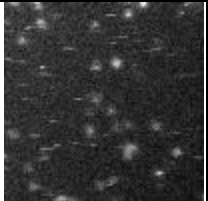

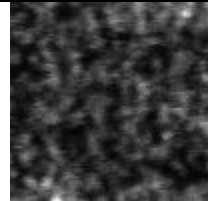
intermediate relative oligomer size distribution. When Bax was present, the distribution of immobile cBid complexes shifted to smaller complex sizes. In the presence of Bcl-XL an opposite shift toward larger complexes was observed.

A simple association model (Eq. 18) was applied to the mobile cBid data and dissociation constants for cBid-cBid interactions were obtained. Considering the  $K_D$  values in Figure 21A, it can be said that cBid affinity for itself increases according to: cBid+Bax < cBid < cBid+Bcl-XL. Interestingly, this trend was reflected in the percentage of immobile spots (as a percent of all objects detected) at the point where an equal number of immobile and mobile cBid exists for a given normalized intensity (Figure 21C). For cBid alone this point was at a normalized intensity of 5. When Bax was present this point was shifted to ~3 and with Bcl-XL was ~6. Finally, the distribution of the background levels ( $B_{fit}$ ) for all objects deemed to have a good Gaussian fit is shown in Figure 21D. Within a given set of experiments the background values fit a Gaussian distribution. The cBid + Bcl-XL data had a markedly higher background than the data for cBid alone or cBid in the presence of Bax. This likely reflects the large amount of cBid present at the plane of the membrane when incubated with Bcl-XL (see Discussion 5.5).

The total amount of cBid (mobile + immobile) at the plane of the membrane varied depending on the presence of a binding partner (Table 8). When cBid with Bax was incubated with SLBs, a concentration of 2.3 cBid molecules/ $\mu\text{m}^2$  (calculated by Eq. 21 based on total fluorescence intensity) was measured at the plane of the membrane which was slightly lower than for cBid alone (2.7 molecules/ $\mu\text{m}^2$ ). On the contrary, with



**Table 8: Membrane bound cBid quantified from confocal images**

	cBid + Bax	cBid (alone)	cBid + Bcl-XL
<b>Representative Image</b>			
<b>cBid concentration at membrane (molecules/<math>\mu\text{m}^2</math>)</b>	2.3	2.7	11.6
<b><math>K_D</math> (<math>\mu\text{M}</math>)</b>	49.04	121.0	35.65
<b>mobile:immobile cBid ratio</b>	6.3	3.1	1.9

**Table 8:** Representative images of the different cBid binding experiments are shown with the cBid concentration at the plane of the membrane, the binding constant for cBid binding to lipids in SLBs and the ratio of mobile to immobile cBid. For all experiments the concentration of cBid injected into the sample chamber was 400 pM. Quantitative data was obtained as an average from 18 confocal images in each experimental condition. cBid concentrations at the membrane and  $K_D$  were calculated from Eqs. 21.  $K_D$ s for cBid binding to SLBs were calculated using Eq. 23.

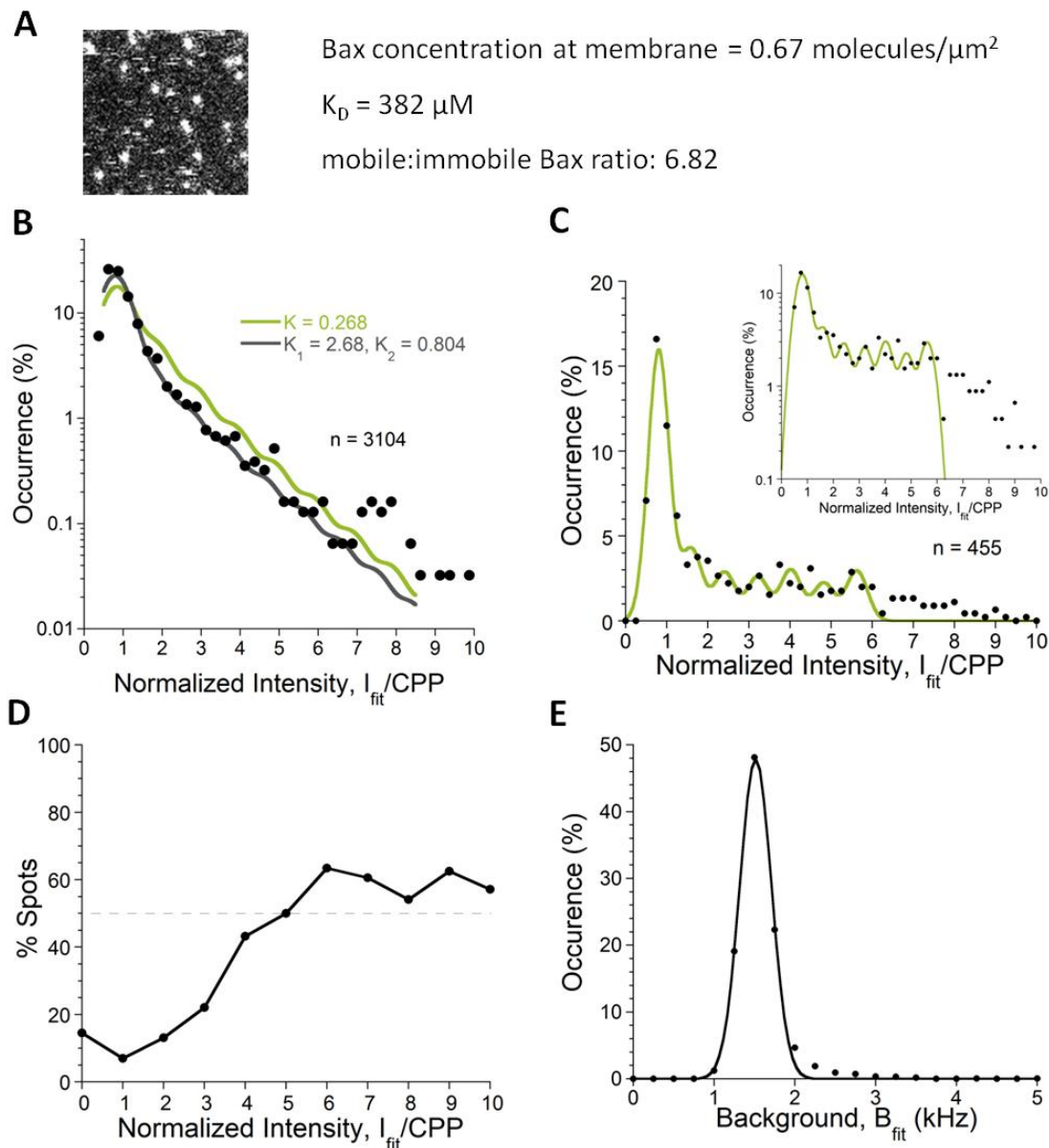
Bcl-XL the concentration of cBid at the membrane was greatly increased to 11.6 molecules/ $\mu\text{m}^2$ . Such a high membrane concentration exceeds the theoretical concentration to resolve single molecules, 2.82 molecules/ $\mu\text{m}^2$  (see Methods 2.11.2). In this regard, the cBid + Bcl-XL data must be interpreted with caution (see Discussion 5.5). Still, robust observations were the amount of protein at the membrane, and the overall ratio of mobile to immobile cBid, irrespective of normalized intensity, calculated from the total number of streaks and spots detected in confocal images (Table 8). As is the case with the relative size of cBid complexes, the data suggests that the distribution between mobile and immobile cBid is altered based the presence of a binding partner. cBid alone showed an intermediate ratio of 3.1 mobile:immobile Bid, compared to 6.3 in the presence of Bax, and 1.9 in the presence of Bcl-XL. Thus, Bax promotes cBid mobility at the membrane, while Bcl-XL inhibits it. The dissociation constants in Table 8 are for

cBid binding to SLBs calculated by Eq. 23. The presence of Bax and Bcl-XL appears to promote cBid binding to SLBs judging by the lower  $K_D$ s compared to cBid alone.

#### *4.8 Quantification Bax binding to supported bilayers*

HiLyte488-Bax binding to SLBs was visualized by confocal imaging and automated image analysis was performed to quantify images. Prior to imaging, fluorescent Bax remaining in solution was washed away with buffer to accurately locate the plane of the membrane. It appeared that most of the Bax added in solution did not bind the membrane after 2 hours incubation judging by the low measured concentration of protein at the membrane ( $0.67$  Bax molecules/ $\mu\text{m}^2$ ), although a concentration of  $2\text{nM}$  Bax was added in solution (in comparison,  $400$  pM Atto647-cBid added in solution resulted in a cBid membrane concentration of  $2.7$  molecules/ $\mu\text{m}^2$ ). As with data for cBid binding to SLBs, normalized intensity data refers to the relative fluorescence intensity of Bax oligomers. The mobile Bax at the plane of the membrane appears to be primarily monomeric with some larger complexes (Figure 22B). The data was fit with Eqs. 18 and 19 to produce  $K_D$  values for Bax oligomerization.

A model which assumed two constants for Bax oligomer formation (Eq. 19, black curve in Figure 22B) proved to fit the data better than a model which assumed only one constant (Eq. 18, green curve in Figure 22B). Interestingly, for the former model, the dissociation constant for dimer formation ( $K_1$ ) was greater than the constant for the formation of larger oligomers ( $K_2$ ), which means once a dimer is formed, forming larger oligomers becomes easier. This suggests there is a degree of cooperativity in Bax oligomerization. Surprisingly, the distribution of immobile Bax complexes (spots)



**Figure 22: Characterizing Bax binding to supported bilayers.** (A) Representative  $10 \times 10 \mu\text{m}$  image of 2 nM HiLyte488-Bax in the presence of 400 pM WT cBid at the plane of the membrane. The CPP for monomeric Bax measured by FIDA was 5.1 kHz. The concentration of Bax at the membrane was calculated by Eq. 21 from fluorescence intensity at the plane of the membrane. A  $K_D$  for Bax binding to SLBs was calculated from Eq. 23. The ratio of mobile to immobile Bax was 6.82. (B) Distribution of mobile Bax (streaks) at the membrane. Circles are experimental data and solid lines are probability distribution fits. A Bax dissociation constant was calculated using either assuming one constant for oligomer formation (Eq. 18, green curve) or one constant for dimer formation and one for all other oligomer formation (Eq. 19, black curve). (C) Distribution of immobile Bax (spots) at the membrane. Black circles are experimental data and solid lines are fits using Eq. 20 with 7 Gaussian peaks. The inset plot is the same data plotted on a log scale. (D) The ratio of mobile (streaks) to immobile (spots) Bax as a function of normalized intensity. (E) Distribution of fit obtained values background ( $B_{fit}$ ) for the data in (B) and (C). Line is a Gaussian fit to the data.

was similar to mobile Bax data (Figure 22C), where it appears that most immobile Bax is monomeric. Some larger complexes were observed, particularly in the normalized intensity range of 2-6 (Figure 22C, inset). Although monomeric Bax was the predominant mobile and immobile species detected, the number of immobile Bax monomers as percentage of all monomers detected was low (Figure 22C) indicating that monomeric Bax has a tendency to be mobile. Approximately equal amounts of mobile and immobile Bax were present at a normalized intensity value of 5 and greater. This suggests that Bax oligomers are more likely than monomers to be immobile, presumably because part of the oligomer is inserted in the SLB lower leaflet. Overall, the mobile-to-immobile Bax ratio, regardless of normalized intensity, was 6.82. A Gaussian distribution of background levels ( $B_{fit}$ ) was seen for all data in Figure 22B-C, and centered at a very low value, ~1 kHz (Figure 22E).

## **5 Discussion and Conclusions**

### *5.1 Protein labelling and photostability*

A critical requirement for single molecule experiments is that protein labelling efficiently is sufficiently high so that the amount membrane bound protein can be quantified with accuracy. Obtaining dye labelled Bax with a high degree of labelling proved difficult and extensive optimization of the labelling protocol was done. Considering the results of Bax labelling experiments summarized in Table 5, two factors appeared to contribute to the degree of labelling: dye size and charge. Smaller dyes (low molecular weight) resulted in higher degree of labelling when compared to larger dye molecules under the same conditions (compare Table 5, trial 2 to trials 3, 8 and 13). This effect is likely due to smaller dyes being able to more easily access the labelling sites with less steric hindrance. The second contributing factor is the charge of the dye at the pH used in labelling reactions. Charged dyes may be repulsed by electrostatic interaction with charged residues adjacent to the labelling site. Under standard labelling conditions HiLyte488, an uncharged and relatively small dye, resulted in a higher degree of labelling than the Alexa and Atto dyes tried (compare Table 5, trial 19 to trial 3, 8 and 13). Though 70% and 81% labelling efficiency was obtained for Atto647-cBid and HiLyte488-Bax respectively, ideally a higher degree of labelling is desired (although it may not be possible to achieve higher labelling using reactive dyes). Alternatively, fluorescent fusion proteins (e.g. eGFP-Bax) can be used to achieve 100% labelling, since the fluorophore and protein of interest are expressed as a fusion product. However there are associated artefacts with fusion proteins (see section 5.2). In vitro transcription and translation using

modified aminoacyl-tRNAs is another method to achieve a high degree of labelling. Using this technique, single dye molecules (covalently attached to amino acids, usually lysine or cysteine) are incorporated into proteins as they are synthesized *in vitro*, thereby resulting in very high (>90%) labelling efficiency. Thus this could be a method to improve the labelling efficiency.

Single molecule experiments also require bright, photostable dyes. The Alexa Fluor dyes are recognized as standards in this respect. The HiLyte and Atto dyes used to label the proteins in the presented experiments have molecular brightness comparable to their Alexa counterparts (Figure 14A, E). Alexa- and Atto647 dyes share similar photophysical properties in terms of quantum yield, extinction coefficient as well as similar absorption and emission peak wavelengths according to the manufactures' specifications. While Atto647 appeared to have a marginally shorter photobleaching lifetime ( $\tau_p$ ) and therefore be slightly more prone to photobleaching than Alexa647, Atto647 also retained a higher normalized specific brightness at low scan speed than that of Alexa647 (Figure 14D). Collectively, the data demonstrates that the fluorescence properties of Atto647 are comparable to that of Alexa647 and suitable for single molecule experiments.

HiLyte488 showed a drastic decrease in diffusion time with increased laser power (Figure 14F) suggesting it is prone to photobleaching. Indeed, this is also borne out in the calculated photobleaching lifetime  $\tau_p = 2.3$  ms at a laser power of 250  $\mu$ W which is relatively short (Figure 14H). In contrast, Alexa488 was very photostable and maintained a high molecular brightness at all scan speeds, though it must be taken into consideration

that Alexa 488 was the free dye whereas HiLyte488-Bax was a labelled protein. Since high Bax labelling efficiency was only possible with HiLyte488, conditions were used to limit photobleaching by using low laser power (5  $\mu$ W) for FCS/FIDA measurements and confocal imaging of HiLyte488-Bax. In addition, accurate determination of HiLyte488-Bax specific brightness and concentration can be made if the pixel dwell time for imaging (1 ms) was lower than photobleaching time (2.3 ms at  $p=250 \mu$ W, so  $\sim 100$  ms at  $P=5 \mu$ W used for imaging). In the future, antibleaching reagents (e.g. ascorbic acid) may also be used to alleviate the effects of poor HiLyte488 photostability.

### *5.2 Fluorescent protein membrane binding and pore forming activity*

The ability of fluorescently labelled single cysteine mutants to retain their WT activity was assessed by the ANTS pore forming assay (Figure 5). Compared to WT cBid, Atto647-cBid appeared to be enhanced in activating WT Bax and HiLyte488-Bax resulting in higher ANTS release. It may be that the positive charge carried by Atto647 on labelled cBid increases its affinity for the negatively charged MOM-like liposomes. Labelling cBid may also facilitate the conformational changes that occur during separation of the p7 and p15 fragments and tBid membrane binding.

For initial experiments assessing fluorescent Bax binding to liposomes, the eGFP-Bax fusion protein was used. This construct displays approximately 40-50% pore forming activity of WT Bax. Interestingly, Bax membrane targeting assessed by Western blot indicated that WT Bax and eGFP-Bax bind membranes to the same extent across all protein-to-liposome ratios (Figure 6). Thus, inhibition of eGFP-Bax pore formation must occur at the oligomerization step downstream of membrane binding. Considering the

eGFP-Bax construct is an N-terminal fusion of a 36kDa eGFP monomer to 22 kDa Bax this is not unexpected. When Bax binds membranes, the N-terminal region remains above the bilayer, thus having a large fusion to the N-terminal may hinder the association of membrane bound Bax monomers during oligomerization. When eGFP-Bax binding to planar membranes was assessed by confocal imaging, very little Bax was observed at the plane of the membrane (after washing away protein in solution) even when using a high concentration of 100 nM eGFP-Bax (data not shown). In contrast HiLyte488-Bax displayed approximately 60-70% of WT Bax pore forming ability in the ANTS assay (Figure 5). 2nM HiLyte488-Bax was able to bind SLBs in the presence of cBid to a greater extent than 100 nM eGFP-Bax. It must be noted there is no functional assay for pore formation in SLBs analogous to ANTS release. It was assumed that Bax pore forming activity seen in mitochondria-like liposomes would translate to mitochondria-like SLBs as well. However, the requirement for activation by cBid for Bax binding could be assessed in the SLB system.

Prior to assessing Bax binding to SLBs, the binding of Atto647-tBid and Atto647-cBid to SLBs was observed. Atto647-tBid bound non-specifically to the mica surface in the absence of a planar membrane (data not shown), thus Atto647-cBid was used for subsequent experiments. cBid is also a more biologically relevant form of Bid which dissociates into tBid + p7 fragment when in close proximity to the membrane. In Figure 15, although the membrane is saturated with cBid by 2 minutes, cBid remaining in solution may still interact with the membrane causing separation of the two cBid fragments and resulting in the generation of tBid. tBid has been observed to “stick” non-



specifically to surfaces and this could be the cause of the observed decrease in the signal in solution (Figure 15C green curve decrease in solution over time).

HiLyte488-Bax binding to SLBs was observed in the absence or presence of cBid (Figure 16). In the absence of cBid, a small amount of HiLyte488-Bax appeared at the plane of the membrane, possibly suggesting some Bax was autoactive in the absence of cBid. In cells, it has been observed that a population of Bax is always loosely associated with mitochondria even when apoptosis is not initiated (Antonsson et al, 2001). Confocal imaging does not offer sufficient resolution to determine whether the Bax localized to the membrane in the absence of cBid is loosely associated or fully membrane bound. The very low signal that was observed at the membrane in the absence of cBid could also be background fluorescence from the mica. In Figure 16C, in the presence of cBid, HiLyte488-Bax signal at the membrane was increased. Thus it can be said cBid promotes Bax binding to SLBs.

### *5.3 Bax binding to liposomes measured by complimentary techniques*

eGFP-Bax binding to mitochondria-like liposomes was measured by Western blot, FCS and FIDA. The three methods were in general agreement that eGFP-Bax binding to liposomes saturates at high Bax-to-liposome ratios,  $r$  (Figure 7C). This was a robust observation also seen by small angle neutron scattering experiments at much higher protein and lipid concentrations (but the same relative protein-to-lipid ratios) (Satsoura et al, 2012). The absolute values for the amount of Bax bound to liposomes at a given  $r$  obtained from each method differ due to assumptions of how the amounts of soluble and membrane bound protein are calculated.

Immunoblotting requires that membrane bound and soluble proteins are separated by gel filtration. Gel filtration is limited in that it cannot distinguish between proteins that are inserted in the liposome membrane and proteins that are peripherally or loosely bound to the liposome. Loosely bound protein may or may not unbind from liposomes during gel filtration and additionally there may be a pool of inactive Bax that remains on the column which may account for the variability in blotting results. Although efforts were made to work within the linear response range of the technique, the amount of eGFP-Bax bound to liposomes quantified from immunoblots for a given  $r$  showed large variation from experiment-to-experiment (between 50-80% at  $r=1$  and between 0-20% at  $r=50$ ).

Alternatively, fluorescence fluctuation methods performed in solution can detect all membrane associated protein, whether fully inserted into the membrane or peripherally bound. Although these techniques can not differentiate between full membrane bound and peripherally associated protein, they are more sensitive in detecting small amounts of protein. As is the case with Western blot results, the saturation of eGFP-Bax binding at high  $r$  values was a robust observation seen by both FCS and FIDA methods (Figure 7C). With FIDA, the distinction between the two populations of membrane bound and soluble eGFP-Bax is made based on difference in molecular brightness. Unbound proteins have brightness equal to that of a single eGFP fluorophore, while liposomes with bound protein have brightness greater than a single eGFP. FIDA values mirror Western blotting results only at high  $r$  when there are multiple Bax molecules bound per liposome. This reflects the bias in the FIDA method which cannot differentiate between a soluble eGFP-Bax monomer and a single membrane bound eGFP-Bax (see Materials 2.8.6).

With FCS, the distinction between membrane bound and soluble protein is made by the difference in diffusion times. Soluble protein had a diffusion time in the focal volume 10-fold lower and has a diffusion coefficient 10-fold higher than protein bound to liposomes (Figure 7A). FCS has the necessary sensitivity to assess whether any Bax may remain transiently bound to liposomes in the absence of tBid as long as the interaction lasts more than a few milliseconds. Using FCS, the total eGFP-Bax associated with liposomes in the absence of tBid was always less than 5% at  $r=1$  (Figure 7B). A small amount of Bax is always thought to be associated with membranes since, it has been shown that in normal cells, a small amount of Bax is always loosely associated with the mitochondrial membrane and is carbonate extractable (Antonsson et al 2001). FCS values mirrored Western blot data only at low  $r$  values, reflecting the bias that FCS can only accurately differentiate between membrane bound and soluble Bax when there is one or less Bax molecule bound per vesicle (see Methods 2.8.5).

#### *5.4 Validating the mitochondria-like supported lipid bilayer system*

The method of vesicle fusion using SUVs has been shown to produce single planar bilayers, and has been well characterized by AFM (Reviakine et al, 2000; Richter et al 2005; Chiantia et al, 2006), neutron scattering (Armstrong et al, 2010) and ellipsometry (Benes et al, 2002; Richter et al 2005). Although the lamellarity of the planar membrane cannot easily be assessed by confocal microscopy, the measured 2-fold difference in the brightness per unit area in the planar membrane and vesicles suggests the planar membrane is a single bilayer once photobleaching and the position of the confocal volume relative to the plane of the membrane are accounted for. Additionally, it is

hypothesized that the same interactions that allow mica to be an effective substrate for vesicle fusion, are also responsible for slowing down lipid diffusion, particularly in the lower leaflet that directly interacts with the substrate surface. Therefore lipids in the lower leaflet are more prone to photobleaching than lipids in the top leaflet and this may also contribute to the observed 2-fold deficit in brightness per area in SLBs.

It has been previously reported that lipid diffusion in SLBs is slower than in free-standing membranes (Garcia-Saez & Schwille, 2008; Przybylo et al, 2006). Surprisingly when lipid diffusion in the plane of the membrane was measured by FCS, the resulting diffusion coefficients for dye labelled PE and the membrane tracer DiO were somewhat higher than previously seen for the same probes under similar conditions (Table 2). It must be noted that in the studies performed by Chiantia et al (2006) and Huang et al (1992) the planar membranes contained cholesterol up to 20% which has the effect of shifting membrane dynamics to the liquid ordered state in which diffusion is slowed. Although it was possible to measure diffusion coefficients with a high degree of reproducibility (low standard deviation) the same measurements did not yield a value for the number of particles in the focal volume (N) and molecular brightness (CPP) with any certainty (Table 7). This was particularly true for the NBD-PE probe. It has been previously reported that NBD is not ideal for single molecule experiments due to its relatively low quantum yield and molecular brightness, although this is especially true in aqueous buffer (Benes et al, 2002). Furthermore, to measure diffusion by FCS, the focal volume must remain stationary in the sample for the duration of the measurement. Consequently, photobleaching in the region of the beam is more likely to occur in the

absence of beam scanning which would result in higher than expected diffusion coefficients. Thus, the measured diffusion coefficients were likely influenced by photobleaching of probes as they diffused through the focal volume and therefore appear faster than they are in reality. Still the fluid properties observed for the mitochondria-like SLBs were encouraging.

As final validation of the mitochondria-like SLB system, the ability of Bcl-2 proteins to bind the membrane was observed by confocal imaging. cBid is able to bind mitochondria-like liposomes with high affinity and recruit Bax to bind and permeabilize membranes (Lovell et al 2008). Here, it was found the fluorescently labeled Atto647-cBid was able to bind the mitochondria-like planar membrane with specificity (Figure 15). Fluorescent HiLyte488-Bax, too, was able to bind the SLB in the presence of cBid (Figure 16).

### *5.5 Characterization of cBid binding to supported bilayers*

The protein-protein and protein-membrane interactions of Bcl-2 proteins have been extensively characterized using ensemble techniques in cells and in vitro systems such as isolated mitochondria and liposomes. In this thesis, a novel approach was used to characterize the binding of fluorescent cBid and Bax to mitochondria-like SLBs with single molecule resolution. cBid binding to SLBs occurred with a high degree of specificity and fast kinetics (Figure 15). This reflects the data for tBid binding to liposomes, which too occurs rapidly (Lovell et al, 2008) and results in almost all tBid targeting to liposomal membranes (Billen et al, 2008). Certain considerations were made (see Methods 2.11) to ensure that single molecules could be resolved and that the

intensity of protein complexes on the membrane could be accurately quantified. In general, experiments with labelled cBid showed a higher level of background than experiments with labelled Bax (compare Figure 21D and Figure 22E). Experiments with Atto647-cBid contained the 488 nm excitable membrane tracer DiO, while experiments with HiLyte488-Bax contained the 647 nm excitable membrane tracer DiD. The membrane dyes were present to ensure that SLBs formed free of defects. DiO bleed through into the red cBid channel resulted in a background signal of ~30 kHz and likely caused the higher levels of background seen in cBid experiments. Whereas, there was no bleedthrough of DiD into the Bax channel.

In experiments where cBid was incubated with Bcl-XL, the surface concentration of cBid was approximately 4 times the concentration at which single cBid molecules could be resolved. In this case, there is not sufficient spatial separation of single molecules on the membrane to accurately detect and quantify intensity data by the Gaussian fitting method employed. As a result, the total number of objects with a Gaussian profile detected in the presence of Bcl-XL was significantly lower than in other experiments (compare n values in Figure 21A, B) and a much higher background than in the absence of Bcl-XL (Figure 21D). Using 4-fold lower cBid concentration in future experiments should allow for adequate separation of molecules on the membrane to accurately detect and quantify data. For the moment, the shift to larger relative cBid complex sizes in the presence of Bcl-XL must be interpreted with caution as this may be the result of failing to detect complexes with a lower intensity not sufficiently above the background, or failure to detect individual molecules due to inadequate spatial separation.

Still, some conclusions can be made by analyzing the size of cBid complexes formed in the presence of different Bcl-2 binding partners and the amounts of mobile and immobile protein that is present at the membrane.

When cBid alone was incubated with SLBs, the predominant mobile species appears to be monomers and the predominant immobile species is the trimer (Figure 21). If one considers the partial cBid labelling efficiency was 71%, this immobile species may be closer to a tetramer. The formation of tBid homotrimers has been previously observed in cells (Grinberg et al, 2002), thus this may represent a preferred oligomer size for Bid in the absence of binding partners. A  $K_D$  of 0.351 molecules/ $\mu\text{m}^2$  was calculated assuming a single dissociation constant for cBid oligomer formation and resulted in a good fit of the experimental data (Figure 21A). It is possible that the populations of mobile and immobile cBid correspond to two distinct forms of membrane bound cBid. It has been reported that helices 6, 7 and 8 of Bid insert into membranes upon binding (Oh et al, 2005). Thus, immobile cBid which appears as diffraction limited spot may correspond to cBid in this form with helices 6, 7 and 8 embedded in the membrane rooting it in place. However, none of these helices are thought to completely span the entire membrane. As such, mobile cBid may represent a loosely membrane associated form of Bid with certain helices peripherally bound to the bilayer. This distinction between membrane inserted and loosely associated cBid may not be apparent using ensemble techniques, but can be easily seen as immobile spots and mobile streaks by confocal imaging under single molecule conditions.

Bid is an unusual Bcl-2 protein since it is capable of causing membrane insertion, and activation, of both pro-apoptotic Bax and anti-apoptotic Bcl-XL. Interestingly, when considering the  $K_D$  for cBid binding to SLBs, the presence of a Bcl-2 binding partner appears to increase cBid binding affinity (Table 8). In addition, the presence of Bax or Bcl-XL appears to cause a shift to smaller or larger cBid complexes, respectively. This effect is also apparent when considering the  $K_D$  for cBid complex formation in the presence of either Bax or Bcl-XL (Figure 21A). A corresponding shift in the distribution of mobile and immobile cBid complexes is also seen. With Bax, cBid complexes irrespective of size appear to be more mobile whereas with Bcl-XL the opposite is true. A similar trend is observed when insertion of cBid into liposome membranes is measured by change in NBD fluorescence (Shamas-Din, unpublished data). In the presence of Bax, NBD-cBid appears to be less membrane inserted indicated by a decrease in NBD fluorescence. In the presence of Bcl-XL, the NBD fluorescence increased suggesting cBid is embedded deeper in liposomal membranes. Collectively, the data suggests a mechanism by which cBid is capable of regulating apoptosis by altering its propensity for activating either Bax or Bcl-XL. In liposomes, cBid is able to recruit approximately 3.5-fold molar excess of Bax or 4-fold molar excess of Bcl-XL to bind membranes (Billen et al, 2008). Thus, Bid can be considered catalytic to the function of both Bax and Bcl-XL. The molar excess of Bcl-XL recruited to membranes can sequester any membrane bound cBid as well as activated Bax at the membrane thereby preventing Bax oligomerization (Billen et al, 2008). The shift towards larger and more immobile cBid complexes in the presence of Bcl-XL supports this. If cBid forms large homo-complexes, it is unlikely to



bind and activate Bax. Conversely, in the presence of Bax, a shift to smaller complexes of more mobile cBid can promote Bax activation by increasing the amount of monomeric cBid molecules available to activate Bax. Increased mobility of cBid provides a means of propagating the pro-apoptotic signal by activating Bax at multiple sites.

### *5.6 Characterization of Bax binding to SLBs*

HiLyte488-Bax binding to SLBs in the presence of 400 pM cBid occurred slowly and a large amount of Bax remained in solution after the 2 hour incubation period. To accurately locate the plane of the membrane, fluorescent Bax remaining in solution following the two hour incubation period was washed away with buffer. After washing, an apparent  $K_D$  of 382  $\mu\text{M}$  (association constant of  $0.00263 \mu\text{M}^{-1}$ ) for Bax binding to SLBs was calculated. This is consistent with cBid binding to SLBs with a higher affinity than Bax, as is the case with these proteins binding to liposomes. Considering the association constant in Figure 8A (orange curve, for samples prior to gel filtration) Bax is able to bind liposomal membranes with approximately 40-fold higher affinity than SLBs. Membrane curvature may play a role in binding affinity. Bax binds to 50 nm liposomes with slightly higher affinity than 100 nm liposomes (compare  $K_A$  values in Figure 9A). 50 nm liposomes have a higher membrane curvature than 100 nm liposomes, thus it follows Bax would bind even less to SLBs which have no curvature. It may be that the low protein concentrations required for single molecule detection are not sufficient for cBid to activate Bax to bind SLBs. Using intermolecular FRET in liposomes, Lovell et al reported an apparent  $K_D$  of ~20 nM for the binding interaction between tBid and Bax which is many times the concentration of protein used in SLB binding experiments.

Another issue affecting Bax binding is saturation of binding sites in SLBs. To accommodate protein binding, liposomes can increase in size. Consistent with this, insertion of Bax in liposomes was found to result in thinning of the membrane bilayer (Satsoura et al, 2012). In a SLB, lipids are constrained in a 2D plane, and the insertion of protein will cause an increase in the packing density and surface pressure of lipid in the membrane over time. Thus it is not surprising that Bax binding to SLBs saturates at lower protein-to-lipid ratios than seen in liposomes.

An unexpected finding was that the amount of monomeric Bax at the membrane (either mobile or immobile) greatly exceeded oligomeric Bax. Previously, it has been observed that Bax activated by detergent below the critical micelle concentration exists as membrane bound monomers (Bleicken et al, 2010; Ivashyna et al, 2009) and Bax is thought to bind to membranes as a monomer prior to oligomerization (Annis et al, 2005). Still, in the ANTS pore forming assay, endpoint is reached after 2 hours and Bax membrane permeabilization activity is dose-dependent (Figure 10) suggesting an equilibrium state of Bax pores by 2 hours. Similar results have been shown for Bax oligomerization measured by FRET which appears to be complete by 30 minutes (Lovell et al, 2008). However, the concentrations of Bax and Bid used in the ANTS and FRET assays were many times greater than the concentrations of protein used in SLB binding experiments. Considering this, it is likely that at low protein concentration most membrane bound Bax may not be part of an oligomeric pore (i.e. monomeric) as observed here. Detergent activated Bax was shown to create large openings in planar membranes when measured by AFM, with possibly hundreds of Bax per pore (Epanand et al, 2002;

Kuwana et al, 2002). Here, the Bax complexes that were observed on SLBs did not surpass the size of decamers. There is evidence for relatively small functional Bax pores. It has been shown that a tetramer size pore is sufficient to cause the release of cytochrome C from liposomes (Saito et al, 2000). Also, formation of just a single Bax pore in 200 nm GUVs resulted in rapid release of encapsulated fluorophores finishing within 30 ms after pore formation (Schlesinger & Saito, 2006).

For mobile Bax complexes at the plane of the membrane, 2 models were applied assuming one or two dissociation constants for Bax oligomer formation respectively. In Figure 22B, it can be seen that the model assuming one constant for the formation of dimers ( $K_1$ ) and a second constant for the formation of all higher order oligomers ( $K_2$ ) is a better fit to the experimental data than assuming a single dissociation constant. The asymmetric model for Bax oligomerization would predict a single binding constant for oligomer formation since Bax monomers are added to a growing chain. The data for Bax binding to SLBs is contrary to this; still it cannot be said with certainty that the presence of 2 binding constants is proof of symmetric Bax oligomerization. If Bax oligomerization followed the symmetric model, then the relative Bax complex intensity (normalized intensity in Figure 22C) would in principle increase in increments of dimers. This is not the case for immobile Bax at the plane of the membrane where the relative intensity of Bax complexes increases in increments of monomers (Figure 22C). However, the intermediate values observed may result from less than 100% Bax labelling efficiency and photobleaching. Therefore to confirm whether Bax oligomers grow with the addition of monomers or dimers, a higher degree of labelling is required. In liposomes, Bax

binding and pore formation was found to be cooperative (Saito et al, 2000). The presence of two binding constants does suggest a degree of cooperativity in Bax binding once a Bax dimer is formed since  $K_2$  is lower than  $K_1$ . This is supported by the normalized intensity data for immobile Bax at the membrane. In Figure 22C, while the majority of immobile Bax appears to be monomeric, there are almost equal numbers of oligomers with a relative size of 3, 4, 5 and 6 subunits again reflecting cooperativity in binding once a dimer is formed.

As proposed for cBid binding to SLBs, the two populations of mobile and immobile Bax may correspond to fully membrane inserted and loosely associated protein, respectively. In contrast to cBid, Bax membrane inserting helices are thought to span the entire membrane. Thus it is possible that Bax monomers may be mobile until Bax oligomerization results in a conformational change causing Bax oligomers to become immobile. Therefore is it surprising that in addition to most of the immobile Bax being monomeric, some large mobile Bax complexes were observed. Alternatively, it may be possible for larger complexes to become mobile as subunits are added. Since there is no functional assay for Bax pore formation in planar membranes as yet, it is difficult to determine whether Bax binding and oligomerization in planar membranes occurs in the same manner as it does in liposomes and mitochondria.

### *5.7 Future Directions*

While the data presented in this thesis strongly suggests the formation of cBid and Bax oligomers in SLBs, confocal imaging lacks the specificity to confirm a direct interaction between single molecules due to diffraction limited resolution. A SLB system

offers a platform to characterize direct interactions between single proteins using a method such as FRET. Alternatively, mutations that inhibit oligomerization of Bax and cBid, but not membrane binding, can be introduced to see if a shift towards monomeric proteins and the loss of higher order complexes occurs. In the absence of these mutations, the formation of higher order complexes would suggest direct interactions leading to oligomer formation. It is also possible to measure interactions by fluorescence crosscorrelation spectroscopy (FCCS), in which two proteins are labelled with dyes of different colour. Such an experiment can provide insight into the unanswered question as to whether cBid remains associated with Bax (possibly as part of a pore) following the initial interaction that causes Bax membrane binding.

The conformational changes that accompany protein binding to SLBs can also be investigated with single molecule resolution to gain further insight into the molecular mechanisms regulating Bcl-2 protein function in apoptosis. Crucially, this requires a suitable fluorophore whose fluorescence emission is altered by the conformational change. In addition, lipidic quenchers can be incorporated into the SLB to assess the degree of insertion of the helices 5, 6, and 9 in Bax (or helices 6, 7 and 8 in cBid) upon membrane binding, when those regions are labelled with a fluorescent dye. A final consideration is the need for a functional pore forming assay in a SLB system. Methods measuring current fluctuations or the loss of membrane potential as indications of membrane permeabilization still cannot directly determine the size of pores in the way that leakage assays in liposome systems can. By using a tethered supported bilayer system, or by forming a membrane on a surface with pores, the membrane can divide two

aqueous spaces which can be amenable to leakage assays by trapping particles in one space and observing their diffusion across the membrane if pores are formed. It may also be possible to implement AFM on SLBs to gain a topographical view of membrane bound protein complexes and determine a pore size this way.

## 6 References

- Annis, M. G., Soucie, E. L., Dlugosz, P. J., Cruz-Aguado, J. A., Penn, L. Z., Leber, B. & Andrews, D.W. Bax forms multispinning monomers that oligomerize to permeabilize membranes during apoptosis. *EMBO J.* **2005**; 24: 2096-2103
- Antonsson, B. & Martinou, J.C. The Bcl-2 Protein Family. *Exp Cell Res.* **2000**; 256: 50-57
- Antonsson, B., Montessuit, S., Lauper, S., Eskes, R & Martinou, J.C. Bax oligomerization is required for channel-forming activity in liposomes and to trigger cytochrome c release from mitochondria. *Biochem J.* **2000**; 345:271-278.
- Antonsson, B., Montessuit, S., Sanchez, B., & Martinou, J. C. Bax is present as a high molecular weight oligomer/complex in the mitochondrial membrane of apoptotic cells. *J Biol Chem.* **2001**; 276(15): 11615-11623
- Armstrong, C.L., Kaye, M.D., Zamponi, M., Mamontov, E., Tyagi, M., Jenkins, T. & Rheinstadter, M.C. Diffusion in single supported lipid bilayers studied by quasi-elastic neutron scattering. *Soft Matter.* **2010**; 6, 5864-5867.
- Basañez G., Sharpe J.C., Galanis J., Brandt T.B., Hardwick J.M. & Zimmerberg J. Bax-type apoptotic proteins porate pure lipid bilayers through a mechanism sensitive to intrinsic monolayer curvature. *J Biol Chem.* **2002**; 277(51): 49360-49365
- Benes, M., Billy, D., Hermens, W.T. & Hof, M. Muscovite (Mica) Allows the Characterisation of Supported Bilayers by Ellipsometry and Confocal Fluorescence Correlation Spectroscopy. *Biol Chem.* **2002**; 383: 337-341
- Ben-Tal, N., Honig, B., Peitzsch, R.M., Denisov, G. & McLaughlin, S. Binding of small basic peptides to membranes containing acidic lipids: theoretical models and 1490 experimental results. *Biophys. J.* **1996**; 71: 561–575
- Billen, L.P., Kokoski, C.L., Lovell, J.F., Leber, B. & Andrews, D.W. Bcl-XL Inhibits Membrane Permeabilization by Competing with Bax. *PLOS Biol.* **2008**; 6(6): e147
- Billen, L.P., Shamas-Din, A. & Andrews, D.W. Bid: a Bax-like BH3 protein. *Oncogene.* **2009**; 27: S93-S104
- Bleicken, S., Classen, M., Padmavathi, P.V., Ishikawa, T., Zeth, K., Steinhoff, H.J. & Bordignon, E. Molecular Details of Bax activation, oligomerization and membrane insertion. *J Biol Chem.* **2010**; 285(9): 6636-6647

- Boatright, K.M. & Salvesen, G.S. Mechanisms of caspase activation. *Curr Opin Cell Biol.* **2003**; 15:725-731
- Bogner, C., Leber, B. & Andrews, D.W. Apoptosis: embedded in membranes. *Curr Opin Cell Biol.* **2010**; 22:1-7
- Chiantia, S., Ries, J., Kahya, N., Schwille, P. Combining AFM and Two-Focus SFCS Study of Raft-Exhibiting Model Membranes. *ChemPhysChem.* **2006**; 7: 2409-2418.
- Chen, L., Willis, S.N., Wei, A., Smith, B.J., Fletcher, J.I., Hinds, M.G., Colman, P.M., Day, C.L., Adams, J.M. & Huang, D.C. Differential targeting of prosurvival Bcl-2 proteins by their BH3-only ligands allows complementary apoptotic function. *Mol Cell.* **2005**; 17: 393–403
- Certo, M., Del Gaizo Moore, V., Nishino, M., Wei, G., Korsmeyer, S., Armstrong, S.A. & Letai, A. Mitochondria primer by death signals determine cellular addiction to antiapoptotic BCL-2 family members. *Cancer Cell.* **2006**; 9: 351-365
- Chipuk, J.E., Fisher, J.C., Dillon, C.P., Kriwacki, R.W., Kuwana, T. & Green, D.R. Mechanism of apoptosis induction by inhibition of the anti-apoptotic BCL-2 proteins. *Proc Natl Acad Sci USA.* **2008**; 105(51): 20327-32
- Chipuk, J.E., Moldoveanu, T., Llambi, F., Parsons, M.J. & Green, D.R. The BCL-2 family reunion. *Mol Cell.* **2010**; 37: 299-310
- Cotter, T.G. Apoptosis and cancer: the genesis of a research field. *Nat Rev Cancer.* **2009**; 9: 501-507
- Cremer, P.S., Boxer, S.G. Formation and Spreading of Lipid Bilayers on Planar Glass Supports. *J Phys Chem Biol.* **1999**; 103: 2553-2559
- Davis, L.M., Shen, G. & Ball, D.A. Multiphoton Microscopy in the Biomedical Sciences V: “Saturation effects in fluorescence correlation spectroscopy.” ed. Periasamy, A. SPIE, Bellingham, Washington. **2005**
- Desagher, S., Osen-Sand, A., Nichols, A., Eskes, R., Montessuit, S., Lauper, S., Maundrell, K., Antonsson, B. & Martinou, J.C. Bid-induced conformational change of Bax is responsible for mitochondrial cytochrome c release during apoptosis. *J Cell Biol.* **1999**; 144: 891-901



- Edinger, A.L. & Thompson, C.B. Death by design: apoptosis, necrosis and autophagy. *Curr Opin Cell Biol.* **2004**; 16: 663-669
- Epand, R.F, Martinou, J.C., Montessuit, S., Epand, R.M. & Yip, C.M. Direct evidence for membrane pore formation by the apoptotic protein Bax. *Biochem Biophys Res Comm.* **2002**; 298: 744-749
- Eskes, R., Desagher, S., Antonsson, B. & Martinou, J.C. Bid induces the oligomerization and insertion of Bax into the outer mitochondrial membrane. *Mol Cell Biol.* **2000**; 20(3): 929-35
- Fuertes, G., García-Sáez, A.J., Esteban-Martín, S., Giménez, D., Sánchez-Muñoz, O.L., Schwille, P. & Salgado, J. Pores Formed by Bax $\alpha$ 5 Relax to a Smaller Size and Keep at Equilibrium. *Biophys. J.* **2000**; 99(9): 2917-2925
- Garcia-Saez, A.J. & Schwille, P. Fluorescence Correlation Spectroscopy for the study of membrane dynamics and protein/lipid interactions. *Methods.* **2008**; 46: 116-122
- García-Sáez, A.J., Ries, J., Orzáez, M., Pérez-Payà, E. & Schwille, P. Membrane promotes tBid interacton with Bcl-XL. *Nature Struc Mol Biol.* **2009**; 16(11): 1178-1186
- Ghibelli, L. & Diederich, M. Multistep and multitask Bax activation. *Mitochondrion.* **2010**; 10(6): 604-613
- Gavathiotis, E., Suzuki, M., Davis, M.L., Pitter, K., Bird, G.H., Katz, S.G., Tu, H.C., Kim, H., Cheng, E.H., Tjandra, N. & Walensky, L.D. BAX activation is initiated at a novel interaction site. *Nature.* **2008**; 455: 1076-1081.
- Gavathiotis, E., Reyna, D.E., Davis, M.L., Bird, G.H. & Walensky, L.D. BH3-triggered structural reorganization drives the activation of proapoptotic BAX. *Mol Cell.* **2010**; 40(3): 481-92
- Grant Jr.,E., Beeler, T.J., Taylor, K.M., Gable, K.& Roseman, M.A. Mechanism of magainin 2a induced permeabilization of phospholipid vesicles. *Biochemistry.* **1992**; 1493(31): 9912–9918
- Grinberg, M., Sarig, R., Zaltsman, Y., Frumkin, D., Grammatikakis, N., Reuven, E. & Gross, A. tBid Homooligomerizes in the Mitochondrial Membrane to Induce Apoptosis. *J Biol Chem.* **2001**; 277(14): 12237-12246

- Gross, A., Yin, X.M., Wang, K., Wei, M.C., Jockel, J. & Milliman, C. Caspase cleaved BID targets mitochondria and is required for cytochrome c release, while BCL-XL prevents this release but not tumor necrosis factor-R1/Fas death. *J Biol Chem.* **1999**; 274:1156–1163
- Groves, J.T. Parthasarathy, R. & Forstner, M.B. Fluorescence Imaging of Membrane Dynamics. *Annu. Rev. Biomed. Eng.* **2008**; 10: 331-338
- Hecht, E. Optics, Third Edition. Addison-Wesley. **1998**
- Heimlich, G., McKinnon, A.D., Bernardo, K., Brdiczka, D., Reed, J.C., Kain, R., Krönke, M. & Jürgensmeier, J.M. Bax-induced cytochrome c release from mitochondria depends on alpha-helices-5 and -6. *Biochem J.* **2004**; 15(378): 247-255
- Henriques, R., Lelek, M., Fornasiero, E.F., Valtorta, F., Zimmer, C., Mhlanga, M.M. QuickPALM: 3D real-time photoactivation nanoscopy image processing in ImageJ. *Nat Methods.* **2010**; 7(5): 339-40
- Hinds, M.G., Smits, C., Fredericks-Short, R., Risk, J.M., Bailey, M., Huang, D.C. & Day, C.L. Bim, Bad and Bmf: intrinsically unstructured BH3-only proteins that undergo a localized conformational change upon binding to prosurvival Bcl-2 targets. *Cell Death Differ.* **2007**; 14(1): 128-136
- Hsu, Y.T. & Youle, R.J. Nonionic detergents induce dimerization among members of the Bcl-2 family. *J Biol Chem.* **1997**; 272: 13829–13834
- Inoue, S. Handbook of Biological Confocal Microscopy: “Chapter 1 – Foundations of Confocal Scanned Imaging in Light Microscopy.” ed. Pawley, J.B. Plenum Press, New York. **1990**
- Ivashyna, O., Garcia-Saez, A.J., Ries, J., Christenson, E.T., Schwille, P. & Schlesinger, P.H. Detergent-Activated Bax Protein is a Monomer. *J Biol Chem.* **2009**; 284 (36): 23935-23946
- Kerr, J. F., Wyllie, A. H. & Currie, A. R. Apoptosis: a basic biological phenomenon with wide-ranging implications in tissue kinetics. *Br J Cancer.* **1972**; 26: 239–257
- Kiessling, V., Domanska, M.K., Murray, D., Wan, C. & Tamm, L.K. Wiley Encyclopedia of Chemical Biology: “Supported Lipid Bilayers: Development and Applications in Chemical Biology.” ed. Begley, T.P. John Wiley & Sons. **2008**

Kuwana, T., Mackey, M.R., Perkins, G., Ellisman, M.H., Latterich, M., Schneider, R., Green, D.R. & Newmeyer, D.D. Bid, Bax, and lipids cooperate to form supramolecular openings in the outer mitochondrial membrane. *Cell*. **2002**; 111: 331–342

Kvansakul, M., Yang, H., Fairlie, W.D., Czabotar, P.E., Fischer, S.F., Perugini, M.A., Huang, D.C. & Colman, P.M. Vaccinia virus anti-apoptotic F1L is a novel Bcl-2-like domain-swapped dimer that binds a highly selective subset of BH3-containing death ligands. *Cell Death Differ*. **2008**; 15(10): 1564-1571

Leber, B., Lin, J. & Andrews, D.W. Embedded together: The life and death consequences of interaction of the Bcl-2 family with membranes. *Apoptosis*. **2007**; 12: 897-911

Leber, B., Lin, J. & Andrews, D.W. Still embedded together binding to membranes regulates Bcl-2 protein interactions. *Oncogene*. **2010**; 29: 5221-5230

Letai, A., Bassik, M.C., Walensky, L.D., Sorcinelli, M.D., Weiler, S. & Korsmeyer, S.J. BH3 domains either sensitize or activate mitochondrial apoptosis, serving as prototype cancer therapeutics. *Cancer Cell*. **2002**; 2: 183–192

Lovell, J.F., Billen, L.P., Bindner, S., Shamas-Din, A., Fradin, C., Leber, B. & Andrews, D.W. Membrane Binding by tBid Initiates an Ordered Series of Events Culminating in Membrane Permeabilization by Bax. *Cell*. **2008**; 135 (12): 1074-1084

Lucken-Ardjomande, S., Montessuit, S., & Martinou, J.C. Contributions to Bax insertion and oligomerization of lipids of the mitochondrial outer membrane. *Cell Death and Differ*. **2008**; 15: 929-937

Magde, D., Elson, E. L. & Webb, W.W. Fluorescence correlation spectroscopy II. An experimental realization. *Biopolymers*. **1974**; 13: 29–61

Martinez-Caballero, S., Dejean, L.M., Kinnally, M.S., Oh, K.J., Mannella, C.A. & Kinnally, K.W. Assembly of the Mitochondrial Apoptosis-induced Channel, MAC. *J Biol Chem*. **2009**; 284 (18): 12235-12245

Mattson, M.P., Culmsee, C. & Yu, Z.F. Apoptotic and Antiapoptotic mechanisms in stroke. *Cell Tissue Res*. **2000**; 301: 173-187

McDonnell, J.M., Fushman, D., Milliman, C.L., Korsmeyer, S.J. & Cowburn, D. Solution structure of the proapoptotic molecule BID: a structural basis for apoptotic agonists and antagonists. *Cell*. **1999**; 96:625-634.

- Muller, J.D., Chen, Y. & Gratton, E. Resolving Heterogeneity on the Single Molecule Level with the Photon-Counting Histogram. *Biophys J.* **2000**; 78: 474-486.
- Nouraini, S., Six, E., Matsuyama, S., Krajewski, S. & Reed, J.C. The putative pore-forming domain of Bax regulates mitochondrial localization and interaction with Bcl-X(L). *Mol Cell Biol.* **2000**; 20(5): 1604-1615
- O'Neill, J.W., Manion, M.K., Maguire, B. & Hockerbery, D.M. Bcl-XL Dimerization by Three-dimensional Domain Swapping. *J Mol Biol.* **2006**; 356: 367-381
- Oh, K.J., Barbuto, S., Meyer, N., Kim, R.S., Collier, R.J. & Korsmeyer, S.J. Conformational changes in BID, a pro-apoptotic BCL-2 family member, upon membrane binding. A site-directed spin labeling study. *J Biol Chem.* **2005**; 280: 753-767
- Petros, A.M., Olejniczak, E.T. & Fesik, S.W. Structural Biology of the Bcl-2 family of proteins. *Biochim Biophys Acta.* **2004**; 1644: 83-94
- Przybylo, M., Sykora, J., Humpolichova, J., Benda, A., Zan, A & Hof, M. Lipid Diffusion in giant unilamellar vesicles is more than 2 times faster than in supported lipid bilayers under identical conditions. *Langmuir.* **2006**; 24: 9096-9099
- Puu, G. & Gustafson, I. Planar lipid bilayers on solid supports from liposomes – factors of importance for kinetics and stability. *Biochim Biophys Acta.* **1997**; 1327: 149-161
- Reed, J.C. Proapoptotic multidomain Bcl-2/Bax-family proteins: mechanisms, physiological roles, and therapeutic opportunities. *Cell death differ.* **2006**; 13: 1378-1386
- Reviakine, I., & Brisson, A. Formation of supported phospholipid bilayers from unilamellar vesicles investigated by atomic force microscopy. *Langmuir.* **2000**; 16: 1806-1815
- Richter, R.P. & Brisson, A.R. Following the Formation of Supported Lipid Bilayers on Mica: A Study Combining AFM, QCM-D and Ellipsometry. *Biophys J.* **2005**; 88: 3422-3433
- Richter, R.P., Berat, R. & Brisson, A.R. Formation of Solid-Supported Lipid Bilayers: An Integrated View. *Langmuir.* **2006**; 22: 3497-3505
- Rigler, R., Mets, U., Widengren, P. & Kask, P. Fluorescence Correlation Spectroscopy with high count rate and low background: analysis of translational diffusion. *Eur. Biophys. J.* **1993**; 22:169-175

- Saito, M., Korsmeyer, S.J & Schlesinger, P.H. BAX-dependant transport of Cytochrome C reconstituted in pure liposomes. *Nat Cell Biol.* **2000**; 2: 553-555
- Satsoura, D., Kučerka, N., Shivakumar, S., Pencer, J., Griffiths, C., Leber, B., Andrews, D.W., Katsaras, J. & Fradin, C. Interaction of the full-length Bax protein with biomimetic mitochondrial liposomes: a small-angle neutron scattering and fluorescence study. *BBA.* **2012**; 1818(3): 384-401
- Satsoura, D., Leber, B., Andrews, D.W. & Fradin, C. Circumvention of fluorophore photobleaching in fluorescence fluctuation experiments: a beam scanning approach. *Chemphyschem.* **2007**; 8(6): 834-48
- Schendel, S.L., Azimov, R., Pawłowski, K., Godzik, A., Kagan, B.L. & Reed, J.C. Ion Channel Activity of the BH3 Only Bcl-2 Family Member, BID. *J Biol Chem.* **1999**; 274 (31): 21932-21936
- Schlesinger, P.H. & Saito, M. The Bax pore in liposomes, Biophysics. *Cell Death and Differ.* **2006**; 13: 1403-1408
- Shamas-Din, A. Private communication of experimental results for NBD insertion. Department of Biochemistry and Biomedical Sciences, McMaster University. **2012**
- Sternberg, S.R. Biomedical Image Processing. *IEEE Computer.* **1983**; 16(1): 22-34
- Sun, X-M., Bratton, S.B., Butterworth, M., MacFarlane, M. & Cohen, G.M. Bcl-2 and Bcl-xl inhibit CD95-mediated apoptosis by preventing mitochondrial release of Smac/DIABLO and Subsequent Inactivation of X-linked Inhibitor-of-Apoptosis protein. *J Biol Chem.* **2002**; 277: 11345-11351
- Susin, S. A., Lorenzo, H.K., Zamzami, N., Marzo, I., Snow, B.E., Brothers, G.M., Mangion, J., Jacotot, E., Costantini, P., Loeffler, M., Larochette, N., Goodlett, D.R., Abersold, R., Siderovski, D.P., Penninger, J.M. & Kroemer, G. Molecular characterization of mitochondrial apoptosis-inducing factor. *Nature.* **1999**; 397: 441-446
- Suzuki, M., Youle, R.J. & Tjandra, N. Structure of Bax: Coregulation of Dimer Formation and Intracellular Localization. *Cell.* **2000**; 103: 645-654
- Tait, S.W.G. & Green, D.R. Mitochondria and cell death: outer membrane permeabilization and beyond. *Nat Rev Mol Cell Biol.* **2010**; 11: 621-632

Tan, C., Dlugosz, P.J., Peng, J., Zhang, Z., Lapolla, S.M., Plafker, S.M., Andrews, D.W. & Lin, J. Auto-activation of the apoptosis protein Bax increases mitochondrial membrane permeability and is inhibited by Bcl-2. *J Biol Chem.* **2006**; 281: 14764-14775

Terrones, O., Antonsson, B., Yamaguchi, H., Wang, H.G., Liu, J., Lee, R.M., Herrmann, A. & Basañez, G. Lipidic pore formation by the concerted action of proapoptotic Bax and tBid. *J Biol Chem.* **2004**; 279(29): 30081-30091

Thompson, N.L. Topics in Fluorescence Spectroscopy, Volume 1: “Techniques, Fluorescence Correlation Spectroscopy.” ed. Lakowicz, J.R. Plenum Press, New York. **1991**

Tsujimoto, Y. & Croce, C. M. Analysis of the structure, transcripts, and protein products of bcl-2, the gene involved in human follicular lymphoma. *Proc Natl Acad Sci USA.* **1986**; 83: 5214–5218

Valentijn, A.J., Upton, J.P. & Gilmore, A.P. Analysis of endogenous Bax complexes during apoptosis using blue native PAGE: implications for Bax activation and oligomerization. *Biochem J.* **2008**; 412: 347-357

Valero, J.G., Sancey, L., Kucharczak, J., Guillemin, Y., Gimenez, D., Prudent, J., Gillet, G., Salgado, J., Coll, J.L. & Aouacheria, A. Bax-derived membrane-active peptides act as potent and direct inducers of apoptosis in cancer cells. *J Cell Sci.* **2010**; 124(4): 556-564

Voet, D & Voet, J.G. Biochemistry, Third Edition. John Wiley & Sons Inc, Hoboken, NJ. **2004**

Walensky, L.D., Kung, A.L., Escher, I., Malia, T.J., Barbuto, S., Wright, R.D., Wagner, G., Verdine, G.L. & Korsmeyer, S.J. Activation of apoptosis by a hydrocarbon-staples BH3 helix. *Science.* **2004**; 305: 1466-1470

Wang, K., Yin, X.M., Chao, D.T., Milliman, C.L. & Korsmeyer, S.J. BID: a novel BH3 domain-only death agonist. *Genes Dev.* **1996**; 10:2859-2869.

Webb, R.H. Theoretical Basis of Confocal Microscopy. *Methods in Enzymology.* **1999**; 307: 3-26

Wei, M.C., Lindsten, T., Mootha, V.K., Weiler, S., Gross, A., Ashiya, M., Thompson, C.B. & Korsmeyer, S.J. tBID, a membrane-targeted death ligand, oligomerizes BAK to release cytochrome c. *Genes Dev.* **2000**; 14(16): 2060-71.

Willis, S.N., Fletcher, J.I., Kaufmann, T., van Delft, M.F., Chen, L., Czabotar, P.E., Ierino, H., Lee, E.F., Fairlie, W.D., Bouillet, P., Strasser, A., Kluck, R.M., Adams, J.M. & Huang, D.C. Apoptosis initiated when BH3 ligands engage multiple Bcl-2 homologs, not Bax or Bak. *Science*. **2007**; 315(5813): 856-859

Wolter, K.G., Hsu, Y.-T., Smith, C.L., Nechushtan, A., Xi, X.-G., & Youle, R.J. Movement of Bax from the cytosol to mitochondria during apoptosis. *J Cell Biol*. **1997**; 139: 1281-1292

Wu, Y., Wang, Y., Sun, Y., Zhang, L., Wang, D., Ren, F., Chang, D., Chang, Z. & Jia, B. RACK1 promotes Bax oligomerization and dissociates the interaction of Bax and Bcl-XL. *Cell Signal* . **2010**; 22: 1495-1501

Youle, R.J. & Strasser, A. The Bcl-2 protein family: opposing activities that mediate cell death. *Mol Cell Biol*. **2008**; 9: 47-59

Zhang, Z., Zhu, W., Lapolla, S.M., Miao, Y., Shao, Y., Falcone, M., Boreham, D., McFarlane, N., Ding, J., Johnson, A.E., Zhang, X.C., Andrews, D.W. & Lin, J. Bax forms an oligomer via separate, yet interdependent, surfaces. *J Biol Chem*. **2010**; 285(23): 17614-17627

Zou, H., Li, Y., Liu, X. & Wang, X. An APAF-1.cytochrome c multimeric complex is a functional apoptosome that activates procaspase-9. *J Biol Chem*. **1999**; 274: 11549-1155

## 7 Appendix – ImageJ script for automated image analysis

A description of each block of code precedes executable text and appears within borders (e.g. /\* description\*/).

Annotations appear immediately following a double backslash (e.g. //annotation).

```
/*-----\
```

Version 3: Aug. 2, 2011

- Amalgamation of versions 1 and 2.
- Order of code reflects the chronological order of analysis steps.
- Variables listed by order of use.

Version 4: Aug. 12, 2011

- shows copy image with detected spots regions erased during analysis loop

Version 5: Aug. 28, 2011

- moved radius (xradius, yradius) for ROI fitting into analysis loop
- Draws boxes around spot, measures total intensity of boxed area until brightest area found
- Sept. 24: outputs data to txt file

Version 6: Oct. 18, 2011

- separates output data into streaks and spots, sorts spots based on wellness of fit
- no cross drawn for streaks
- brightest pixel of spot indicated in blue

Version7: July 9, 2012

- spots/streaks separated by w0x, w0y values from fit
- streaks sorted good/bad based on gaussian fit
- no ROIs detected in outer 3 rows of pixels

```
\-----*/
```

```
/*-----\
```

Load JAVA packages for ImageJ API

```
\-----*/
```

```
import ij.*;
import ij.process.*;
import ij.gui.*;
import java.awt.*;
import ij.io.*;
import ij.io.OpenDialog;
import java.util.*;
import java.io.*;
import javax.imageio.*;
import java.awt.image.BufferedImage;
import java.io.BufferedReader;
import java.io.BufferedWriter;
import java.io.FileNotFoundException;
import java.io.FileReader;
import java.io.FileWriter;
import java.io.IOException;
```



```

import ij.ImagePlus;
import ij.process.ImageProcessor;
import ij.IJ;
import ij.plugin.filter.*;

public class GaussianFit_Version7 implements PlugInFilter
{
    ImagePlus imp;
    ImageStack stack;

    /*-----\
Setup method: Getting info about the PlugIn
-----*/

    public int setup(String arg, ImagePlus imp)
    {
        this.imp = imp;
        return DOES_16;
    }

    /*-----\
Main program
-----*/

    public void run(ImageProcessor ip)
    {

        /* Declaration of variables */

        //getting info about the image stack
        int size=imp.getStackSize();
        int width = ip.getWidth();
        int height = ip.getHeight();
        int dimension = width*height;
        String title = imp.getTitle();
        String dir = IJ.getDirectory("image");

        //variables in loop finding brightest slice
        double SumIm[] = new double[size+1];
        double MaxSum = 0;

        // slice number of brightest slice
        int position = 0;

        // variables for imaging conditions
        double pixelsize = 100;
        int positionuser = 1;
        double CPP = 20;
        String location = "";
        String channel = "";

        //variables for creating checkboxes

```

```
String labels[]={"Blue channel (488 nm)"," Red channel (633 nm)","analyze membrane", "analyze
solution"};
boolean values[]={false, true, false, false};
boolean allgood=false;

// array for saving original image data
double mirror[][]= new double [width][height];

// variables for creating copy image with 10X resolution (1000x1000 pixels)
double maxint = 0;
double gardpixel = 0;
int c = 0;

// variables for finding estimated noise
double minint = 4095;
double noiseest=0;
int noisecounter = 0;

// variable for theoretical w0
double wnotuser = 0;
// variable for threshold used in analysis
double pthreshold = 0;

// variables for method "drawCross"
int xpos = 0;
int ypos = 0;
int sizex = 0;
int sizey = 0;

// variable for looping analysis loop
int endloop = 0;

// variables for finding pixels of highest intensity in copy image
int xmaxint = 0;
int ymaxint = 0;

// variables defining ROI for Gaussian fit
int xmin = 0;
int xmax = 0;
int ymin = 0;
int ymax = 0;

// variables for drawing gaussian mask around ROI
double roixmin = 0;
double roixmax = 0;
double roiymin = 0;
double roymax = 0;
double roixmingard = 0;
double roixmaxgard = 0;
double roiymingard = 0;
double roymaxgard = 0;

// variables for finding centre of mass within ROI for Gaussian fit
```

```

double xweight = 0;
double yweight = 0;
double gard = 0;
double xcenter=0;
double ycenter=0;

// variables for 4-parameter gaussian fit
double intensityfit = 0;
double noisefit = 0;
double wnotfit = 0;
double wnotfity = 0;
int kgard = 0;
int lgard = 0;
int mgard = 0;
int ngard = 0;

// krange describes the expected range in % of the max intensity
int kmax= 5;
double krange = 50;
int linter = 30;
int mmax= 5;
double mrange = 50;
int ninter = 20;

// variables for counting spots and streaks found
int counter = 1;
int badcounter = 1;

//arrays for writing data to file
double spotArray[][] = new double [16][250];
double streakArray[][] = new double [16][600];

/* Find the brightest image in the stack to ask whether this is the one that needs to be analyzed */

for (int k=1; k<size+1; k++)
{
    imp.setSlice(k);
    double Sum = 0;
    for (int i=0; i<width; i++)
    {
        for (int j=0; j<height; j++)
        {
            Sum = Sum + ip.getPixelValue(i,j);
        }
    }
    SumIm[k]=Sum;
    if (Sum>MaxSum)
    {
        MaxSum = Sum; position = k;
    }
}

/* Dialog box for user to enter parameters for analysis*/

```

```

GenericDialog gd = new GenericDialog("Imaging Conditions");
gd.addStringField("Directory to save data", dir);
gd.addMessage("The brightest image in stack is: " + position);
gd.addCheckboxGroup(2,2, labels, values);
gd.addNumericField("Slice to analyze", position,0);
gd.addNumericField("Specific brightness of monomer (kHz)", CPP, 0);
gd.addNumericField("Pixel Size (nm): ", pixelsize, 1);
gd.showDialog();
if (gd.wasCanceled()) return;

dir = gd.getNextString();
boolean blue = gd.getNextBoolean();
boolean red = gd.getNextBoolean();
boolean membrane = gd.getNextBoolean();
boolean solution = gd.getNextBoolean();
positionuser = (int) gd.getNextNumber();
CPP = (double) gd.getNextNumber();
pixelsize = (double) gd.getNextNumber();

if (blue==true && red==false) {channel = "blue"; wnotuser = 240;}
if (red==true && blue==false) {channel = "red"; wnotuser = 280;}
if (membrane==true && solution==false && blue==true && red==false || membrane==true &&
solution==false && red==true && blue==false ||solution==true && membrane==false &&
blue==true && red==false || solution==true && membrane==false && red==true &&
blue==false) {allgood=true;} else {allgood=false;}
if (allgood==false) {return;}
if (membrane==true) {location="membrane";} else {location="solution";}

imp.setSlice(positionuser);
String filename = title + "slice #" + positionuser + ".txt";

/* Copies image to array */

for (int i=0; i<width; i++)
    {
        for (int j=0; j<height; j++)
            {
                mirror[i][j]=ip.getPixelValue(i,j);
            }
    }

/* Create a copy image with a 10 times higher resolution to show detected objects */

ImagePlus Result_image = NewImage.createRGBImage("Result", width*10, height*10, 1,
NewImage.FILL_RAMP);
ImageProcessor Result_ip = Result_image.getProcessor();
maxint = 0;
for (int i=0; i<width; i++)
    {
        for (int j=0; j<height; j++)
            {
                if (mirror[i][j]>maxint)

```

```

                {
                    maxint=mirror[i][j];
                }
            }
        }
    for (int i=0; i<width; i++)
    {
        for (int j=0; j<height; j++)
        {
            gardpixel=(int) (ip.getPixelValue(i,j)/maxint*255);
            c=((0 & 0xff)<<16) | (((int) gardpixel & 0xff)<<8) | 0 & 0xff;
            for (int k=0; k<10; k++)
            {
                for (int l=0; l<10; l++)
                {
                    Result_ip.putPixel(10*i+k,10*j+l,c);
                }
            }
        }
    }
}

```

Result\_image.show();

ImagePlus Result\_goodspot = NewImage.createRGBImage("Good spots", width\*10, height\*10, 1, NewImage.FILL\_RAMP);

ImageProcessor Result\_gs = Result\_goodspot.getProcessor();

```

for (int i=0; i<width; i++)
{
    for (int j=0; j<height; j++)
    {
        gardpixel=(int) (ip.getPixelValue(i,j)/maxint*255);
        c=((0 & 0xff)<<16) | (((int) gardpixel & 0xff)<<8) | 0 & 0xff;
        for (int k=0; k<10; k++)
        {
            for (int l=0; l<10; l++)
            {
                Result_gs.putPixel(10*i+k,10*j+l,c);
            }
        }
    }
}

```

ImagePlus Result\_badspot = NewImage.createRGBImage("Bad spots", width\*10, height\*10, 1, NewImage.FILL\_RAMP);

ImageProcessor Result\_bs = Result\_badspot.getProcessor();

```

for (int i=0; i<width; i++)
{
    for (int j=0; j<height; j++)
    {
        gardpixel=(int) (ip.getPixelValue(i,j)/maxint*255);
        c=((0 & 0xff)<<16) | (((int) gardpixel & 0xff)<<8) | 0 & 0xff;
        for (int k=0; k<10; k++)
        {

```

```

        for (int l=0; l<10; l++)
            {
                Result_bs.putPixel(10*i+k,10*j+l,c);
            }
        }
    }

ImagePlus Result_goodstreak = NewImage.createRGBImage("Good streaks", width*10,
height*10, 1, NewImage.FILL_RAMP);
ImageProcessor Result_gst = Result_goodstreak.getProcessor();
for (int i=0; i<width; i++)
    {
        for (int j=0; j<height; j++)
            {
                gardpixel=(int) (ip.getPixelValue(i,j)/maxint*255);
                c=((0 & 0xff)<<16) | (((int) gardpixel & 0xff)<<8) | 0 & 0xff;
                for (int k=0; k<10; k++)
                    {
                        for (int l=0; l<10; l++)
                            {
                                Result_gst.putPixel(10*i+k,10*j+l,c);
                            }
                    }
            }
    }

ImagePlus Result_badstreak = NewImage.createRGBImage("Bad streaks", width*10, height*10,
1, NewImage.FILL_RAMP);
ImageProcessor Result_bst = Result_badstreak.getProcessor();
for (int i=0; i<width; i++)
    {
        for (int j=0; j<height; j++)
            {
                gardpixel=(int) (ip.getPixelValue(i,j)/maxint*255);
                c=((0 & 0xff)<<16) | (((int) gardpixel & 0xff)<<8) | 0 & 0xff;
                for (int k=0; k<10; k++)
                    {
                        for (int l=0; l<10; l++)
                            {
                                Result_bst.putPixel(10*i+k,10*j+l,c);
                            }
                    }
            }
    }

double maxmax=maxint;

/* Calculate intensity threshold to use for analysis and number of pixels with lowest intensity, draw crosses
*/

for (int i=0; i<width; i++)
    {

```

```

        for (int j=0; j<height; j++)
        {
            if (mirror[i][j]<minint)
            {
                minint=mirror[i][j];
            }
        }
    }
    for (int i=0; i<width; i++)
    {
        for (int j=0; j<height; j++)
        {
            if (mirror[i][j] == minint)
            {
                noisecounter++;
                drawCross(i*10+5, j*10+5, 1, 1, Result_ip);
                int rad=1;
                for (int k=-rad; k<rad+1; k++)
                {
                    for (int l=-rad; l<rad+1; l++)
                    {
                        if (i+k>-1 && i+k<width && j+l>-1 && j+l<height)
                        {noisest = noisest +
                        mirror[i+k][j+l]/Math.pow(2*(rad+1),2);}
                    }
                }
            }
        }
    }
}

```

```

// average pixel brightness in image
double everest=SumIm[positionuser]/dimension;
// estimated noise from points of low intensity
noisest=noisest/noisecounter;
// threshold value for analysis
if (membrane==true) {pthreshold = (everest+(0.5*CPP));}
if (solution==true) {pthreshold = (everest+(0.1*CPP));}

```

```

GenericDialog analysis = new GenericDialog("Analysis Conditions");
analysis.addMessage("Channel: " + channel + "          theoretical w0: " + wnotuser);
analysis.addMessage("specific brightness of monomer: " + CPP);
analysis.addMessage("threshold set for analyzing: " + location);
analysis.addMessage("The slice that will be analyzed: " + positionuser);
analysis.addMessage("Average pixel intensity (ph/pxl): " +
Double.toString((double)(Math.round(everest*1000))/1000));
analysis.addMessage("Estimated noise (ph/pxl): " +
Double.toString((double)(Math.round(noisest*1000))/1000) + " calculated from " +
Integer.toString(noisecounter) + " points");
analysis.addMessage("Threshold that will be used: " + pthreshold);
analysis.showDialog();
if (analysis.wasCanceled()) return;

```

```

IJ.saveAs(Result_image, ".png", dir + filename + " background points");

```

```

Result_goodspot.show();
Result_badspot.show();
Result_goodstreak.show();
Result_badstreak.show();

/* Calculating radii for fit from w0 from user entered value */

// minimum distance between two detected particles
int radius = (int) Math rint(1*wnotuser/pixelsize+1);
// size of the region used to calculate the center of mass and perform the fit
int radius2 = (int) Math rint(1*wnotuser/pixelsize+1);

/* Analysis loop begins here*/

while (endloop == 0)
{

/* Find the ROI(s) - point(s) of highest intensity in the image */

maxint = 0;
for (int i=2; i<width-2; i++)
{
for (int j=2; j<height-2; j++)
{
if (mirror[i][j]>maxint)
{
maxint=mirror[i][j];
xmaxint=i;ymaxint=j;
}
}
}
if (maxint>pthreshold)
{

/* Determine the boundary of the ROI(s) for the gaussian mask and gaussian fit */

int xradius = radius;
int yradius = radius;
if (xmaxint<radius || xmaxint>width-1-radius) {xradius=Math.min(xmaxint,width-1-
xmaxint);}
if (ymaxint<radius || ymaxint>height-1-radius) {yradius=Math.min(ymaxint,height-1-
ymaxint);}
xmin=xmaxint-xradius;
xmax=xmaxint+xradius;
ymin=ymaxint-yradius;
ymax=ymaxint+yradius;

/* Finding area around ROI with highest total intensity (Gaussian mask) */

double maxroiintensity = 0;
for (int i=xmin; i<xmax+1; i++)
{
for (int j=ymin; j<ymax+1; j++)

```



```

{
for (double m = 0; m<10; m++)
{
double xdecimal = m*0.1;
for (double n=0; n<10; n++)
{
double ydecimal = n*0.1;

double roiintensity = 0;
if (i<radius) {roixmin=xmin;} else {roixmin =
i+xdecimal-radius;}
if (i>width-1-radius) {roixmax=xmax;} else {roixmax
= i+xdecimal+radius;}
if (j<radius) {roiymn=ymin;} else {roiymn =
j+ydecimal-radius;}
if (j>height-1-radius) {roiymax=ymax;} else
{roiymax = j+ydecimal+radius;}

for (double k=roixmin; k<roixmax+1; k++)
{
for (double l=roiymn; l<roiymax+1; l++)
{
roiintensity = roiintensity +
mirror[(int) k][(int) l]*Math.exp(-
2*Math.pow((k-
(roixmax+roixmin)/2)*pixelsize/wn
otuser,2))*Math.exp(-
2*Math.pow((l-
(roiymin+roiymn)/2)*pixelsize/wn
otuser,2));
}
}
}
//if ROI is along left edge of image, weight of leftmost pixel not subtracted when moving increments; if
ROI is along right edge of image, weight of rightmost pixel not added when moving increments

for (double k=roiymn; k<roiymax+1; k++)
{
if (i>radius) {roiintensity = roiintensity -
(mirror[(int) roixmin][(int) k]*Math.exp(-
2*Math.pow((k-
(roixmax+roixmin)/2)*pixelsize/wnotuser,2)
)*(xdecimal));}
if (i<width-1-radius) {roiintensity =
roiintensity + (mirror[Math.min((int)
roixmax+1, width-1)][(int) k]*Math.exp(-
2*Math.pow((k-(roixmax+roixmin)/2)
*pixelsize/wnotuser,2))*(xdecimal));}
}
}
//if ROI is along top edge of image, weight of topmost pixel not subtracted when moving increments; if
ROI is along bottom edge of image, weight of bottommost pixel not added when moving increments

for (double l=roixmin; l<roixmax+1; l++)
{

```

```

        if (j>radius) {roiintensity = roiintensity -
        (mirror [(int) l][(int) roiymin]*Math.exp(-
        2*Math.pow((1-(roiymax+roiymin)/2)
        *pixelsize/wnotuser,2))*(ydecimal));}
        if (j<width-1-height) {roiintensity =
        roiintensity + (mirror [(int) l][Math.min((int)
        roiymin+1, height-1)]*Math.exp(-
        2*Math.pow((1-(roiymax+roiymin)/2)
        *pixelsize/wnotuser,2))*(ydecimal));}
        }
    }
}

if (roiintensity>maxroiintensity)
{maxroiintensity=roiintensity; roixmingard=roixmin;
roixmaxgard=roixmax; roiymingard=roiymin;
roymaxgard=roymax;}
}
}

/* Fit ROI to a 4-parameter Gaussian function */

xweight = 0;
yweight = 0;
gard=0;

//finding the centre of mass for ROI
for (int i=xmin; i<xmax+1; i++)
{
    for (int j=ymin; j<ymin+1; j++)
    {
        xweight = xweight+i*(ip.getPixelValue(i,j)-noiseest);
        yweight = yweight+j*(ip.getPixelValue(i,j)-noiseest);
        gard=gard+(ip.getPixelValue(i,j)-noiseest);
    }
}
xcenter=xweight/gard;
ycenter=yweight/gard;

double chisquare = 0;
double chisquaregard = 4000;
for (int k=-kmax;k<kmax+1;k++)
{
    intensityfit = (maxint-(noiseest+everest)/2)+((double) k)/((double)
    kmax)*(maxint-(noiseest+everest)/2)*((double) krange)/100;
    for (int l=0;l<linter+1;l++)
    {
        noisefit = noiseest+l*(2*everest-noiseest)/linter;
        for (int m=-mmax;m<2*mmax+1;m++)
        {
            wnotfit=wnotuser+((double) m)/((double)
            mmax)*wnotuser*((double) mrange)/100.0;
            for (int n=0;n<ninter;n++)

```

```

        {
        wnotfity=pixelsize/2+n*(2*wnotuser-
        pixelsize)/ninter;
        double difference = 0;
        chisquare = 0;
        for (int i=xmin; i<xmax+1; i++)
        {
            for (int j=ymin; j<ymax+1; j++)
            {
                difference = ip.getPixelValue(i,j)-
                noisefit-intensityfit*Math.exp(-
                2*Math.pow((i-
                xcenter)*pixelsize/wnotfit,2))*Math
                .exp(-2*Math.pow((j-
                ycenter)*pixelsize/wnotfity,2));
                chisquare=chisquare +
                Math.pow(difference,2);
            }
        }
        chisquare=chisquare/(xmax+1-xmin)/(ymax+1-
        ymin)/maxint;
        if (chisquare<chisquaregard)
        {kgard=k;lgard=l;mgard=m;ngard=n;chisquaregard=c
        hisquare;}
        }
    }
}

intensityfit=(maxint-(noiseest+everest)/2)+((double) kgard)/((double) kmax)*(maxint-
(noiseest+everest)/2)*((double) krange)/100;
noisefit = noiseest+lgard*(everest-noiseest)/linter;
wnotfit=wnotuser+((double) mgard)/((double) mmax)*wnotuser*((double)
mrange)/100.0;
wnotfity=wnotfity=pixelsize/2+ngard*(2*wnotuser-pixelsize)/ninter;

/* Calculate position to draw crosses and numbers in copy image */

xpos = ((int) (Math rint(xcenter*10)))+5;
ypos = ((int) (Math rint(ycenter*10)))+5;
sizex = ((int) (wnotfit/pixelsize))*10;
sizey = ((int) (wnotfity/pixelsize))*10;

/* if ROI is deemed to be a streak, data is placed in streakArray, streak drawn in copy image*/

if (Math.sqrt(Math.abs(Math.pow((wnotuser-wnotfit),2))+
Math.abs(Math.pow((wnotuser-wnotfity),2))))>=(wnotuser/2)
{
    streakArray[0][badcounter-1] = badcounter;
    streakArray[1][badcounter-1] = maxint;
    streakArray[2][badcounter-1] = xmaxint;
    streakArray[3][badcounter-1] = ymaxint;
    streakArray[4][badcounter-1] = xcenter;
    streakArray[5][badcounter-1] = ycenter;
}

```

```

streakArray[6][badcounter-1] = intensityfit;
streakArray[7][badcounter-1] = noisefit;
streakArray[8][badcounter-1] = wnotfit;
streakArray[9][badcounter-1] = wnotfity;
streakArray[10][badcounter-1] = maxroiintensity;
streakArray[11][badcounter-1] = kgard;
streakArray[12][badcounter-1] = lgard;
streakArray[13][badcounter-1] = mgard;
streakArray[14][badcounter-1] = ngard;
streakArray[15][badcounter-1] = chisquaregard;

if (streakArray[11][badcounter-1]>kmax && streakArray[11][badcounter-1]<kmax && streakArray[12][badcounter-1]>0 && streakArray[12][badcounter-1]<linter && streakArray[9][badcounter-1]<=wnotuser)
    {
    drawmaxpoint(xmaxint, ymaxint, Result_gst);
    drawstreaknumber(badcounter, xpos, ypos, width, radius, Result_gst);
    Result_goodstreak.draw();
    }
else
    {
    drawmaxpoint(xmaxint, ymaxint, Result_bst);
    drawstreaknumber(badcounter, xpos, ypos, width, radius, Result_bst);
    Result_badstreak.draw();
    }
badcounter = badcounter+1;

```

/\* Erases the streak in the image \*/

```

xmin = Math.max((int)Math.rint((xcenter-wnotfit/pixelsize)), 0);
xmax = Math.min((int)Math.rint((xcenter+wnotfit/pixelsize)),width-1);
ymin = Math.max((int)Math.rint((ycenter-wnotfity/pixelsize)), 0);
ymax = Math.min((int)Math.rint((ycenter+wnotfity/pixelsize)), height-1);
for (int i=xmin; i<xmax+1; i++)
    {
    for (int j=ymin; j<ymax+1; j++)
        {mirror[i][j]=0;}
    }
mirror[xmaxint][ymaxint]=0;
}

```

/\*if ROI is deemed to be a spot, data is placed in spotArray, spot location and area of gaussian fit drawn on copy image for good spots\*/

```

else
    {
    spotArray[0][counter-1] = counter;
    spotArray[1][counter-1] = maxint;
    spotArray[2][counter-1] = xmaxint;
    spotArray[3][counter-1] = ymaxint;
    spotArray[4][counter-1] = xcenter;
    spotArray[5][counter-1] = ycenter;
    }

```

```

spotArray[6][counter-1] = intensityfit;
spotArray[7][counter-1] = noisefit;
spotArray[8][counter-1] = wnotfit;
spotArray[9][counter-1] = wnotfity;
spotArray[10][counter-1] = maxroiintensity;
spotArray[11][counter-1] = kgard;
spotArray[12][counter-1] = lgard;
spotArray[13][counter-1] = mgard;
spotArray[14][counter-1] = ngard;
spotArray[15][counter-1] = chisquaregard;

if (spotArray[11][counter-1]>-kmax && spotArray[11][counter-1]<kmax &&
spotArray[12][counter-1]>0 && spotArray[12][counter-1]<linter)
    {
        drawmaxpoint(xmaxint, ymaxint, Result_gs);
        drawBox(roixmingard, roixmaxgard, roiymingard, roiymaxgard,
Result_gs);
        drawCross(xpos, ypos, sizex, sizey, Result_gs);

        drawspotnumber(counter, xpos, ypos, Result_gs);
        Result_goodspot.draw();
    }
else
    {
        drawmaxpoint(xmaxint, ymaxint, Result_bs);
        drawBox(roixmingard, roixmaxgard, roiymingard, roiymaxgard,
Result_bs);
        drawCross(xpos, ypos, sizex, sizey, Result_bs);
        drawspotnumber(counter, xpos, ypos, Result_bs);
        Result_badspot.draw();
    }
counter = counter+1;

/* Erases the spot in the image */
xmin = (int) Math.max((Math.min(xmaxint-(radius2), xmaxint-
Math rint(wnotfit/pixelsize))), 0);
xmax = (int) Math.min((Math.max(xmaxint+(radius2),
xmaxint+Math rint(wnotfit/pixelsize))), width-1);
ymin = (int) Math.max((Math.min(ymaxint-(radius2), ymaxint-
Math rint(wnotfity/pixelsize))), 0);
ymax = (int) Math.min((Math.max(ymaxint+(radius2),
ymaxint+Math rint(wnotfity/pixelsize))), height-1);
for (int i=xmin; i<xmax+1; i++)
    {
        for (int j=ymin; j<ymax+1; j++)
            {mirror[i][j]=0;}
    }
}

/* Gives the choice of looking at the original ROI and fit of ROI */

int choicefit = 0 ;
GenericDialog viewfit = new GenericDialog("Result of fit");

```

```

viewfit.addNumericField("Do you want to see the result of the fit (No:0,
Yes:1)",choicefit, 0);
viewfit.showDialog();
if (viewfit.wasCanceled()) return;
choicefit = (int) viewfit.getNextNumber();

if (choicefit ==1)
{
int b=0;
ImagePlus Particle_image = NewImage.createImage("Particle", xradius*2+1,
yradius*2+1, 1, 16, NewImage.FILL_RAMP);
ImagePlus Fit_image = NewImage.createImage("Fit", (xradius*2+1),
(yradius*2+1), 1, 16, NewImage.FILL_RAMP);
ImageProcessor Particle_ip = Particle_image.getProcessor();
ImageProcessor Fit_ip = Fit_image.getProcessor();
for (int i=0; i<xradius*2+1; i++)
{
for (int j=0; j<yradius*2+1; j++)
{
b=(int) (ip.getPixelValue(xmaxint-xradius+i,ymaxint-
yradius+j));
Particle_ip.putPixel(i,j,b);
b= (int) (noisefit+intensityfit*Math.exp(-
2*Math.pow((xmaxint-xradius+i-
xcenter)*pixelsize/wnotfit,2))*Math.exp(-
2*Math.pow((ymaxint-yradius+j-
ycenter)*pixelsize/wnotfit,2));
Fit_ip.putPixel(i,j,b);
}
}
Particle_image.show();
Fit_image.show();
}
}
else
{endloop = 1;}
}

/*Analysis loop ends here*/

/*Numerical data is output as a text file*/

write(dir, filename, width, height, channel, MaxSum, positionuser, wnotuser, spotArray, streakArray,
position, noiseest, counter, badcounter, kmax, linter, mmax, ninter, noisecounter, everest, pthreshold, CPP,
location);

IJ.saveAs(Result_goodspot, ".png", dir + filename + " good spots");
IJ.saveAs(Result_badspot, ".png", dir + filename + " bad spots");
IJ.saveAs(Result_goodstreak, ".png", dir + filename + " good streaks");
IJ.saveAs(Result_badstreak, ".png", dir + filename + " bad streaks");

/* Draws copy image of erased areas (spots and streaks that are found) */

```

```

ImagePlus Erase_image = NewImage.createRGBImage("Erased spots", width*10, height*10, 1,
NewImage.FILL_RAMP);
ImageProcessor Erase_ip = Erase_image.getProcessor();

for (int i=0; i<width; i++)
    {
        for (int j=0; j<height; j++)
            {
                gardpixel=(int) (mirror[i][j]/maxmax*255);
                c=((0 & 0xff)<<16) | (((int) gardpixel & 0xff)<<8) | 0 & 0xff;
                for (int k=0; k<10; k++)
                    {
                        for (int l=0; l<10; l++)
                            {
                                Erase_ip.putPixel(10*i+k,10*j+l,c);
                            }
                    }
            }
        Erase_image.show();
        IJ.saveAs(Erase_image, ".png", dir + filename + " erased areas");
    }

/* Method for drawmaxpoint - pixel of highest intensity for ROIs drawn in copy image */

public static void drawmaxpoint(int xmaxint, int ymaxint, ImageProcessor ip)
    {
        int paintvalue= ((0 & 0xff)<<16) | ((0 & 0xff)<<8) | 255 & 0xff;
        ip.setValue(paintvalue);
        ip.setLineWidth(10);
        ip.drawDot(xmaxint*10+5, ymaxint*10+5);
    }

/* Method for drawstreaknumber - draws number beside streaks that are found */

public static void drawstreaknumber(int badcounter, int xpos, int ypos, int width, int radius, ImageProcessor
ip)
    {
        int paintvalue= ((148 & 0xff)<<16) | ((0 & 0xff)<<8) | 211 & 0xff;
        ip.setValue(paintvalue);
        Font f;
        f = new Font ("SansSerif", Font.BOLD, 20);
        ip.setFont(f);
        if ((xpos-5)/10>width-radius) {xpos = xpos-25;}
        if ((ypos-5)/10<radius) {ypos = ypos+25;}
        ip.drawString(Integer.toString(badcounter), xpos, ypos);
    }

/* Method for drawspotnumber - draws numbers beside spots that are found*/

public static void drawspotnumber(int counter, int xpos, int ypos, ImageProcessor ip)
    {
        int paintvalue= ((255 & 0xff)<<16) | ((255 & 0xff)<<8) | 0 & 0xff;

```

```

ip.setValue(paintvalue);
Font f;
f = new Font ("SansSerif", Font.BOLD, 20);
ip.setFont(f);
ip.drawString(Integer.toString(counter), xpos, ypos);
}

```

/\* Method for drawBox - draws boxes around areas of highest total intensity after gaussian blur\*/

```

public static void drawBox(double roixmingard, double roixmaxgard, double roiy mingard, double
roiymaxgard, ImageProcessor ip)
{
int paintvalue= ((255 & 0xff)<<16) | ((0 & 0xff)<<8) | 0 & 0xff;
ip.setValue(paintvalue);
ip.setLineWidth(1);
ip.drawLine(((int)(Math rint(roixmingard*10)))+5, ((int)(Math rint(roiy maxgard*10)))+5,
((int)(Math rint(roixmaxgard*10)))+5, ((int)(Math rint(roiy maxgard*10)))+5);
ip.drawLine(((int)(Math rint(roixmingard*10)))+5, ((int)(Math rint(roiy mingard*10)))+5,
((int)(Math rint(roixmaxgard*10)))+5, ((int)(Math rint(roiy mingard*10)))+5);
ip.drawLine(((int)(Math rint(roixmingard*10)))+5, ((int)(Math rint(roiy maxgard*10)))+5,
((int)(Math rint(roixmingard*10)))+5, ((int)(Math rint(roiy mingard*10)))+5);
ip.drawLine(((int)(Math rint(roixmaxgard*10)))+5, ((int)(Math rint(roiy maxgard*10)))+5,
((int)(Math rint(roixmaxgard*10)))+5, ((int)(Math rint(roiy mingard*10)))+5);
}

```

/\* Method for "drawCross" - draws crosses for spots with good gaussian profile \*/

```

public static void drawCross(int xpos, int ypos, int sizex, int sizey, ImageProcessor ip)
{
int paintvalue= ((255 & 0xff)<<16) | ((255 & 0xff)<<8) | 255 & 0xff;
ip.setValue(paintvalue);
ip.setLineWidth(1);
ip.drawLine(xpos-sizex,ypos,xpos+sizex,ypos);
ip.drawLine(xpos,ypos-sizey,xpos,ypos+sizey);
}

```

/\*Method for write - writes data to text file\*/

```

protected void write(String dir, String filename, int width, int height, String channel, double MaxSum, int
positionuser, double wnotuser, double[][] spotArray, double[][] streakArray, int position, double noiseest,
int counter, int badcounter, int kmax, int linter, int mmax, int ninter, int noisecounter, double everest,
double pthreshold, double CPP, String location)
{
try
{
BufferedWriter bw = new BufferedWriter(new FileWriter(dir + filename));
bw.write(filename + "\n");
bw.write("Image dimensions are " + width + "x" + height + " pixels" + "\n");
bw.write("The brightest image is slice #" + position + ", Average brightness: " +
MaxSum/(width*height) + " ph/pxl" + "\n");
bw.write("Analysis conditions - channel: " + channel + " theoretical w0: " + wnotuser +
" CPP: " + CPP + " threshold set for: " + location + "\n");
bw.write("The slice analyzed was # " + positionuser + "\n");
}
}

```



```

bw.write("average pixel brightness: " + everest + "\n");
bw.write("noise: " + noiseest + " ,calculated from " + noisecounter + " points" + "\n");
bw.write("threshold used: " + pthreshold + "\n");
bw.write("spots found: " + (counter-1) + " streaks founds: " + (badcounter-1) + "\n");
bw.write("fit range intensity: " + -kmax + "-" + kmax + " noise: 0-" + linter + " wnofitx:
" + -mmax + "-" + mmax + " wnofity: 0-" + ninter + "\n");
bw.write("N MaxIntensity(ph/pxl) xint(pxl) yint(pxl) xcenter(pxl) ycenter(pxl)
fitintensity(ph/pxl) fitnoise(ph/pxl) fitw0x(nm) fitw0y(nm) totalIntensity(ph) intensity
noise w0x w0y chisquare \n");

bw.write("streaks" + "\n");
for (int ii = 0; ii<badcounter-1; ii++)
{
    for (int jj = 0; jj<16; jj++)
    {
        bw.write(Double.toString(streakArray[jj][ii]));
        if (jj<16){ bw.write(" ");}
    }
    bw.write("\n");
}
bw.write("good streaks" + "\n");
for (int ii = 0; ii<badcounter-1; ii++)
{
    if (streakArray[11][ii]>-kmax && streakArray[11][ii]<kmax &&
streakArray[12][ii]>0 && streakArray[12][ii]<linter &&
streakArray[9][ii]<=wnotuser)
    {
        for (int jj = 0; jj<16; jj++)
        {
            bw.write(Double.toString(streakArray[jj][ii]));
            if (jj<16){ bw.write(" ");}
        }
        bw.write("\n");
    }
}
bw.write("intensity out of bounds" + "\n");
for (int ii = 0; ii<badcounter-1; ii++)
{
    if (streakArray[11][ii]==-kmax || streakArray[11][ii]==kmax)
    {
        for (int jj = 0; jj<16; jj++)
        {
            bw.write(Double.toString(streakArray[jj][ii]));
            if (jj<16){ bw.write(" ");}
        }
        bw.write("\n");
    }
}
bw.write("background out of bounds" + "\n");
for (int ii = 0; ii<badcounter-1; ii++)
{
    if (streakArray[12][ii]==0 || streakArray[12][ii]==linter)
    {

```

```

        for (int jj = 0; jj<16; jj++)
            {
                bw.write(Double.toString(streakArray[jj][ii]));
                if (jj<16){ bw.write(" ");}
            }
        bw.write("\n");
    }
    bw.write("w0y too large" + "\n");
    for (int ii = 0; ii<badcounter-1; ii++)
    {
        if (streakArray[9][ii]>wnotuser)
            {
                for (int jj = 0; jj<16; jj++)
                    {
                        bw.write(Double.toString(streakArray[jj][ii]));
                        if (jj<16){ bw.write(" ");}
                    }
                bw.write("\n");
            }
    }
    bw.write("spots" + "\n");
    for (int ii = 0; ii<counter-1; ii++)
    {
        for (int jj = 0; jj<16; jj++)
            {
                bw.write(Double.toString(spotArray[jj][ii]));
                if (jj<16){ bw.write(" ");}
            }
        bw.write("\n");
    }
    bw.write("good guassian fits" + "\n");
    for (int ii = 0; ii<counter-1; ii++)
    {
        if (spotArray[11][ii]>-kmax && spotArray[11][ii]<kmax &&
            spotArray[12][ii]>0 && spotArray[12][ii]<linter)
            {
                for (int jj = 0; jj<16; jj++)
                    {
                        bw.write(Double.toString(spotArray[jj][ii]));
                        if (jj<16){ bw.write(" ");}
                    }
                bw.write("\n");
            }
    }
    bw.write("intensity out of bounds" + "\n");
    for (int ii = 0; ii<counter-1; ii++)
    {
        if (spotArray[11][ii]==-kmax || spotArray[11][ii]==kmax)
            {
                for (int jj = 0; jj<16; jj++)
                    {
                        bw.write(Double.toString(spotArray[jj][ii]));
                    }
            }
    }

```

```

                if (jj<16){ bw.write(" ");}
            }
            bw.write("\n");
        }
    }
    bw.write("background out of bounds" + "\n");
    for (int ii = 0; ii<counter-1; ii++)
    {
        if (spotArray[12][ii]==0 || spotArray[12][ii]==linter)
        {
            for (int jj = 0; jj<16; jj++)
            {
                bw.write(Double.toString(spotArray[jj][ii]));
                if (jj<16){ bw.write(" ");}
            }
            bw.write("\n");
        }
    }
    bw.write("wnot x out of bounds" + "\n");
    for (int ii = 0; ii<counter-1; ii++)
    {
        if (spotArray[13][ii]==-mmax || spotArray[13][ii]==mmax)
        {
            for (int jj = 0; jj<16; jj++)
            {
                bw.write(Double.toString(spotArray[jj][ii]));
                if (jj<16){ bw.write(" ");}
            }
            bw.write("\n");
        }
    }
    bw.write("wnot y out of bounds" + "\n");
    for (int ii = 0; ii<counter-1; ii++)
    {
        if (spotArray[14][ii]==0 || spotArray[14][ii]==ninter)
        {
            for (int jj = 0; jj<16; jj++)
            {
                bw.write(Double.toString(spotArray[jj][ii]));
                if (jj<16){ bw.write(" ");}
            }
            bw.write("\n");
        }
    }
    bw.close();
}
catch (Exception e)
{
    IJ.error("Simple ASCII Writer", e.getMessage());
    return;
}
}
}

```